University of Alberta

Developing Microfluidic Systems for Chromatography

by

Jian-Bin Bao 

A thesis submitted to the Faculty of Graduate Studies and Research
in partial fulfillment of the requirements for the degree of

Doctor of Philosophy

Department of Chemistry

Edmonton, Alberta
Spring 2004

Your file Votre référence
ISBN: 0-612-96237-7
Our file Notre référence
ISBN: 0-612-96237-7

Thesis Abstract

This thesis work focuses on developing microfluidic systems for liquid chromatography (LC). To reach this goal, great effort has first been put into traditional head pressure driven flow. A photobleaching method was developed to accurately measure flow velocities within the microchannels for a given head pressure. Coupled with a finite element method, simulations for D-shaped microchannels were studied to allow comparison with experiment. It was proven that the Hagen-Poisseuille equation, a solution to the Navier-Stokes equations, can describe the flow behavior down to 1 μm deep microchannels. Magnetohydrodynamic (MHD) flow was believed to be able to pump an LC on chip because it shows convenient pumping and valving characteristics. Even for open tubular LC, which has the column with the lowest flow resistance, MHD was shown to be too weak, because the pumping force scales in the wrong direction with size. In order to enhance MHD pumping, three solutions were developed in this thesis work. First, a unique electromagnetic channel (EMC) was designed and fabricated, which generated pumping along the whole channel, gave uniform current density and reduced the flow resistance compared to earlier designs. The challenges of micromachining an EMC were overcome by optimizing electroplating conditions, developing polishing techniques, and reducing the ICP-RIE etching rates. Second, an AC magnet system was developed with a potential application for AC MHD, which demonstrated a high magnetic field at high frequency, using a mechanical rotor. The corresponding techniques for using the magnet were also developed. Third, a novel DC MHD nano pump was invented which showed a flow velocity of higher than 0.1 mm/sec in 10 μm size

microchannels. Through this effort, the possibility of realizing LC chips has been increased. As a major important side product, concentrated gold nanoparticle suspensions were discovered to create a highly DC-conductive liquid, giving an alternative to electrolyte solutions and redox couples. The applications of such a liquid may be wide.

To my parents

Acknowledgements

First and foremost, I would like to express my great gratitude to my research supervisor, Prof. D. Jed Harrison. He introduced me to this exciting field of microfluidics and provided me with his valuable guidance and support throughout the course of my research. I am very thankful for his approval which allowed me to study what I was interested in and for his intellectual and financial support. Each of the *late afternoon* scientific appointments between us was interesting and fruitful, but none of them were short. I am also indebted for his patience in reading my thesis and shaping it to its present form. Thank you, Jed!

Many thanks go to the DJH group members for their helpful discussions. Special thanks go to Dr. Cameron D. Skinner for his advice when I started my research work. I wish to express my gratitude to Mrs. Arlene Figley for making grammatical corrections for my thesis and arranging many last minute emergencies.

As always, the scientific discussions with my brother, Dr. Jianren Bao, were very fruitful. In fact, some smart ideas from him have changed this thesis.

My appreciations extend to the technical support staff from this Department of Chemistry. Particular thanks go to Richard Tomski, who built the AC magnet system which is as nice as his music. Thank you to Hubert Hoffmann, who guided me to design complex machine systems. I am grateful to Ed Feschuk who built all electronic devices. Thank you to Dr. Ken Westra and Keith Franklin at the University of Alberta NanoFab for valuable discussion.

Many thanks go to the members of my candidacy and defence committee in the persons of Dr. Frederick Cantwell, Dr. Mark McDermott, Dr. Charles Lucy, Dr. George Kotovych, Dr. Shijie Liu and Dr. Ash Parameswaran.

Special thanks go to Prof. Zhiquan Shen, Prof. Kemin Yao, and Prof. Xuanzhen Jiang at Zhejiang University for their help and inspiration. I also have to extend my gratitude to my friends either in China or in North America.

Finally, thank you to my parents and my wife, Xiaoshu. Without their love, I never would have made it this far.

Table of Contents

Chapter 3: Design and Fabrication of Magnetohydrodynamic Liquid Chromatography Chips

Chapter 4: Rotating Permanent Magnets for AC Magnetohydrodynamic Pumping

List of Tables

List of Figures

Chapter 1

Chapter 2

Chapter 3

Chapter 4

Chapter 5

List of Abbreviations

AC	Alternating current
B	Buffer reservoir
BW	Buffer waste reservoir
CE	Capillary electrophoresis
CEC	Capillary electrochromatography
CMP	Chemical-Mechanical Polishing
D	Detection location
DC	Direct current
EMC	Electromagnetic channel
emf	Electromotive force
EMLC	Electromagnetic liquid chromatography
EOF	Electroosmotic flow
ER	Electrorheological
ex	Exit
FEM	Finite element method
f.l.	Focal length
HPLC	High performance liquid chromatography
IC	Integrated circuit
ICP	Inductively coupled plasma
i.d.	Inner diameter
in	Inlet
LC	Liquid chromatography
LIF	Laser induced fluorescence
LIGA	Lithographie, Galvanoformung, Abformung
MEMS	Microelectromechanical systems
MHD	Magnetohydrodynamic(s)
MPC	Monolayer protected clusters
o.d.	Outer diameter
OTLC	Open tubular liquid chromatography
PDMS	Poly(dimethylsiloxane)
RIE	Reactive ion etch systems
rms	Root mean square
RPM	Revolutions per minute
rsd	Relative standard deviation
S	Sample reservoir
sccm	cc of gas at STP per minute (1 sccm = 4.5×10^{17} s^{-1})
sd	Standard deviation
SW	Sample waste reservoir
TEM	Transmission electron microscopy
wr	Weir
μTAS	Micro total analysis systems

Chapter 1

Introduction

1.1 Pumping in Micro Total Analysis Systems

The concept of the micro total analysis systems (μTAS) (1) or lab-on-a-chip has been revolutionary in providing routes to shrinking the size of analytical tools, reducing the consumption of samples and reagents, enhancing the analytical performance and producing unique advantages in the integration of separation techniques (2-11). In the past decade, researchers in academics and industry have developed a variety of μTAS systems (12-13). These include various types of sample preparation (14-18), injection (8, 19-21), fluid and particle handling (22-24), mixing (25, 26), reaction (27-29), separation (30-34), and detection (11, 35-37), as well as applications in immunoassays (29, 38), protein separation (39, 40), DNA separation (35, 41-42), DNA sequencing (43, 44), and clinical diagnostics (45-47).

Most of these systems utilize electrokinetic effects to pump the fluids, such as electroosmotic flow (EOF), dielectrophoresis (48, 49) or electrohydrodynamics (50). Electrokinetic effects are so successful in μTAS systems due to the unique demands and characteristics of microfluidics. The key element is that there are no mechanically

moving parts required by electrokinetics, as there are when pumps and valves are used. EOF pumping is not sensitive to the dimensions of the microchannel below about 300 μm, except in terms of the magnitude of the currents, and resultant Joule heating. EOF is produced along the entire length of the microchannel. More importantly, the flow in interconnected channels can be controlled by switching voltages, without any active valving. Therefore, by using an EOF pump, capillary electrophoresis (CE) and capillary electrochromatography (CEC) can be realized on a microchip, and flow control can be optimized by switching voltages between the channel-contacting reservoirs (3, 4).

While presenting advantages, EOF also exhibits limitations. EOF is highly dependent on the channel surface charge and on the solution conditions. Not all buffers are suitable for EOF (51). For glass channels, EOF often does not work very well at low pH. It is not always possible to mobilize biological cells, because cells may be lysed by the high voltages that the EOF pump uses. Compared to pressure driven flow, EOF has poor stability. This is the key reason that high-performance liquid chromatography (HPLC) has better reproducibility than CE or CEC.

Researchers have been continuing to seek new pumping techniques for μTAS. Table 1.1 lists some of the micropumps developed in the past few years. Among nonmechanical pumps, gravity pumps (52, 53) driven by hydraulic pressure are simple in principle, but the velocity is quite limited. Various bubble pumps control the flow by

Table 1.1. Pumping techniques developed for μTAS.

Type	Name	Mechanism	Ref
Nonmechanical	Gravity pump		52, 53
	Bubble pump	Thermal	54, 55
		Thermolysis	56
		Electrolysis	57
		Decomposition	58, 59
	Evaporation pump		60-62
	Centrifugal pump		63, 64
	Surface pump	Electrochemical	65
		Capillary wetting	66, 67
		Electrocapillary	23
Mechanical	Piezoelectric pump		68-71
	Peristaltic pump		72-74
	Magnetic pump		75-77
	Shear driven pump		78
	Squeezing pump		79

generating bubbles or expanding the bubble volume within channels, using increased temperature (54, 55), thermolysis (56), electrolysis (57), or chemical decomposition (58, 59). The pumping velocity can be high, but before using them, these systems must be closed after adding sample and reagents. Evaporation pumps (60-62) induce liquid to flow by constantly removing it at one end of an open system by evaporation. Obviously, the flow can only go one direction. Centrifugal pumps (63, 64) generate pumping by centrifugal force. Depending upon the rotation speed, the pumping can be very powerful. However, there is no way to reverse the flow direction. Surface pumping by electrochemistry (65), capillary force (66, 67) or electrocapillary (23) can also generate powerful flow. However, like the EOF pump, they are surface or interface condition dependent. Mechanical pumps include various piezoelectric pumps (68-71), peristaltic pumps (72-74), magnetic pumps (75-77), shear driven pumps (78), and squeeze pumps (79), etc. They can be bidirectional, and may give a high velocity flow. However, the size of micromechanical pumps is bigger than most EOF systems, and the fabrication is more difficult.

Importantly, at intersections, controlling the direction of flow generated by most pumps is difficult. Microvalves have been an area of continuing research in microfluidics, and very recently significant progress has been made. However, they suffer from relatively complex fabrication steps, leakage, and lack of appropriate, microfabrication

compatible materials (80). Most soft material microvalves developed cannot handle high pressure, such as poly(dimethylsiloxane) (PDMS) (81, 82), hydrogels (83), and other soft polymers (81). A ball valve (84) developed at Sandia National Laboratory was shown to withstand 3400 psi, but the yield of manufacture was low. Despite all these efforts, controlling a non-EOF flow chip using microvalves remains a challenge.

This thesis work focuses on a pumping technique using a different mechanism than EOF, but with the same convenience of flow control and valving that EOF offers. This technique is magnetohydrodynamic (MHD) pumping. By using MHD flow, a liquid chromatography (LC) on chip may be feasible.

1.2 Liquid Chromatography

1.2.1 Benchtop Liquid Chromatography

As we know, CE and CEC have a sister, liquid chromatography (LC). According to Snyder (85), LC has been in first place in total analytical instrument sales since the 1990s. Based on the columns used, LC can principally be divided into two categories: packed column liquid chromatography and open-tubular liquid chromatography (OTLC). The former technique has been dominant in both research and industry. The reasons behind this are: a) packed column liquid chromatography can obtain very reasonable separation efficiency; b) various high-quality packed columns are commercially

available; c) packed columns are compatible with benchtop HPLC pumps. The trend for packed column LC has been to reduce column i.d. from 4.6 mm (usual packed column), to 2.1 mm (narrow bore column), to 1.0 mm (micro bore column), to 0.01-0.75 mm (packed fused silica capillary column). Some of the rationale for these size reductions include improved separation efficiency due to greater column uniformity, reduced sample and solvent (eluent) consumption, potentially less sample dilution, and often higher speed separations. "The ultimate form of miniaturization is to reduce the column diameter to such an extent that the stationary phase can reside on the wall of the column and packing material is no longer needed (86)." This is known as OTLC.

The plate height in an OTLC column can be estimated by the Golay equation (87) as

$$H = H_{LD} + H_M + H_S = \frac{2D_m}{v} + \frac{1+6k'+11(k')^2}{(1+k')^2} \cdot \frac{d_c^2 v}{96D_m} + \frac{2k'}{(1+k')^2} \frac{d_f^2 v}{3D_s} \qquad (1.1)$$

where H is the plate height, the variance of the peak width per unit length of column. Contributing factors include the longitudinal diffusion term, H_{LD}, resistance to mass transfer terms in the mobile phase, H_M, and in the stationary phase, H_S. In equation 1.1, v is the mobile phase velocity, k' is the capacity factor of the analyte, D_m and D_s are diffusion coefficients of the analyte in the mobile and stationary phases, respectively, d_f is the thickness of the stationary phase, and d_c is the diameter of the column available for the mobile phase (equal to the i.d. of the column minus 2 d_f).

The same range of mobile phase velocity may be used in OTLC as is used in conventional packed LC, *i.e.* from 0.1 to 50 mm/sec (88). In this velocity range, the H_M term is much larger than the other terms. It is also a function of the channel size. The larger the size, the larger the plate height contribution. At the low velocity extreme, the H_{LD} term gets larger (the H_S term is still small), but this is not a common operating range due to the low speed of separation. To minimize H_M, the i.d. of an OTLC column should be in the range of 0.2 to 10 μm (86). The short optical path lengths in such small column mean it is even harder to detect than CE volumes. The pressures needed for submicron capillaries are quite high. The manufacture and use of such small columns is also a big challenge. Therefore, in practice, "a compromise is often made between efficiency and the i.d. of the column," leading to a column size smaller than 10 μm (86, 88). To be compatible with the small column size, the linear sample capacity (LSC) in such columns is also very low, typically requiring a volume of 30-300 pL (86). "Conventional HPLC injection and detection devices, designed for sample and peak volumes of several μL, cannot be used" for such small columns (86). In terms of retention and loading ability, traditional stationary phases for packed columns are not optimal, "because the wall surface-to-volume ratio in an OTLC column is much smaller than that in packed columns (86)." All the above are reasons why OTLC did not become widely used, although open tubular columns were first described three decades ago (89).

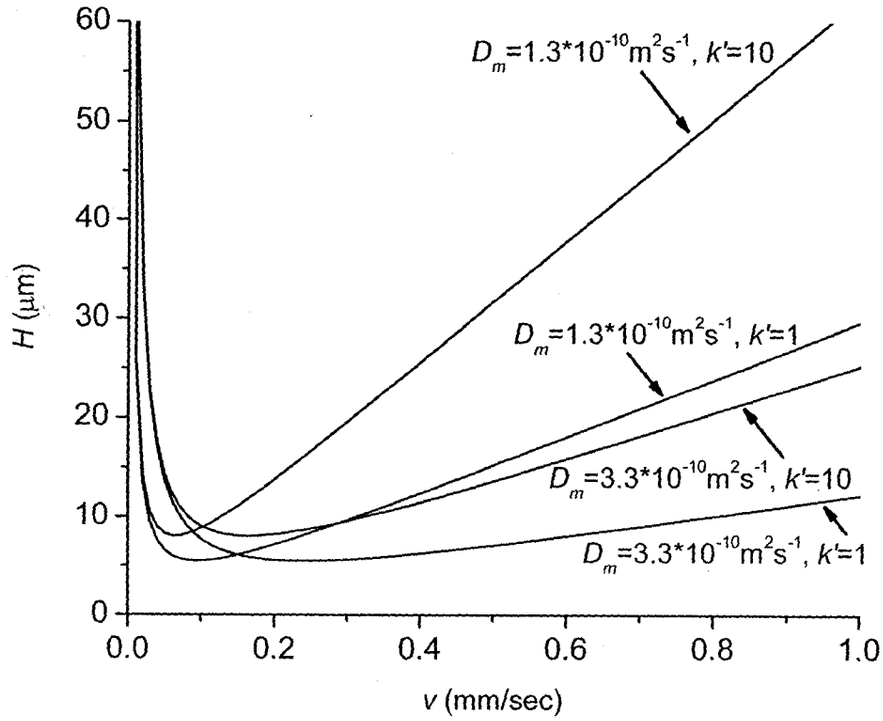

Figure 1.1. Theoretical plate height versus mobile phase velocity for OTLC.

Based on equation 1.1, we prepared a plot of the theoretical plate height versus the mobile phase velocity in a 10 μm column (d_c) for different diffusion coefficients, D_m, and capacity factor, k', as shown in Figure 1.1. The minimum theoretical plate height is more sensitive to the diffusion coefficient than the capacity factor. For a typical dye solution, fluorescein in water, $D_m = 3.3\times10^{-10}$ m^{2}s^{-1} (90). The optimum velocity is about 0.2 mm/sec, but small values of H are achieved if the mobile flow velocity is larger than

0.1 mm/sec. The separation of biological samples such as proteins is of greatest interest. For a moderate sized protein, cytochrome *c* in water, $D_m = 1.3\times10^{-10}$ m^2s^{-1} (91). The optimum mobile phase velocity is 0.06-0.1 mm/sec. Therefore, this thesis work chose 0.1 mm/sec as the minimum pumping velocity in the microchannels.

1.2.2 LC Chips

LC chips are attractive for many reasons, including faster analysis or extremely small sample and reagent volumes (51, 80) compared to conventional LC. These advantages are similar to the advantages miniaturization on chip offers for CE. However, as stated by Harris (51), "although miniaturizing those techniques (*i.e.* CE and CEC) quickly proved fruitful, doing the same to LC was a different story. The difficulties of microscaling pressure-based LC systems, of fabricating efficient separation devices on which nanoliter volumes flow in an area the size of one's hand, became far more challenging to solve." Note that partially integrated LC components, such as an LC column on a chip (92, 93), are much more easily realized, but do not seem to be attractive because there are fairly few advantages.

Manz *et al.* presented an idea for OTLC on a chip in 1990 when μTAS made its debut (2), but no data for operation of that device was ever published and no pump was included. Basically, both packed LC and OTLC are possible on chip. However, packing

chromatographic beads on chip can be difficult, and the pressure required for packed LC is higher than that of OTLC if the open tubular column size is not too small. As a result, OTLC should have a much better chance to be realized on chip.

Very recently, Harris discussed the efforts that researchers in both academics and industry have put into LC chips. He predicted that LC chips would replace benchtop systems in a 5 to 10-year time frame (51). To reach that goal, there is still a lot of work to do. As we know, benchtop liquid chromatographs are all activated by pressure driven flow. However, pressure driven flow requires pumps and valves; manipulating such a flow on chip is very difficult. Being aware of the difficulties of using pressure driven flow on chip, researchers such as A. Manz began to explore "whatever generates the pressure" (51). Even so, almost all of the pumping techniques listed in Table 1.1 are not suitable for LC chips, because they are either too weak or lack ways to manipulate the flow direction at intersections. We therefore believe that LC chips continue to need a new pumping and valving method.

1.3 Magnetohydrodynamic Pump

1.3.1 History

Magnetohydrodynamics (MHD) is defined as the science of the motion of electrically conducting fluids through magnetic fields (94). Its history can be traced back

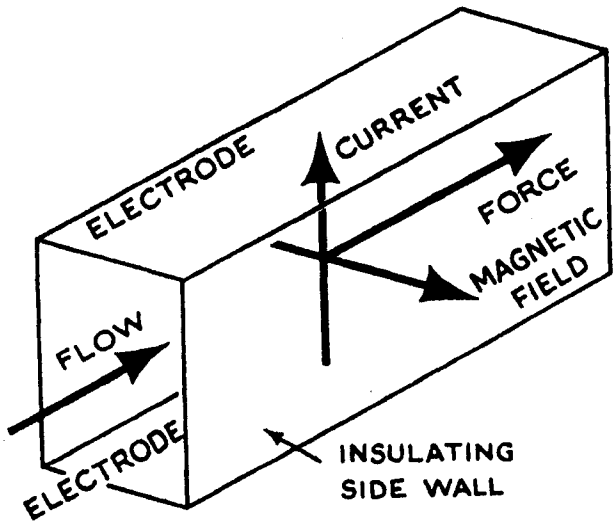

Figure 1.2. Schematic electromagnetic pump (94).

to the 1830s, when "Faraday (95) and his contemporaries knew that solid or fluid material moving in a magnetic field experiences an electromotive force (emf). If the material is electrically conducting and a current path is available, electric currents ensue (94)." Equally so, if an electric current is applied in a magnetic field, then the material experiences a force known as the Lorentz force, causing it to move. "Ritchie had in effect pumped water electromagnetically in 1832 (96), yet not until the early twentieth century was that obvious MHD device, the electromagnetic pump, developed in practical forms. Figure 1.2 shows it at its simplest, with imposed transverse current flow and magnetic field yielding an electromagnetic force along the channel (94)."

MHD was not initially recognized as a means of pumping water. Instead, astrophysicists came to realize the prevalence throughout the universe of conducting,

ionized gases (plasmas) and significantly strong magnetic fields (94, 97). Also, "electromagnetic pumping of liquid metal coolants became standard practice and electromagnetic pumping, stirring and levitation were exploited in the metallurgical industries" (94, 98, 99). Eventually though, a pump for water was realized. A boat named *Yamoto-1* realized a successful combination of magnetic field and electric field to pump seawater and create a powerful propulsion system (100).

1.3.2 Applications in μTAS

MHD received attention for pumping water in μTAS, since μTAS needs more pumping techniques. Compared to the other micropumps listed in Table 1.1, in terms of pump activation, flow control and fluid direction switching, the MHD pump is most comparable to the EOF pump. Both use a voltage to generate flow, both can switch and flip flow direction by controlling the applied voltage, and both can be used to balance flows in intersecting channels, creating a valve with no moving parts. However, MHD needs a magnetic field in addition to an electric field, and while using higher currents than EOF, it uses lower voltages.

Based on their operation modes, the MHD pumps on chip can be divided into two categories: DC and AC MHD pumps.

1.3.2.1 DC Mode – Electrolysis Causes Bubbles

MHD pumping can be operated in either DC or AC mode. In the DC mode, a DC current is applied across the channel in the presence of a uniform magnetic field. Jang and Lee first fabricated a DC MHD micropump using a permanent magnet and applying DC current. A pumping pressure of 0.2 kPa was obtained, but the solution rapidly underwent electrochemical decomposition and generated bubbles (101, 102). Huang *et al.* fabricated a DC electromagnetic micropump using the LIGA method, but concluded the device a failure due to the generation of bubbles (103). Bau *et al.* published a series of papers on a DC MHD micropump (104), mixer (105), stirrer (106, 107), fluidic network (108), or complex flow (109). Schasfoort *et al.* also presented an MHD mixer that induced liquid vortices in the presence of both EOF flow and MHD flow under a permanent magnetic field (110). However, for aqueous solutions, the practical application of DC MHD is quite limited, because of unavoidable gas bubbles, generated by the electrolysis needed to enable the current conduction required for the Lorentz force (101-110). Gas bubbles in flow channels clearly present many problems, and should be avoided.

1.3.2.2 AC Mode – Bubble Current Density Threshold

DC MHD is simple, but impractical for an LC or most other microfluidic systems. To solve the bubbling problem, Heng *et al.* employed an AC current and a permanent magnetic field, coupled with a channel in a diffuser/nozzle structure so as to generate a net flow in one direction (111). Simultaneously, Gong *et al.* fabricated a four-layer electromagnetic pump, in which a Fe-Ni magnetic core was included on chip. With a microvalve design, AC electric voltages can be used to activate the pump (112, 113). The first AC MHD pump (AC electric field coupled with AC magnetic field) was proposed by Lemoff and Lee (114-116). "A sinusoidal electric current was used with a perpendicular, synchronous AC magnetic field from an electromagnet. Since the fields are synchronous, the Lorentz force points in the same direction throughout the cycle. When an AC current of sufficiently high frequency is passed through an electrolytic solution, the chemical reactions are reversed rapidly enough that bubbles never have a chance to form, and no electrode degradation can occur (114, 115)." Solving the bubble problem allows AC MHD to be used in μTAS. According to Lemoff and Lee (114, 115), "the Lorentz force varies in magnitude through one period of oscillation, the flow is actually pulsed; however, at high frequencies, the pulsed volume is so small that the flow is effectively continuous, reflecting only the time-averaged force. The time-averaged Lorentz force not only depends on the current amplitude and the magnetic field amplitude but also on the

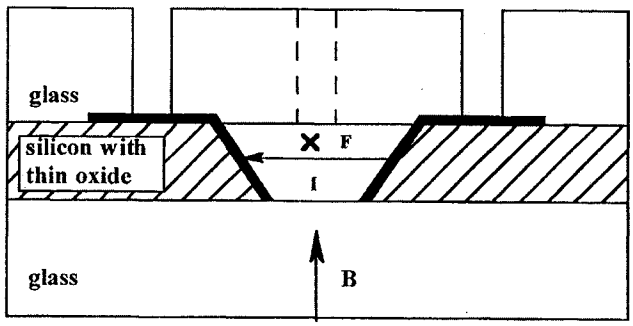

Figure 1.3. Trapezoidal channel cross-section of MHD pump designed by Lemoff and Lee (115).

phase of the magnetic field relative to the electrode current." Controlling the phase of the current controls not only the flow speed but also the flow direction (114, 115).

An AC MHD micropump with trapezoidal cross-section (Figure 1.3) was fabricated and tested by Lemoff and Lee (114, 115). A weak (B = 7.4-18.7 mT) electromagnet was positioned underneath the fluidic chip. NaCl aqueous solutions were introduced into the chip. Measurements were done on varying concentrations (0.01-1 M) of NaCl solution as a function of frequency, to determine the maximum current allowed in the microchannels before bubble formation was observed (Figure 1.4). The magnetic field strength of the electromagnet (mini-electromagnet) as a function of frequency was measured, as shown in Figure 1.5. A maximum flow velocity of 1.51 mm/sec was realized in a 380 μm deep × 800 μm wide (top) trapezoidal channel (the trapezoidal angle is 54°).

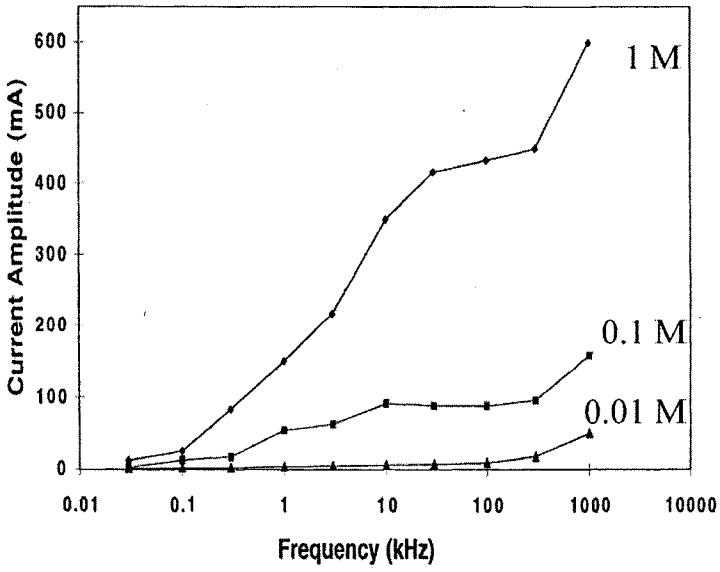

Figure 1.4. Bubble current threshold for varying concentrations of NaCl solution as a function of frequency (115).

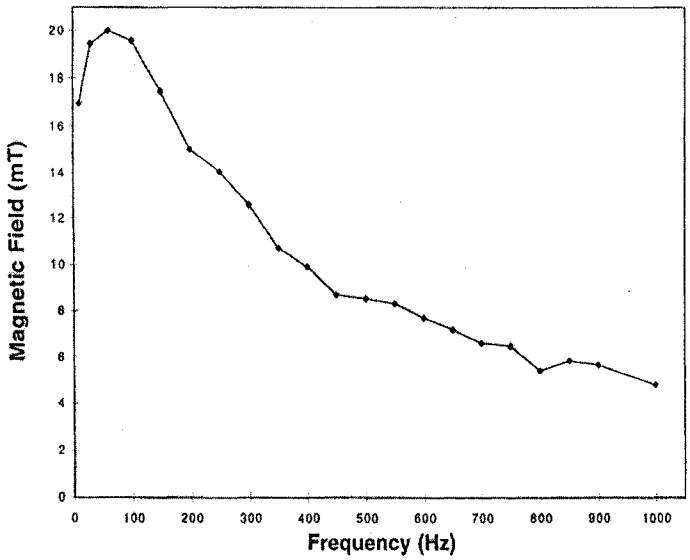

Figure 1.5. Magnetic field strength as a function of frequency given the same driving voltage amplitude of 5.5 V (115).

Another device was tested by Eijkel *et al.* (117, 118). A circular AC MHD micropump was developed, with an idea of running circular LC on chip, as shown in Figure 1.6. Reversible, controlled AC MHD flow of maximally 40 μm/sec in a 30 μm deep × 200 μm wide channel was demonstrated. A compromise between solution electrolysis and heating induced by eddy currents was struck by driving the device at 2.44 kHz for their magnetic field (105 mT) (117, 118). The phase shift between applied voltage and observed current was studied so as to reach a perfect phase matching.

Unfortunately, both AC MHD pumps were not strong enough for LC chips, either because the pumping velocity was too slow (117, 118) or because the channel size was too big (114, 115). It is the goal of this thesis work to enhance the MHD pump and reach a pumping velocity and channel dimension that satisfies the demands of the Golay equation for OTLC.

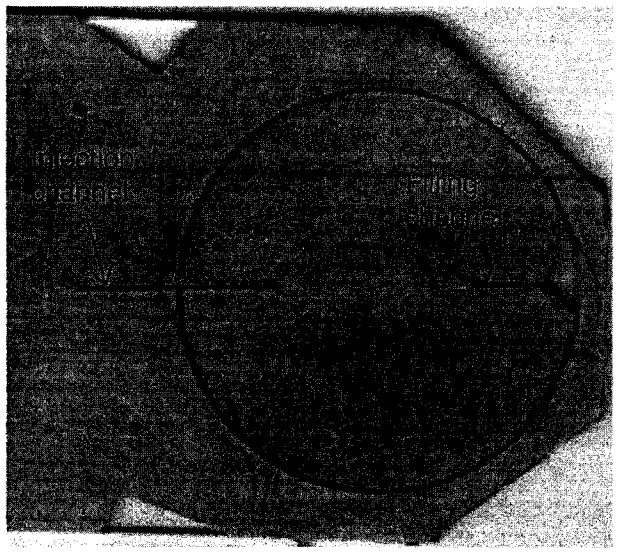

Figure 1.6. Circular AC MHD micropump designed by Eijkel *et al.* (118) with 30 μm high channel structure fabricated in electroformed gold prior to sealing.

1.4 Microelectromechanical Systems

The semiconductor industry and the engineering research community have developed many microelectromechanical fabrication techniques. Many processes that have been used for the fabrication of μTAS, such as the lithography, HF isotropic wet etching, sputtering, cleaning and bonding techniques were used in this thesis work also. Most of these are relatively familiar and are discussed in the literature (119), so will not be discussed here. Some of the newer or less frequently used methods are discussed here.

1.4.1 ICP-RIE

Deep silicon etching is a key technology in fabricating microelectromechanical systems (MEMS). These structures range in depth from around 10 μm to 500 μm (120). Two popular techniques have been developed for achieving such deep, vertical silicon structures (120). One was invented by Robert Bosch GmbH and referred to as the Bosch process. The other was named the cryo process, which relies on cooling the stage and silicon to cryogenic temperatures using liquid nitrogen (120). This thesis work used the Bosch process.

Walker (120) provided an excellent summary on the use of the Bosch process (Figure 1.7) in MEMS. "This process uses a fluorine based plasma chemistry to etch the silicon, combined with a fluorocarbon plasma process to provide sidewall passivation and

improved selectivity to masking materials. A complete etch process cycles between etch and deposition steps many times to achieve deep, vertical etch profiles. It relies on the source gases being broken down in a high-density plasma region before reaching the wafer surface, which has a small but controlled voltage drop from the plasma. This technique cannot be performed in reactive ion etch systems (RIE), as these have the wrong balance of ions to free radical species (120)." This balance can be achieved in high-density plasma systems, using inductively coupled plasma (ICP) methods (120).

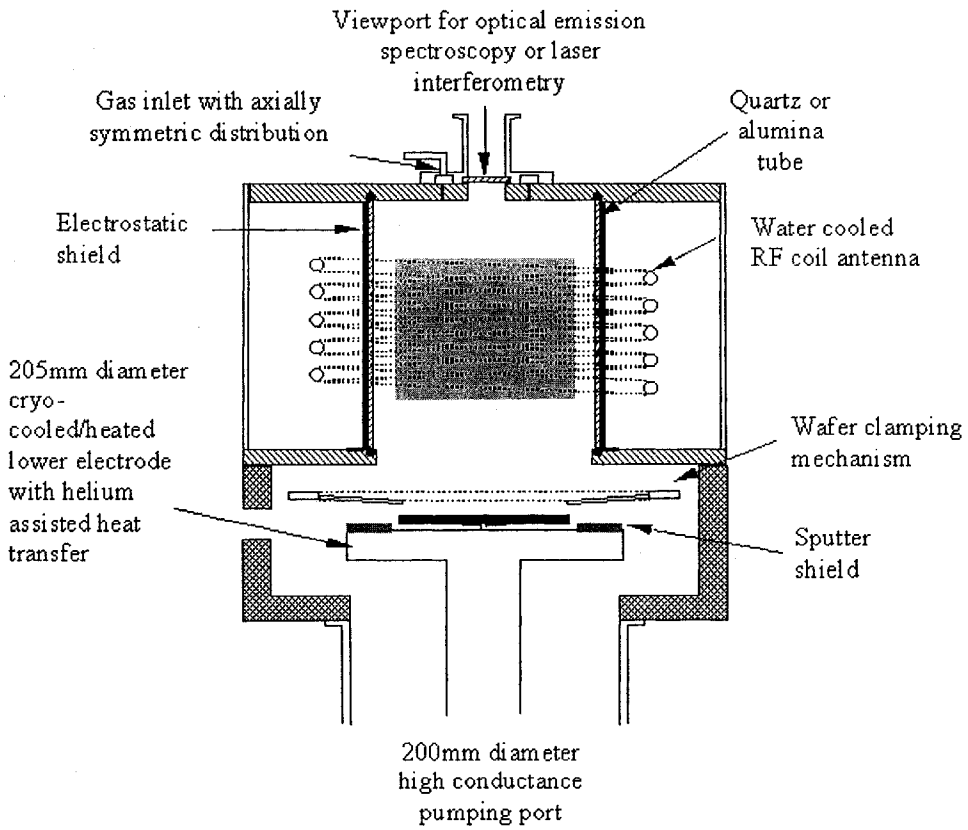

Figure 1.7. Schematic diagram of ICP system used for Bosch processing (120).

According to Walker (120), sulphur hexafluoride (SF_6) is the source gas which will break up in an ICP to release free radical fluorine for silicon etching. The sidewall passivation is provided by octafluorocyclobutane ($c\text{-}C_4F_8$), a cyclic fluorocarbon that decomposes to produce CF_2 and longer chain radicals in the ICP. These readily deposit as a fluorocarbon polymer on the samples being etched (120). Therefore, for the Bosch process, the polymer deposition and isotropic etch are alternated, resulting in a rough sidewall (119) as shown in Figure 1.8.

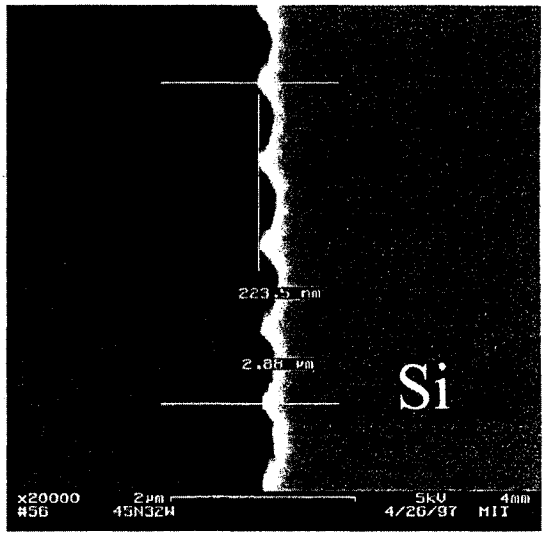

Figure 1.8. SEM of sidewall roughness from Bosch process (119).

The profile and etch rate are controlled by adjusting the step efficiencies or the ratio of duration of the two steps. However, as Walker (120) says, "adjusting the process requires an understanding of the various mechanisms occurring. For example, increasing the bias in an attempt to reduce *grass* at the bottom of features may have unwanted side effects." "Reducing pressure assists in transport of reactants and products into and out of etched features, but this must be accompanied by a reduction in ICP power, to avoid an increase in ion density (120)." A relatively easier way to adjust the process is to change the length of the etch step, because "this will not significantly change the amount or

energy of ions involved, but will alter the balance between polymer deposition and removal (120)."

1.4.2 Electroplating

A typical electroplating cell consists of anode, cathode, aqueous-metal solution, and a power supply, as shown in Figure 1.9 for nickel electroplating (121). It is an established technique for large-scale industrial purposes. As Judy (121) says, "to fabricate microstructures by electroplating, a conductive plating base or seed layer and a means to pattern the electrodeposit are needed. Since the localized electrodeposition rate is proportional to the localized current density, a uniform current density over the entire seed layer is needed to obtain an electrodeposit having a uniform thickness. To achieve selective deposition, however, portions of the seed layer are covered with an insulating masking material, which makes the current density in its proximity non-uniform. An example of the effect the plating mask has on the uniformity of the current density is illustrated in Figure 1.10." Non-uniform current density also results in different gradients of metal ion concentration in the electroplating solution. Both effects cause different deposition rates. Typically, a thin channel well separated from other features will deposit at a much faster rate than does a wide channel with a high density of open channels.

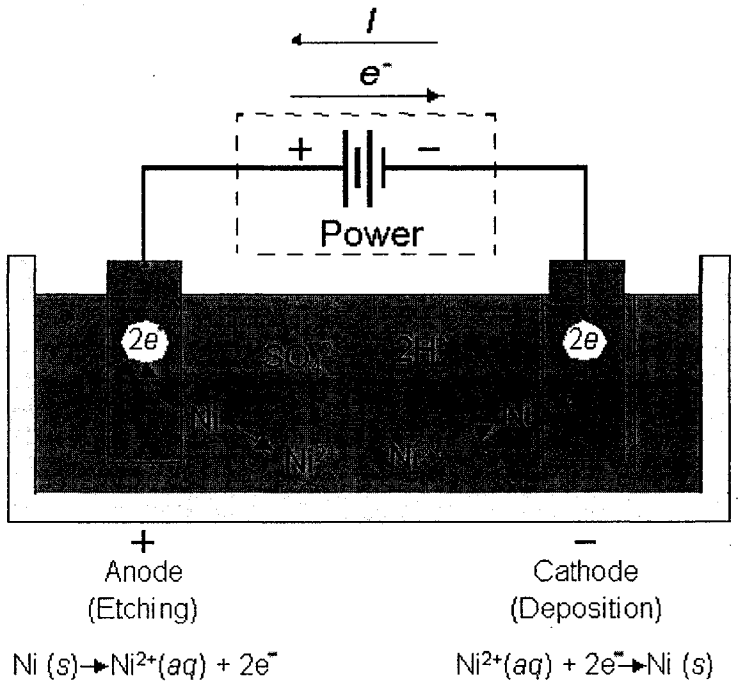

Figure 1.9. Electroplating setup (121).

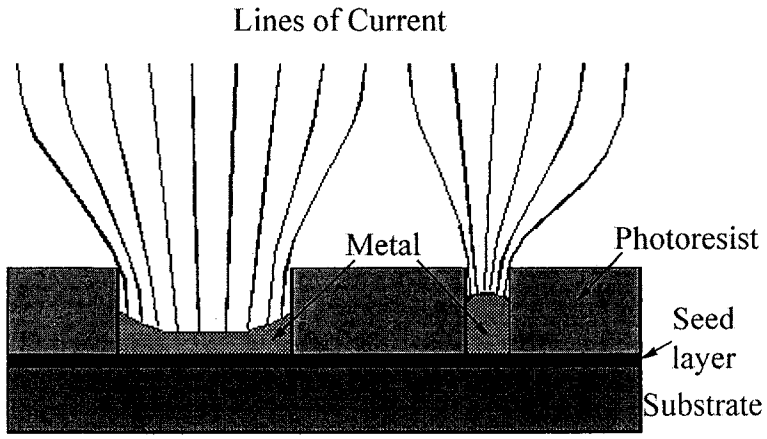

Figure 1.10. Illustration of non-uniform electroplating current density (121).

The deposition rate difference can be reduced by using waveform modification (reverse pulse) or incorporating additional organic compounds (122). However, since this problem is fundamental, it is impossible to get a uniform surface. Therefore, a polishing process, as discussed below, is required.

1.4.3 Chemical-Mechanical Polishing

"Chemical-Mechanical Polishing (CMP) is a polishing process that laterally removes material to form a smooth surface on a variety of materials, metals, and dielectrics (123)." This technique is widely used in integrated circuit (IC) and MEMS manufacturing. Since "the demand to increase the performance of ICs has led to a continuous increase in device density and operating speed," the utilization of low resistivity metals aids in meeting the challenges this creates (123). Currently, "Cu (Figure 1.11) is replacing the standard of Al in some products because of its higher electrical conductivity (125)." Ag is believed to be a candidate for the next chip generation, but CMP of Ag is not well studied (125). Searching the Web of Science found very few papers published on CMP of Ag (125).

"The conventional CMP process uses a slurry, which consists of fine abrasive particles suspended in an aqueous solution containing chemical reagents (124)." It works well for hard metals like W but it is expected to be a challenge for soft metals like Ag

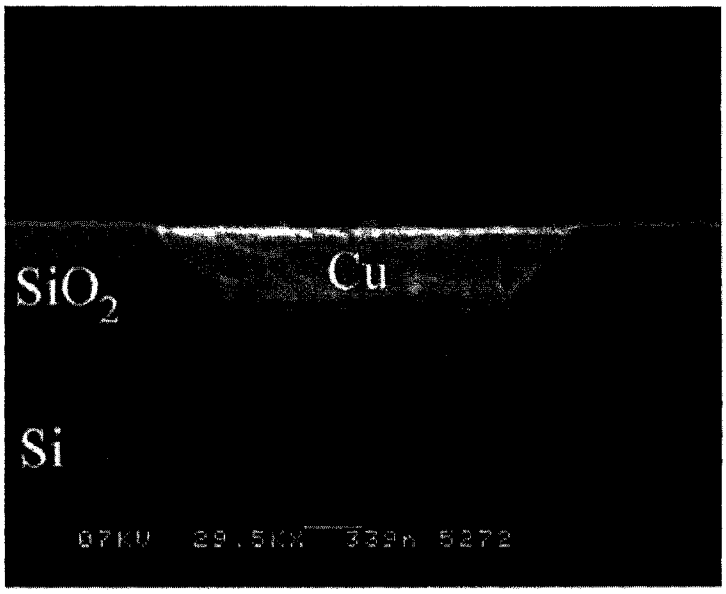

Figure 1.11. Cross-sectional SEM image of a test structure of 2-μm wide copper (124).

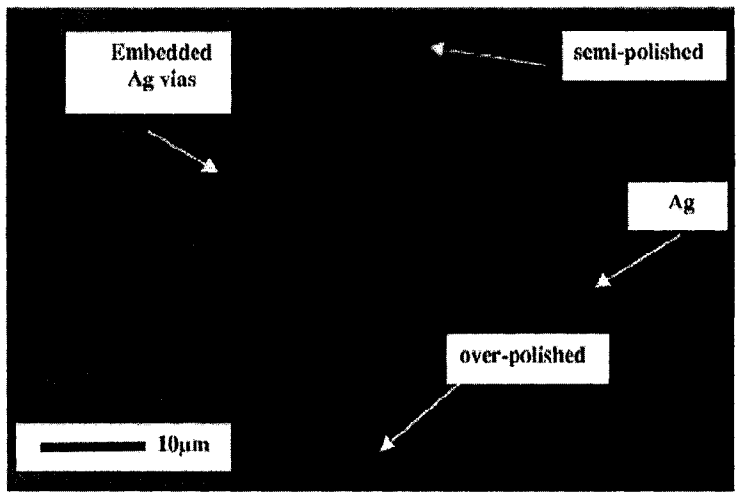

Figure 1.12. Optical micrograph of a polished region. Embedded Ag structures are near to an over-polished and a semi-polished region (125).

(125). Figure 1.12 shows a polished Ag device, in which both semi-polished and over polished regions exist (125). Obviously, such a non-uniform polish process is not satisfactory. This thesis work will require Ag as the material for wires and electrodes because of its low resistivity and absence of response to a magnetic field. Therefore, a polishing process for Ag needs to be developed.

1.5 Scope of the Thesis

This thesis work focuses on pressure driven flow in microchannels and on one of the most important applications of pressure driven flow – liquid chromatography on chip. To reach this goal, great efforts have been put into traditional head pressure driven flow and MHD flow, a pressure-like flow in microchannels. A better understanding of pressure driven flow in microchannels was obtained by studying the relation between head pressures and flow velocities. In order to enhance an MHD pump, a unique electromagnetic channel (EMC) was designed and fabricated in this thesis work, in which pumping occurred along the entire channel length. A strong AC magnetic field was developed with a potential application for AC MHD. Concentrated gold nanoparticle suspensions were discovered to be highly conductive liquids. By using these suspensions, a novel DC MHD nano pump was invented which showed fast enough pumping velocity in a small size microchannel for OTLC chips.

The efforts described in Chapter 2 address the applicability of the Hagen-Poisseuille equation, a solution to the Navier-Stokes equations, to microchannels on the dimension of a micron. A photobleaching method was developed to accurately measure flow velocities within the microchannels. Coupled with a finite element method (FEM), simulations for D-shaped microchannels were studied to allow comparison with experiment. It was proven that the Hagen-Poisseuille equation can describe the flow behavior down to 1 μm deep microchannels. These devices can be used to form packed chromatographic beds for LC or CEC.

In order to enhance MHD pumping, three ideas were developed in this thesis work. Chapter 3 describes one of them, an electromagnetic channel (EMC) design, which generated pumping along the whole channel, gave uniform current density and reduced the flow resistance. The challenges of micromachining an EMC were overcome by optimizing electroplating conditions, developing polishing techniques, and reducing the ICP-RIE etching rates.

Another idea for the MHD pump is discussed in Chapter 4. An AC magnet system was developed, which demonstrated a high magnetic field at high frequency, using a mechanical rotor. The corresponding techniques for using the magnet were also developed.

Chapter 5 presents a successful idea for generating DC MHD in a microchip. An MHD nano pump was invented with the discovery of a highly electrically conductive liquid, made from a concentrated gold nanoparticle suspension. The flow velocity realized by the MHD nano pump was higher than 0.1 mm/sec in 10 μm size microchannels.

As discussed in Chapter 6, although an LC chip was not achieved, substantial progress was made, and the remaining steps are outlined.

1.6References

1. Manz, A.; Graber, N.; Widmer, H. M. *Sens. Actuators* **1990**, B1, 244-248.
2. Manz, A.; Miyahara, Y.; Miura, J.; Watanabe, Y.; Miyagi, H.; Sato, K. *Sens. Actuators* **1990**, B1, 249-255.
3. Harrison, D. J.; Manz, A.; Glavina, P. G. *Transducers '91* **1991**, 792-795.
4. Manz, A.; Harrison, D. J.; Fettinger, J. C.; Verpoorte, E.; Ludi, H.; Widmer, H. M. *Transducers '91* **1991**, 939-941.
5. Manz, A.; Harrison, D. J.; Verpoorte, E. M. J.; Fettinger, J. C.; Paulus, A.; Ludi, H.; Widmer, H. M. *J. Chromatogr.* **1992**, 593, 253-258.
6. Harrison, D. J.; Manz, A.; Fan, Z. H.; Ludi, H.; Widmer, H. M. *Anal. Chem.* **1992**, 64, 1926-1932.

7. Effenhauser, C. S.; Manz, A.; Widmer, H. M. *Anal. Chem.* **1993**, 65, 2637-2642.

8. Harrison, D. J.; Fluri, K.; Seiler, K.; Fan, Z. H.; Effenhauser, C. S.; Manz, A. *Science* **1993**, 261, 895-897.

9. Harrison, D. J.; Fan, Z. H.; Seiler, K.; Manz, A.; Widmer, H. M. *Anal. Chim. Acta* **1993**, 283, 361-366.

10. Harrison, D. J.; Glavina, P. G.; Manz, A. *Sens. Actuators B* **1993**, 10, 107-116.

11. Seiler, K.; Harrison, D. J.; Manz, A. *Anal. Chem.* **1993**, 65, 1481-1488.

12. Reyes, D. R.; Iossifidis, D.; Auroux, P.-A.; Manz, A. *Anal. Chem.* **2002**, 74, 2623-2636

13. Auroux, P.-A.; Iossifidis, D.; Reyes, D. R.; Manz, A. *Anal. Chem.* **2002**, 74, 2637-2652

14. Figeys, D.; Aebersold, R. *Anal. Chem.* **1998**, 70, 3721-3727.

15. Oleschuk, R. D.; Shultz-Lockyear, L. L.; Ning, Y. B.; Harrison, D. J. *Anal. Chem.* **2000**, 72, 585-590.

16. Li, J.; Wang, C.; Kelly, J. F.; Harrison, D. J.; Thibault, P. *Electrophoresis* **2000**, 21, 198-210.

17. Wen, J.; Lin, Y.; Xiang, F.; Matson, D. W.; Udseth, H. R.; Smith, R. D. *Electrophoresis* **2000**, 21, 191-197.

18. Hisamoto, H.; Horiuchi, T.; Uchiyama, K.; Tokeshi, M.; Hibara, A.; Kitamori, T. *Anal. Chem.* **2001**, 73, 5551-5556.

19. Jacobson, S. C.; Ermakov, S. V.; Ramsey, J. M. *Anal. Chem.* **1999**, 71, 3273-3276.

20. Zhang, C. X.; Manz, A. *Anal. Chem.* **2001**, 73, 2656-2662.

21. O'Neill, A. P.; O'Brien, P.; Alderman, J.; Hoffmann, D.; McEnery, M.; Murrihy, J.; Glennon, J. D. *J. Chromatogr. A* **2001**, 924, 259-263.

22. Jacobson, S. C.; McKnight, T. E.; Ramsey, J. M. *Anal. Chem.* **1999**, 71, 4455-4459.

23. Prins, M. W. J.; Welters, W. J. J.; Weekamp, J. W. *Science* **2001**, 291, 277-280.

24. Schrum, D. P.; Culbertson, C. T.; Jacobson, S. C.; Ramsey, J. M. *Anal. Chem.* **1999**, 71, 4173-4177.

25. Stroock, A. D.; Dertinger, S. K. W.; Ajdari, A.; Mezic, I.; Stone, H. A.; Whitesides, G. M. *Science* **2002**, 295, 647-651.

26. Qiu, C. X.; Harrison, D. J. *Electrophoresis* **2001**, 22, 3949-3958.

27. Eijkel, J. C. T.; Prak, A.; Cowen, S.; Craston, D. H.; Manz, A. *J. Chromatogr. A* **1998**, 815, 265-271.

28. Lu, H.; Schmidt, M. A.; Jensen, K. F. *Lab Chip* **2001**, 1, 22-28.

29. Hatch, A.; Kamholz, A. E.; Hawkins, K. R.; Munson, M. S.; Schilling, E. A.; Weigl, B. H.; Yager, P. *Nat. Biotechnol.* **2001**, 19, 461-465.

30. Burggraf, N.; Manz, A.; Verpoorte, E.; Effenhauser, C. S.; Widmer, H. M. *Sens. Actuators B* **1994**, 20, 103-110.

31. Culbertson, C. T.; Jacobson, S. C.; Ramsey, J. M. *Anal. Chem.* **2000**, 72, 5814-5819.

32. Jacobson, S. C.; Culbertson, C. T.; Daler, J. E.; Ramsey, J. M. *Anal. Chem.* **1998**, 70, 3476-3480.

33. He, B.; Tait, N.; Regnier, F. *Anal. Chem.* **1998**, 70, 3790-3797.

34. Han, J.; Craighead, G. *Science* **2000**, 288, 1026-1029.

35. Woolley, A. T.; Lao, K. Q.; Glazer, A. N.; Mathies, R. A. *Anal. Chem.* **1998**, 70, 684-688.

36. Li, J.; Thibault, P.; Bings, N. H.; Skinner, C. D.; Wang, C.; Colyer, C. L.; Harrison, D. J. *Anal. Chem.* **1999**, 71, 3036-3045.

37. Zhang, B.; Liu, H.; Karger, B. L.; Foret, F. *Anal. Chem.* **1999**, 71, 3258-3264.

38. Dodge, A.; Fluri, K.; Verpoorte, E.; de Rooij, N. F. *Anal. Chem.* **2001**, 73, 3400-3409.

39. Badal, M. Y.; Wong, M.; Chiem, N.; Salimi-Moosavi, H.; Harrison, D. J. *J. Chromatogr. A* **2002**, 947, 277-286.

40. Lazar, I. M.; Ramsey, R. S.; Ramsey, J. M. *Anal. Chem.* **2001**, 73, 1733-1739.

41. Belgrader, P.; Hansford, D.; Kovacs, G. T. A.; Venkateswaran, K.; Mariella, R.; Milanovich, F.; Nasarabadi, S.; Okuzumi, M.; Pourahmadi, F.; Northrup, M. A. *Anal. Chem.* **1999**, 71, 4232-4236.

42. Smith, E. M.; Xu, H.; Ewing, A. G. *Electrophoresis* **2001**, 22, 363-370.

43. Koutny, L.; Schmalzing, D.; Salas-Solano, O.; El-Difrawy, S.; Adourian, A.; Buonocore, S.; Abbey, K.; McEwan, P.; Matsudaira, P.; Ehrlich, D. *Anal. Chem.* **2000**, 72, 3388-3391.

44. Paegel, B. M.; Emrich, C. A.; Wedemayer, G. J.; Scherer, J. R.; Mathies, R. A. *Proc. Natl. Acad. Sci.* **2002**, 99, 574-579.

45. Tian, H. J.; Jaquins-Gerstl, A.; Munro, N.; Trucco, M.; Brody, L. C.; Landers, J. P. *Genomics* **2000**, 63, 25-34.

46. Munro, N. J.; Huang, Z. L.; Finegold, D. N.; Landers, J. P. *Anal. Chem.* **2000**, 72, 2765-2773.

47. Sato, K.; Tokeshi, M.; Kimura, H.; Kitamori, T. *Anal. Chem.* **2001**, 73, 1213-1218.

48. Morishima, K.; Arnold, D. W.; Wheeler, A. R.; Rakestraw, D. J.; Zare, R. N. In *Proceedings of Micro Total Analysis Systems 2000*; Kluwer Academic Publishers: Dordrecht, The Netherlands, 2000; pp 269-272.

49. Vykoukal, J.; Yang, J.; Becker, F. F.; Gascoyne, P. R. C.; Krulevitch, P.; Ackler, H.; Hamilton, J. In *Proceedings of Micro Total Analysis Systems 2000*; Kluwer Academic Publishers: Dordrecht, The Netherlands, 2000; pp 127-130.

50. Richter, A.; Plettner, A.; Hofmann, K. A.; Sandmaier, H., *Sens. Actuators A* **1991**, 29, 159-168.

51. Harris, C. M. *Anal. Chem.* **2003**, 75, 64A-69A.

52. Weigl, B. H.; Bardell, R.; Schulte, T.; Williams, C. In *Proceedings of Micro Total Analysis Systems 2000*; Kluwer Academic Publishers: Dordrecht, The Netherlands, 2000; pp 299-302.

53. Zhu, X.; Phadke, N.; Chang, J.; Cho, B.; Huh, D.; Takayama, S. In *Proceedings of Micro Total Analysis Systems 2002*; Kluwer Academic Publishers: Dordrecht, The Netherlands, 2002; pp 151-153.

54. Song, Y. J.; Zhao, T. S. *J. Micromech. Microeng.* **2001**, 11, 713-719.

55. Takahashi, K.; Ikeda, H.; Ikuta, T.; Nagayama, K.; Asano, T. In *Proceedings of Micro Total Analysis Systems 2002*; Kluwer Academic Publishers: Dordrecht, The Netherlands, 2002; pp 130-132.

56. Weng, K.-Y. In *Proceedings of Micro Total Analysis Systems 2001*; Kluwer Academic Publishers: Dordrecht, The Netherlands, 2001; pp 409-410.

57. Furdui, V. I.; Kariuki, J. K.; Harrison D. J. *J. Micromech. Microeng.* **2003**, 13, S164-S170.

58. Choi, Y. H.; Lee, S. S. In *Proceedings of Micro Total Analysis Systems 2003*; Squaw Valley, CA, USA, 2003; pp 611-614.

59. Son, S. U.; Choi, Y. H.; Lee, S. S. In *Proceedings of Micro Total Analysis Systems 2003*; Squaw Valley, CA, USA, 2003; pp 179-182.

60. Goedecke, N.; Manz, A. In *Proceedings of Micro Total Analysis Systems 2001*; Kluwer Academic Publishers: Dordrecht, The Netherlands, 2001; pp 375-376.

61. Effenhauser, C. S.; Harttig, H.; Kramer, P. In *Proceedings of Micro Total Analysis Systems 2001*; Kluwer Academic Publishers: Dordrecht, The Netherlands, 2001; pp 397-398.

62. Choi, Y. H.; Lee, S. S. In *Proceedings of Micro Total Analysis Systems 2003*; Squaw Valley, CA, USA, 2003; pp 219-222.

63. Duffy, D. C.; Gillis, H. L.; Sheppard, N. F. J.; Kellogg, G. J. *Anal. Chem.* **1999**, 71, 4669-4678.

64. Delamarche, E.; Bernard, A.; Schmid, H.; Bietsch, A.; Michel, B.; Biebuyck, H. *J. Am. Chem. Soc.* **1998**, 120, 500-508.

65. Gallardo, B. S.; Gupta, V. K.; Eagerton, F. D.; Jong, L. I.; Craig, V. S.; Shah, R. R.; Abbott, N. L. *Science* **1999**, 283, 57-60.

66. Delamarche, E.; Bernard, A.; Schmid, H.; Michel, B.; Biebuyck, H. *Science* **1997**, 276, 779-781.

67. Seidel, R. U.; Sim, D. Y.; Menz, W.; Esashi, M. *Transducers '99* **1999**, 438-441.

68. Matsumoto, S.; Klein, A.; Maeda, R. In *Proceedings of Micro Total Analysis Systems 1998*; Kluwer Academic Publishers: Dordrecht, The Netherlands, 1998; pp 395-398.

69. Olsson, A.; Enoksson, P.; Stemme, G.; Stemme, E. *J. Microelectromech. Syst.* **1997**, 6, 161-166.

70. Andersson, H.; van der Wijngaart, W.; Nilsson, P.; Enoksson, P.; Stemme, G. *Sens. Actuator, B* **2001**, 72, 259-265.

71. Schluter, M.; Mammitzsch, S.; Martens, M.; Gasso, S.; Lilienhof, H. J. In *Proceedings of Micro Total Analysis Systems 2003*; Squaw Valley, CA, USA, 2003; pp 275-278.

72. Grosjean, C.; Tai, Y. C. *Transducers '99* **1999**, 1776-1779.

73. Xie, J.; Shih, J.; Tai, Y.-C. In *Proceedings of Micro Total Analysis Systems 2003*; Squaw Valley, CA, USA, 2003; pp 865-868.

74. Unger, M. A.; Chou, H.-P.; Thorsen, T.; Scherer, A.; Quake, S. R. *Science* **2000**, 288, 113-116.

75. Hatch, A.; Kamholz, A. E.; Holman, G.; Yager, P.; Bohringer, K. F. *J. Microelectromechan. Syst.* **2001**, 10, 215-221.

76. Atencia, J.; Beebe, D. J. In *Proceedings of Micro Total Analysis Systems 2003*; Squaw Valley, CA, USA, 2003; pp 883-886.

77. Ryu, K. S.; Shaikh, K.; Liu, C. In *Proceedings of Micro Total Analysis Systems 2003*; Squaw Valley, CA, USA, 2003; pp 635-638.

78. Desmet, G.; Vervoort, N.; Clicq, D.; Baron, G. V. *J. Chromatogr. A* **2001**, 924, 111-122.

79. Lim, K.; Kim, S.; Na, K.; Park, J.-K.; Hahn, J. H. In *Proceedings of Micro Total Analysis Systems 2001*; Kluwer Academic Publishers: Dordrecht, The Netherlands, 2001; pp 401-402.

80. Felton, M. J. *Anal. Chem.* **2003**, 75, 429A-432A.

81. Quake, S. R.; Scherer, A. *Science* **2000**, 290, 1536-1540.

82. Hosokawa K.; Maeda R. *J. Micromech. Microeng.* **2000**, 10, 415-420.

83. Liu, R. H.; Yu, Q.; Beebe, D. J. *J. Microelectromechan. Syst.* **2002**, 11, 45-53.

84. Hasselbrink, E. F., Jr.; Shepodd, T. J.; Rehm, J. E. *Anal. Chem.* **2002**, 74, 4913-4918.

85. Snyder, L. R. *Anal. Chem.* **2000**, 72, 412A-420A.

86. Swart, R.; Kraak, J. C.; Poppe, H. *Trends Anal. Chem.*, **1997**, 16, 332-342.

87. Golay, M. J. E. In *Gas Chromatography 1958*; Butterworths: London, **1958**; pp 36-84.

88. Belen'kii, B. G.; Gankina, E. S.; Mal'tsev, V. G. Capillary Liquid Chromatography; Plenum: New York, **1987**.

89. Nota, G.; Marrino, G.; Buonocore, V.; Ballio, A. *J. Chromatogr.* **1970**, 46, 103-106.

90. Fan, Z. H.; Harrison, D. J. *Anal. Chem.* **1993**, 66, 177-184.

91. Liu, M.-K.; Li, P.; Giddings, J. C. *Prot. Sci.* **1993**, 2, 1520-1531.

92. Ocvirk, G.; Verpoorte, E.; Manz, A.; Grasserbauer, M.; Widmer, H. M. *Anal. Methods Instrumen.* **1995**, 2, 74-82.

93. Golubovic, N. C.; Kang, Q.; Henderson, H. T.; Pinto, N. In *Part of SPIE Conf. on Microfluidic Devices and Systems*, Santa Clara, CA, Sept. 1998; pp 86-93.

94. Shercliff, J. A. *A Textbook of Magnetohydrodynamics,* Pergamon, Oxford, 1965.

95. Faraday, M. *Phil. Trans. Roy. Soc.* **1832**, 163 et seq.

96. Ritchie, W. *Phil. Trans. Roy. Soc.* **1832**, 294.

97. Meier, D. L.; Koide, S.; Uchida, Y. *Science*, **2001**, 291, 84-92.

98. Foust, O. J. (Ed.) *Sodium-NaK Engineering Handbook. IV. Sodium Pumps, Valves, Piping, and Auxiliary Equipment*, Gordon & Breach, New York, 1978.

99. Branover, H. *Magnetohydrodynamic Flow in Ducts*, John Wiley & Sons, New York, 1978.

100. *IEE Rev.* **1991**, 37, 45.

101. Jang, J.; Lee, S. In *ASME International Mechanical Engineering Congress and Exposition*, Anaheim, CA, 15–20 November 1998, pp. 439–443.

102. Jang, J.; Lee, S. *Sens. Actuators A* **2000**, 80, 84–89.

103. Huang, L., Wang, W., Murphy, M. C., Lian, K., Ling, Z. G., *Microsystem Tech.* **2000**, 6, 235-240.

104. Zhong, J.; Yi, M.; Bau, H. H. *Sens. Actuators A* **2002**, 96, 59-66.

105. Bau, H. H.; Zhong, J.; Yi, M. *Sens. Actuators B* **2001**, 79, 207-215.

106. Yi, M.; Qian, S.; Bau, H. H. *J. Fluid Mech.* **2002**, 468, 153-177.

107. Qian, S.; Zhu, J.; Bau, H. H. *Phys. Fluids* **2002**, 14, 3584-3592.

108. Bau, H. H.; Zhu, J.; Qian, S.; Xiang, Y. *Sens. Actuators B* **2003**, 88, 205-216.

109. Xiang, Y.; Bau, H. H. *Phys. Rev. E* **2003**, 68, 016312, 11 pages.

110. Schasfoort, R. B. M., Lűttge, R., van den Berg, A., In *Proceedings of Micro Total Analysis Systems 2001*; Kluwer Academic Publishers: Dordrecht, The Netherlands, 2001; pp 577-578.

111. Heng, K.-H.; Huang, L.; Wang, W.; Murphy, M. C. *SPIE* **1999**, 3877, 66–73.

112. Gong, Q.; Zhou, Z. *Transducer '99* **1999**, 466-469.

113. Gong, Q.; Zhou, Z.; Yang, Y.; Wang, X. *Sens. Actuators A* **2000**, 83, 200-207.

114. Lemoff, A. V., Lee, A. P., Miles, R. R., McConaghy, C. F., *Transducers '99* **1999**, 1126-1129.

115. Lemoff, A. V.; Lee, A. P. *Sens. Actuators B* **2000**, 63, 178–185.

116. Lemoff, A. V., Lee, A. P., In *Proceedings of Micro Total Analysis Systems 2000*; Kluwer Academic Publishers: Dordrecht, The Netherlands, 2000; pp 571-574.

117. Eijkel, J. C.T., Dalton, C., Hayden, C. J., Drysdale, J. A., Kwok, Y. C., Manz, A., In *Proceedings of Micro Total Analysis Systems 2001*; Kluwer Academic Publishers: Dordrecht, The Netherlands, 2001; pp 541-542.

118. Eijkel, J. C. T.; Dalton, C.; Hayden, C. J.; Burt, J. P. H.; Manz, A. *Sens. Actuators B* **2003**, 92, 215-221.

119. Senturia, S. D.; Schmidt, M. A.; Harrison, D. J. *Microsystems: Mechanical, Chemical, Optical*, Lecture Notes, Massachusetts Institute of Technology, **1998**.

120. Walker M. J. In *Proc. SPIE: MEMS Design, Fabrication, Characterization, and Packaging*, **2001**, 4407, 89-99.

121. Judy J. W. http://www.ee.ucla.edu/research/judylab/procedures/.

122. Banerjee, G.; So, J.; Mikkola, B. *Solid State Tech.* **2001**, 44 (11), 83-88.

123. Wrschka, P.; Hernandez, J.; Oehrlein, G. S.; Negrych, J. A.; Haag, G.; Rau, P.; Curriec; J. E. *J. Electrochem. Soc.* **2001**, 148, G321-G325.

124. Nguyen, V. H.; Hof, A. J.; van Kranenburg, H.; Woerlee, P. H.; Weimar, F. *Microelectron. Eng.* **2001**, 55, 305-312.

125. Hauder, M.; Gstottner, J.; Gao, L.; Schmitt-Landsiedel, D. *Microelectron. Eng.* **2002**, 64, 73-79.

Chapter 2

Fluid Dynamics in Microfluidic Networks with Micron Sized Flow Restrictors

2.1 Introduction

Control of the direction of fluid flow within a network of flow paths in a microfluidic device is paramount to its proper operation (1). Control of pressure driven flow requires active valving, or else passive control, through variation of the flow resistance of each intersecting channel by adjusting their geometry. Flow restrictors in a microfluidic system must have at least one dimension of a few microns or less, given typical channels sizes of 10 – 300 μm. In order to achieve rational design of passive flow control with such flow restrictors, an accurate model describing fluid flow must be available. The Navier-Stokes equations provide the basis for modeling fluid flow, and their common solutions in the form of the Hagen-Poisseuille equations are routinely employed to describe flow (2, 3). However, what few studies exist on flow in microfluidic systems have suggested these equations may not be entirely suitable. Pfahler *et al.* (4) evaluated flow in microchannels 0.8 and 1.7 μm deep, and 100 μm wide, reporting significant deviations of ~ +300 % and -20 %, respectively, from predictions based upon the Navier-Stokes equations. More recent studies in channels with hydraulic

diameters of 50-250 μm showed there is a modest deviation in friction factor from Poisseuille flow theory, and that the onset of turbulent flow may occur at much lower Reynolds number than expected (5-8). These uncertainties require an evaluation of the suitability of the Poisseuille solutions to the Navier-Stokes equations for use as a design tool for microchannels with dimensions on the scale of 1 μm.

Evaluation of the Navier-Stokes equations and its solutions requires accurate measurement of the relationship between flow rate and pressure. A variety of particle based techniques, such as particle imaging velocimetry (9, 10) or laser Doppler (11, 12) methods, have been applied in chips with dimensions > 10 μm. However, particles should be much smaller than 1 μm to evaluate a 1 μm flow path, making such methods less suitable. Here we have used a time-of-flight approach, in which photobleaching creates a dye zone of reduced concentration in a flowing fluorescent dye stream, whose time of travel can be monitored with fluorescence detection. The method is related to that of optical gating used by Monig and Jorgenson (13-15), and to transport studies using optically released caged fluorescent dyes, but instead uses fluorescein photobleaching.

Because 1 μm deep channels are very susceptible to plugging, devices were designed with a short, shallow weir zone (1-3 μm deep, ~ 280 - 290 μm wide and 18-32 μm long) to create the flow constriction, accessed with 10 μm deep channels in which the flow measurements were made. Flow in such broad shallow channels can be

approximated as two dimensional flow, and will be termed *slot flow* here. Linear flow rates measured in these straight channels were quantitatively compared to the predictions of the Hagen-Poisseuille equation for rectangular geometries using the equations developed below. Flow rates were then measured within a network of channels and flow restrictors, and the resulting values were compared to predictions based upon the Hagen-Poisseuille equation. A three-port, double weir device we have developed for capillary electrochromatography and other applications (16, 17) was used for those tests. Wide channels in that device could be described as rectangular, but channels with an aspect ratio (width to depth) greater than 0.1-0.2, prepared by isotropic etching (18), have a D-shape that is not treated by published solutions to the Navier-Stokes equation. In order to account for the effect of this shape, computational fluid dynamics modeling (3, 19) was employed to provide a working curve relating the geometric form factor for a D-shaped channel to that of a rectangular channel with the same aspect ratio of depth to width (d/W). This report thus presents a means to measure linear flow velocity within a microfluidic chip, correlates linear velocity with volumetric flow rate, evaluates the accuracy of the Hagen-Poisseuille equation in 1 μm deep flow channels, and test the model's ability to describe the proportioning of flow within a network of flow channels.

2.2 Theory of Flow Velocity Parameters Measured in Slot Flow

The flow velocity measurement method employed in this study evaluated the flow rate in the centre of a wide, shallow, rectangular channel, which exhibits slot flow. In order to evaluate the measured linear velocity of a moving dye front, the solutions to the Navier-Stokes equation were evaluated to obtain the average flow across the channel depth (y-direction), and the maximum velocity across the channel width (x-direction). The coordinate system is defined in Figure 2.1. For an incompressible, constant-viscosity fluid flow through a rectangular cross-section, the Navier-Stokes equation and boundary conditions can be written (2) as:

$$\frac{\partial^2 V_z}{\partial x^2}+\frac{\partial^2 V_z}{\partial y^2}=\frac{1}{\eta}\left(-\frac{dp}{dz}\right) \text{ with } \quad V_z=0 \text{ at } x=\pm W/2 \text{ and } y=\pm \mathrm{d}/2 \tag{2.1}$$

where V_z, p, η stand for the velocity along the flow channel, the pressure, and the viscosity of the liquid, respectively. W and d are the width and depth of the channel.

Solving Equation 2.1 and then integrating across the y-axis yields the average velocity across the y-dimension, $\overline{V_z}(x)$,

$$\overline{V_z}(x)=\frac{\mathrm{d}^2}{4\eta}\left(-\frac{dp}{dz}\right)\cdot\left\{\frac{1}{3}-\frac{32}{\pi^4}\sum_{n=0}^{\infty}\frac{\cosh\left[\frac{(2n+1)\pi x}{\mathrm{d}}\right]}{(2n+1)^4\cosh\left[\frac{(2n+1)\pi W}{2\mathrm{d}}\right]}\right\}\equiv\frac{d^2G(x)}{4\eta}\left(-\frac{dp}{dz}\right) \tag{2.2}$$

where the function $G(x)$ is a maximum at the center of the channel (x = 0). However, for slot flow, $G(x)$ varies rapidly only at the channel edges, and is close to constant across

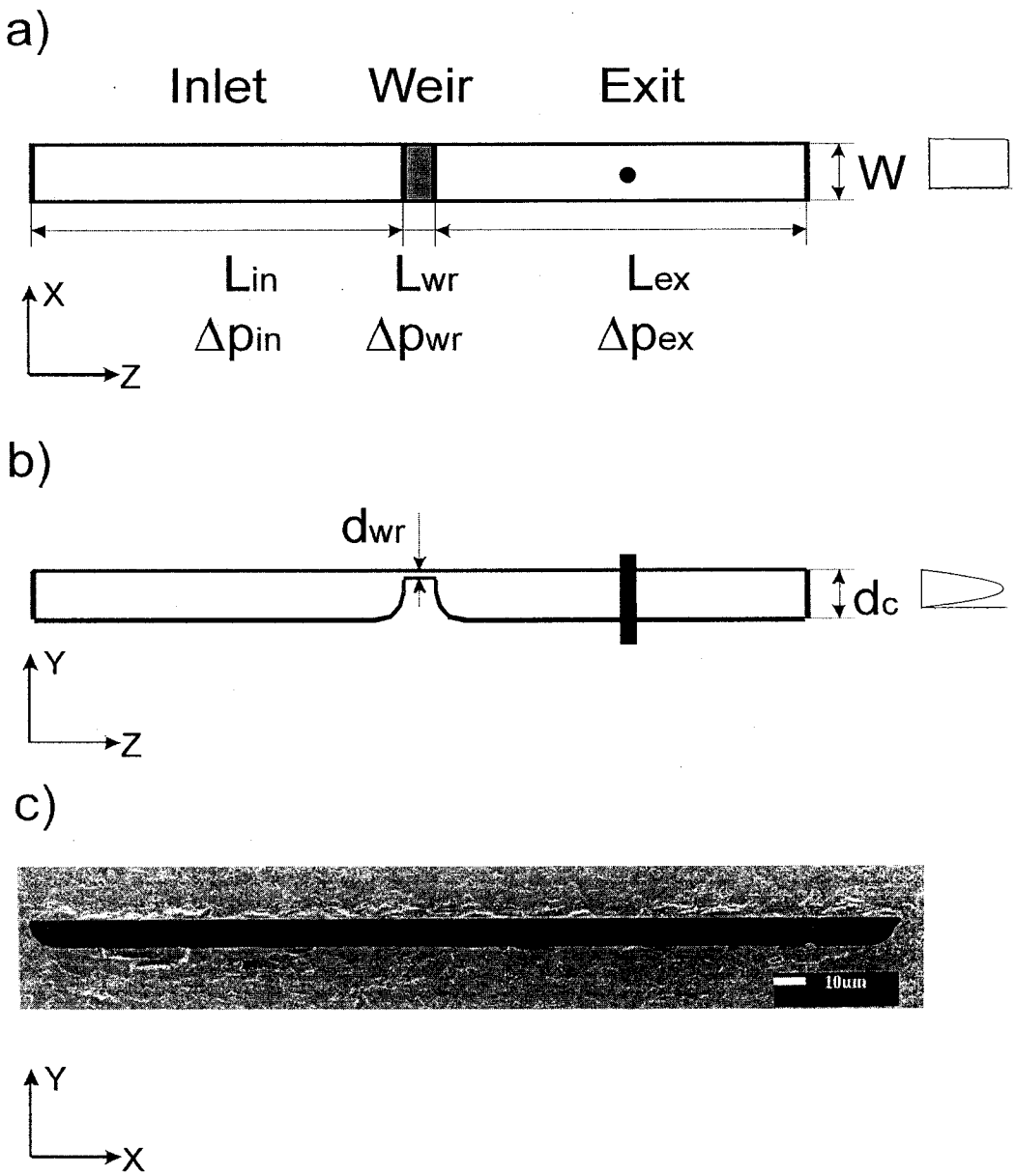

Figure 2.1. Geometry of single channel layout, showing the inlet (in), exit (ex) and weir (wr) segments. Also shown are the coordinate system, pressure drops, and channel dimension symbols used in the mathematical analysis. Nominal channel width and depth was 290 and 10 μm, respectively. Weirs were nominally either 1 or 3 μm deep. The insets show, a) the flow profile along the x-axis, top view, calculated using Equation 2.2, and b) along the y-axis, side view, as calculated form the solution to Equation 2.2. The solid circle and bar show the laser spot used to measure flow velocity. Image c) shows an electron micrograph of the channel cross section.

most of the channel, as illustrated by an inset in Figure 2.1. Thus, for a measurement made near the centre of the channel, as is the case for the fluorescence probe technique employed in this study, the linear flow velocity observed is given by

$$\overline{V_z}(0) = \frac{\mathrm{d}^2}{4\eta}\left(-\frac{dp}{dz}\right)\cdot\left\{\frac{1}{3} - \frac{32}{\pi^4}\sum_{n=0}^{\infty}\frac{1}{(2n+1)^4 \cosh\left[\frac{(2n+1)\pi W}{2\mathrm{d}}\right]}\right\} \tag{2.3}$$

Equation 2.2 may be further integrated over x = -W/2 to +W/2 to give the Hagen-Poisseuille equation (2, 3)

$$Q = \frac{W^2 d^2 F}{4\eta}\left(-\frac{dp}{dz}\right) \tag{2.4}$$

where Q is the volumetric flow rate, and F is a geometric form factor for a rectangular channel given by

$$F = \frac{W}{3\mathrm{d}} - \frac{64W^2}{\pi^5 \mathrm{d}^2}\sum_{n=0}^{\infty}\frac{\tanh\left[\frac{(2n+1)\pi \mathrm{d}}{2W}\right]}{(2n+1)^5} \tag{2.5}$$

Equations 2.4 and 2.5 show that the volumetric flow rate is a complex function of the aspect ratio of the channel, d/W, and the square of the cross-sectional area, Wd. For a channel with a constriction along the flow path, such as the devices studied here, the volumetric flow rate, Q, through each region must still be equal. Referring to Figure 2.1 we can write

$$\Delta p = \Delta p_{in} + \Delta p_{ex} + \Delta p_{wr} \tag{2.6}$$

where the subscripts refer to pressure drops in the inlet, exit and weir segments of the channel, respectively. Assuming each channel segment is long enough for flow to become fully developed so that the pressure gradient is linear along the segment, the differential in Equation 2.4 becomes $\Delta p_i/L_i$ where i refers to a given channel segment, L_i is its length, and Δp_i is defined as the high p minus the low p. Using Equation 2.4 we can also write,

$$\Delta p_{in} + \Delta p_{ex} = Q\frac{4\eta(L_{in} + L_{ex})}{W^2 d_{in}^2 F_{in}} \tag{2.7}$$

since in our devices W and d up- and downstream of the weir were the same. The fraction of pressure drop across the deeper channel segments is given by combining Equations 2.6 and 2.7 to obtain

$$\frac{\Delta p_{in} + \Delta p_{ex}}{\Delta p} = \frac{(L_{in} + L_{ex})}{d_{in}^2 F_{in}} \Bigg/ \left[\frac{(L_{in} + L_{ex})}{d_{in}^2 F_{in}} + \frac{L_{wr}}{d_{wr}^2 F_{wr}}\right] \tag{2.8}$$

Equation 2.8 relates the pressure drop in the deep channel segments to the total pressure drop along a channel. Used in combination with Equation 2.3, and recognizing that *dp/dz* is a constant in the deep channels due to their equal cross-sections, we obtain a relationship between the observable parameters of linear velocity and total pressure drop

$$\overline{V_z}(0) = \frac{\frac{1}{F_{in}}}{\frac{4\eta(L_{in} + L_{ex})}{d_{in}^2 F_{in}} + \frac{4\eta L_{wr}}{d_{wr}^2 F_{wr}}} \cdot \left\{\frac{1}{3} - \frac{32}{\pi^4}\sum_{n=0}^{\infty}\frac{1}{(2n+1)^4 \cosh\left[\frac{(2n+1)\pi W}{2d_{in}}\right]}\right\} \cdot \Delta p \tag{2.9}$$

Evaluation of the quantitative relationship between these two measured variables can then be used to determine the suitability of the Navier-Stokes and Hagen-Poisseuille equations for describing flow in micron-scale channels.

2.3 Experimental Section

2.3.1 Device Fabrication

Devices were fabricated in Corning 0211 glass (Corning Glass, Parkride, IL) at the University of Alberta NanoFab Lab, using published procedures (18). A two mask process was used to fabricate the weir structure. Channels were etched to ~ 10 μm deep, and weirs were etched to either 1 or 3 μm deep; exact depths were determined using an Alpha Step 200 profilometer (Tencor Instr., San Jose, CA) to a precision of ± 0.005 μm. Channel and weir dimensions were determined by optical microscopy, using a reticle and etched scale, and were confirmed by electron microscopy (Jeol X-version JSM 6301 FXV, Peabody. MA) to precisions of 0.5 μm or 20 nm, respectively. A two-port, single channel design illustrated in Figure 2.1 was used, with typical channel widths of 290 μm and weir lengths of 19-32 μm. For 3-port devices approximate, typical widths were 600 μm for the inlet and outlet channels, 280 μm for the weirs, and 40 μm for the side channel.

2.3.2 Reagents

Fluorescein disodium salt (Sigma, St. Louis, MO) was used as received. Distilled water was polished with a Milli-Q UV Plus Ultra-PureMillipore system (Mississauga, ON, Canada). The water used as solvent was prepared by mixing fully degassed water and fully oxygen-saturated water in a 1:1 ratio, into which fluorescein was dissolved at 190 nM. Polished water was degassed by boiling, transferred to a centrifuge tube and capped with no included air volume, then cooled in a water bath to room temperature. A portion of the degassed water was fully oxygen saturated by sparging with O_2 (Praxair, Mississauga, ON, Canada) overnight. Solutions were passed through a 0.22 μm pore size filter (Millipore, Bedford, MA) before being introduced to the dye reservoir.

2.3.3 Pump System and Microchip Operation

Figure 2.2 illustrates the constant pressure pump system utilized. A gas cylinder and regulator was used to pressurize a gas and solvent reservoir, consisting of a poly(ethylene) tube (7 mm o.d., 5 mm i.d, ~35 cm length) and a copper tube connected to the regulator, with a total volume of ~13.5 mL. The aluminum foil-wrapped (to avoid photo reactions) plastic tube was charged with 3 mL of solution, the system sealed and the pressure applied. Once the pressure reached the required value a valve was closed to isolate the gas and liquid reservoirs from the cylinder. At the highest flow rate pressure

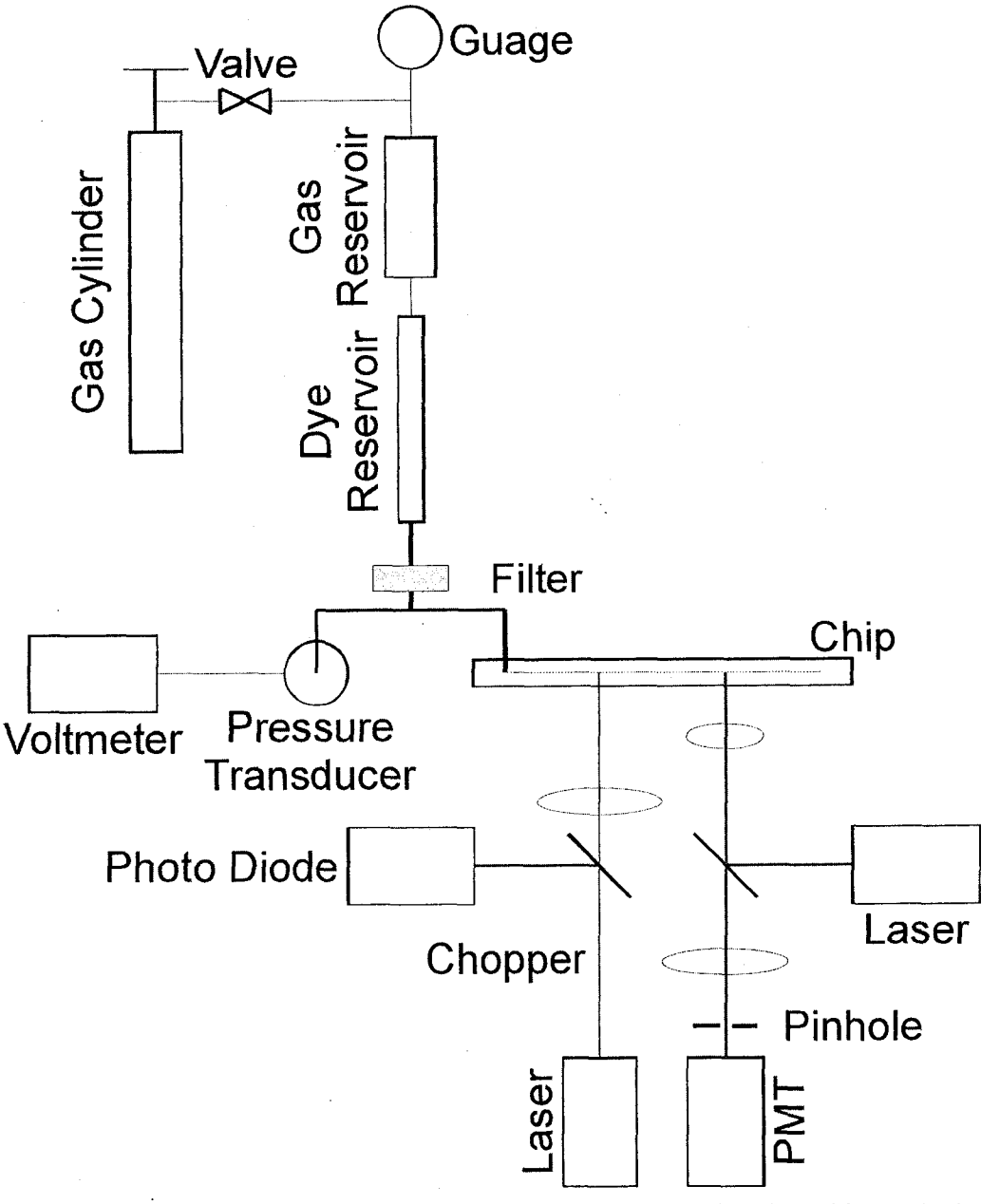

Figure 2.2. Diagram of apparatus used for time of flight, photobleaching velocity measurement technique. Pressure was developed with a gas cylinder, reservoirs were made from poly(ethylene) tubing, a 0.5 μm filter was used to remove particulates. Two lasers and a variety of lenses were used for photobleaching and fluorescence detection. A micrometer was used to set the distance between the bleaching and fluorescence detection spots.

dropped by < 0.3 % over the course of measurement, no observed pressure change was seen at mid or low flow rates. A frit-in-a-ferrule (0.5 μm pore size, Upchurch, Oak Harbor, WA) was added upstream of the pressure sensor. A micro pressure transducer (NPC-1210-015-D-3L, Lucas, Fremont, CA) monitored the pressure drop across the device relative to the atmosphere, using a 10 ppm resolution voltmeter (Hewlett-Packard Model 3468A Multimeter, Palo Alto, CA) for readout. The transducer was calibrated with a Hg filled U-tube connected in place of the chip, mounted vertically using a plumb bob, interpolating to 0.2 mm using graph paper marked to 1 mm-resolution for a scale. The transducer was always kept on after each calibration. The chip was mounted in an aluminum holder and a flangeless nut (Upchurch, Oak Harbor, WA) and a frit-in-a-ferrule coupling was used to connect the pressurized source to the inlet. Room temperature was monitored by a thermometer (0.01K, VWR), to allow selection of water-viscosity values from tabulated results.

2.3.4 Linear Flow Velocity Measurements

The time of flight of a photobleached zone of dye was measured in order to determine velocity. A 190 nM fluorescein solution proved to be optimal; dilute enough to reduce dye-dye interactions that result in aggregate formation (20-22) during photo-bleaching, but high enough to give a strong signal. A 50 % O_2 saturated solution

was used to reduce dye aggregate formation, as O_2 reaction with the excited optical state competes with dye-dye interactions. Higher O_2 concentrations caused bubble formation at the weirs. Figure 2.2 illustrates the time of flight detection apparatus. Two 488 nm Ar ion lasers (Uniphase-Cyonics, San Jose, CA) were used; one laser operated at 2.5-12 mW was focused (plano-convex, f=150 mm, Newport, Irvine, CA) to a 50 μm diam. spot to photobleach the dye. The intensity increased as the flow rate was increased. A chopper was operated at 0.5 Hz to generate a square wave dye concentration variation, alternately directing the beam between the chip and a photodiode (ϕ3 mm, Silicon Detector Corp., Newbury Park, CA). The second laser (~2.5 mW, ~25 μm spot size) was used for laser induced fluorescence detection using an inverted, confocal, epiluminescent, infinite optical conjugation, microscope built in-house (23). A 10X objective (5709, New Focus, Santa Clara, CA), 20 cm f.l. tube lens (Achromat, Newport, PAC064), and a 200 μm pinhole (Newport, Irvine, CA) were used to observe a 20 μm detection zone. The distance between the bleaching point and the detection points was set using a calibrated translation stage (423 stage with SM-13 micrometer, Newport, Irvine, CA, USA), with a positioning error < 1 μm. Signals, shown in Figure 2.3, were monitored with a Pentium 1, 75 Mhz computer, equipped with a National Instruments PC+ board, and Labview Software v.4 (Austin, TX). A 25 kHz acquisition rate was used, but 250 points were averaged in blocks to yield a 100 Hz, net acquisition rate. Data was processed using

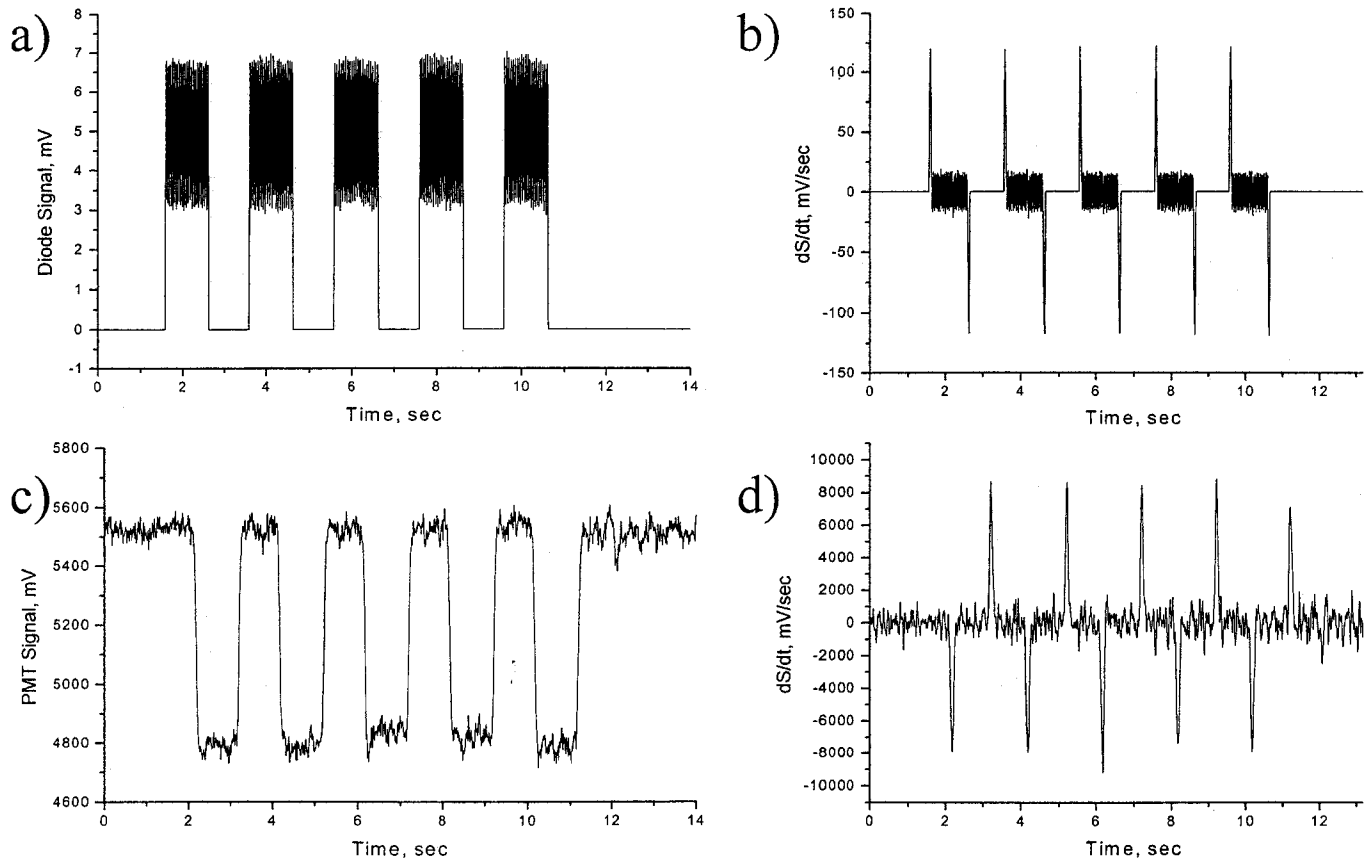

Figure 2.3. Four images illustrating the time of flight measurement of flow velocity: a) chopped laser beam used to bleach dye upstream of the weir, measured with a photodiode, b) differentiated photodiode signal used to highlight edges of the bleached spot, c) fluorescence intensity measured downstream of bleaching spot, d) differentiated fluorescence signal used to highlight edges in the bleached spot rise and fall. The time required for the edge to travel from the bleaching point was used to determine flow velocity, according to the specific method described in the text, Equation 2.10.

Origin v5.0 (Microcal, Northampton, MA) by differentiation, using a 13-point Savitsky-Golay algorithm included with Origin, to allow ready determination of the edges of the photobleached spot. Data was measured first 1 mm away from the bleaching point, and the time of flight from the bleached spot was determined for about 5 pulse periods. The detector was then translated 2.000 mm away from the first observation point, and time of flight was again determined from the bleached spot. These measurements were more than 1 cm downstream of the weir for the single channel devices. For the three port devices a pair of such measurements were made first 1 cm upstream and then 1 cm downstream of the weir structures, and at least 1 cm from any corners. Because photoproducts could plug the weir, measurements upstream of the weir in the three-port device were limited to durations of 1 min at each pressure. No plugging, as evidenced by stable flow rates over time, were seen when measurements were made downstream of the weir.

2.3.5 Finite Element Modeling

FlumeCAD software (Version 4.8.3, Coventor, Cary, NC) were employed for simulating the D-shaped cross-section generated by isotropic etching. Linear flow velocity was the only numeric output readily supplied by the software (24). Consequently, two simulations were made in parallel for each given channel dimension

simulated; in one a pressure (typically 1 Pa) was applied, in the other a volumetric flowrate (typically 1 pl/sec) was used. The linear flow velocity output in numeric form from both runs was then used to establish the relationship between pressure and volumetric flow rate. The pressure-flow rate relationship obtained was then compared to the Hagen-Poisseuille equation for rectangular flow channels and an effective form factor, F_D, for using that equation to describe flow in a D-shaped cross-section was determined. Simulations were performed on a Sun Microsystems Ultra 10 (Palo Alto, CA), using a depth of 10 μm, a variable width and a length ten times the width.

Choosing the proper mesh size is important for a finite element method (FEM). All channels dimensions were simulated for both rectangular and D-shapes, and the results for the rectangular shape were compared to the results of the Hagen-Poisseuille equation. The mesh was adjusted until the results of the simulation and the Hagen-Poisseuille equation agreed within 3 %. The ratio between simulated and calculated results was used to correct the simulated values for both rectangular and D-shaped channels of the same aspect ratio. For example, for a d/W ratio of 0.333, using 36 elements in the cross section gave simulations that matched the Hagen-Poisseuille equation, as long as there were over 30 elements along the direction of flow. When the number of elements along the flow was only 10, the calculation was stable only when the number of cross-sectional elements was over 60. We thus selected 60 elements in the

cross section and 30 elements along the flow direction. A 27-node brick was used as the element, and a parabolic function was used for interpolation during the simulation. Larger numbers of nodes, or longer channels, tended to produce out of memory errors. This same approach was applied to all channel geometries, and we achieved less than 3 % deviation for all but one case. For an aspect ratio of 0.05 a 10 % deviation between simulated and calculated values was accepted, because the mesh could not be set finer due to memory constraints.

2.4 Results and Discussion

Our evaluation of the use of fluid restrictors to control flow in microfluidic devices, and the appropriateness of using the predictions of the Navier-Stokes equation to design such flow restrictors, can be broken down into several steps. We first needed to develop a method to accurately measure flow velocity within the microchannels. The flow rates measured in a straight line channel with a single constriction were then quantitatively compared to the predictions of the Hagen-Poisseuille equation, in order to establish the relevance of the equation for flow in the microchip. Finally, flow rates were measured in a network of channels and flow restrictors, and the resulting values were compared to predictions based upon the Hagen-Poisseuille equation. Computational fluid dynamics modeling was required to accurately make the latter assessment, due to the

non-rectangular cross section of small, isotropically etched flow channels. Each of these steps is discussed in detail below.

2.4.1 Flow Rate Measurements

Linear flow velocity was measured using a fluorescent dye and a photobleaching technique to create a plug of reduced dye concentration. The time of flight of the bleached plug was then determined by measuring at two locations downstream of the bleaching site (Figure 2.4), allowing the velocity to be determined using Equation 2.10.

$$V = \frac{L_2 - L_1}{t_2 - t_1} \tag{2.10}$$

The locations L_1 and L_2 were 1 and 3 mm downstream of the bleaching spot, respectively, while t refers to the time the edge of the bleached zone transits the detector

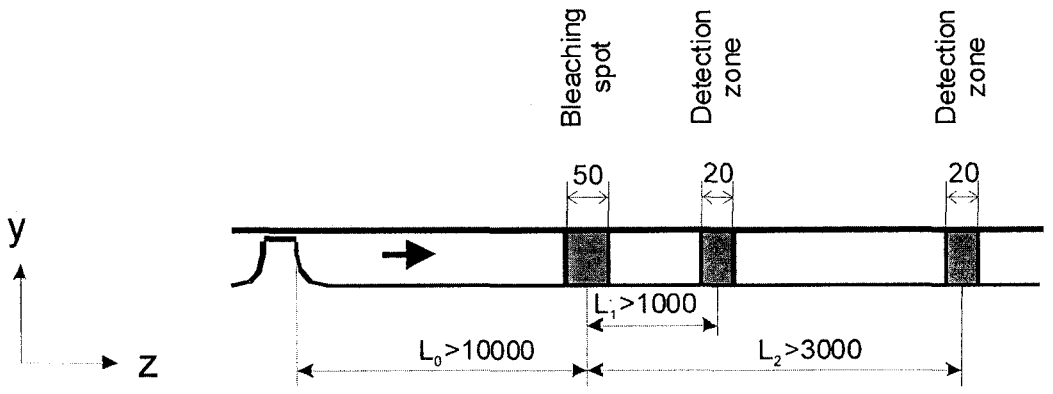

Figure 2.4 Dual-point flow velocity measurement. Each measurement of the velocity was performed by two parallel photobleaching tests so as to reduce the error from the size of the bleaching and detection spots, and from the bleaching response time, etc. Units are in microns.

at that location. Figure 2.3 illustrates the laser bleaching pulses generated by a chopper, and the fluorescence changes observed downstream as a result of bleaching. To improve precision, the data was differentiated, and the peaks were used to determine the edges of the bleached zone, as indicated in Figure 2.3d. The phase shift in the position of the edges for any given bleached zone gave the time $t_{1 \text{ or } 2}$ required to travel from the bleaching zone. While absolute values relative to the bleaching spot could have been employed, using Equation 2.10 gives greater precision, as the distance between the two detection zones can be set within 1-2 μm. Additionally, for greatest accuracy we require that relaxation of the shape of the bleached zone arising from Taylor dispersion be fully developed in the directions perpendicular to the direction of flow. At both detection zones this is the case, as discussed below.

The channels used for velocity measurements in this study are slot shaped, being much wider than they are deep. The slight deviation from a rectangular shape due to isotropic etching of the channels, illustrated in Figure 2.1, can be neglected in slot flow. Across the width of the channel, the x-coordinate, slot flow gives a nearly uniform flow velocity profile, making the measurement independent of exact position near the channel center, and tolerant of the finite size of the measuring spot. Calculations using Equation 2.2 indicate the flow velocity $\overline{V_z}(x)$ is essentially constant across ~80 % of a 200 μm-wide inlet and outlet channels. So for channels 280 μm wide or more we were readily

able to use a bleaching laser spot size of 50 μm and a fluorescent measurement (probe) spot size of ~20 μm. In the vertical direction, the y-coordinate, the fluorescence measurement will give the average velocity as given by Equation 2.3.

Flow velocity must be measured in a region of fully developed flow, unaffected by entrance effects and other factors. The flow velocity profile is considered to have reached steady state after a length of 0.06dRe (3), where d is the characteristic dimension of the flow channel and Re is the Reynolds number, given by $V d\rho/\eta$. For an average linear flow rate of 10 mm/s in the inlet channel the velocity will be 100 mm/s in the weir. Taking a characteristic channel dimension of 2 μm, using a density, ρ, of 10^3 kg/m^3 and a viscosity, η, of 10^{-3} Pa•s, gives Re = 0.2, and a required entrance length of 0.024 μm. For a 3 μm deep weir, with a 6 μm characteristic dimension we estimate a length of 0.072 μm is required. Thus, the 19-32 μm long weirs used in this study will reach fully developed flow. Downstream of a weir the same calculations for 10 mm/s give an entrance length of 0.24 μm. The detector was located at least 1 cm from the weir, so that flow velocity was fully developed.

The concentration plug generated by photobleaching must become fully developed in terms of radial (or lateral) Taylor-Aris dispersion, and so we must consider diffusion in the radial direction in order to evaluate the required distance downstream. Figure 2.1 illustrates the coordinate system used in this analysis. Diffusion in the z

direction reduces the magnitude of the fluorescence signal change caused by bleaching, but does not affect the travel time. In the x, y directions, the velocity vectors are zero. Given that we have slot flow and are measuring near the centre of the channel there is no local concentration gradient in the x direction. As a result the relevant time dependent concentration term for establishing a fully developed plug profile, $\partial C/\partial t$, is governed primarily by diffusion in the y direction and must be of the same order as $D_f(\partial^2 C/\partial y^2)$, where D_f is the dye diffusion coefficient (25). Near the top and bottom edges of the flow channel, where y ~ ±d/2 we have, by analogy to the case for a cylindrical geometry

$$\frac{L_D}{V_z} \sim \frac{(d/2)^2}{D_f} \tag{2.11}$$

where L_D is the required distance downstream from the bleaching zone for fully developed flow. For the channel depth of 10 μm used here, a typical higher velocity of 10 mm/sec, and a fluorescein diffusion coefficient of 3.3×10^{-10} m^2/sec (18), the development length is ~ 760 μm. So the initial detection point 1 mm from the bleaching point should be sufficiently far downstream. In fact, no deviation was observed even at velocities of ~ 15 mm/sec, as seen in Figure 2.5.

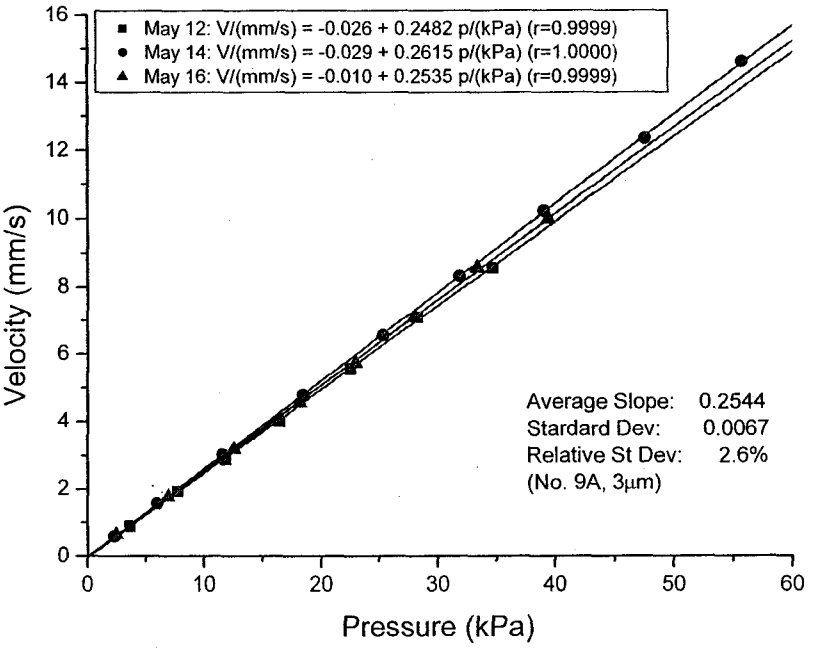

Figure 2.5. Plot of flow velocity versus applied pressure for a two-port, single channel device (Figure 2.1), determined on three different days (T = 23.5, 24.3 and 23.0 °C), illustrating the very small deviations observed over time. Device 9A: channel width 294 μm, depth 10.25 μm, length 35.01 mm; weir width 294 μm, depth 3.03 μm, length 32 μm. Bleaching laser 10 mW, detection laser 2.5 mW, PMT bias 500 V.

Figure 2.5 shows typical velocity-pressure responses for a 3-μm deep weir device; complete dimensions are given in Table 2.1. Each data point is the average of ~30 individual velocity measurements, and has a precision of ± 0.5 %. Individual curves show extremely high linearity, with r^2 = 0.9999 to 1.0000, and a typical rsd in the slope of ± 0.5 %. The intercepts were always within one sd of zero. There was some change in slope over time, however, with an rsd of ± 2.6 % measured over a 5 day period. This variation can be attributed to contamination of the channels and weir due to flow of solvent,

requiring careful preparation of the solutions to achieve a variation this small. These data indicate our apparatus can provide reproducible measurements of the linear velocity in a slot shaped microchannel.

Table 2.1. Two-port channel dimensions

No.	Channel			Weir		
	W(a)	D	L(b)	W(a)	D	L
9A	294	10.25	35090	294	3.03	32
9D	293	10.20	34630	293	3.04	22
7A	290	10.05	35090	290	0.99	30
7D	290	9.96	34630	290	1.02	19

a) The widths of the channel and the weir are the same;
b) The total length of the inlet and exit segments.

2.4.2 Comparison of Experimental Flow Velocity with the Hagen-Poisseuille Equation

The flow velocity was determined as a function of pressure for four different device layouts (Figure 2.6) with the layout shown in Figure 2.1, and specific dimensions given in Table 2.1. The weir acted as a flow restrictor, reducing the slope of the velocity-pressure curves as the weir depth decreased or the weir length increased. The observed slopes are reported in Table 2.2. The volume flow rate and pressure relationship that is predicted according to the Hagen-Poisseuille equation can be related to the linear

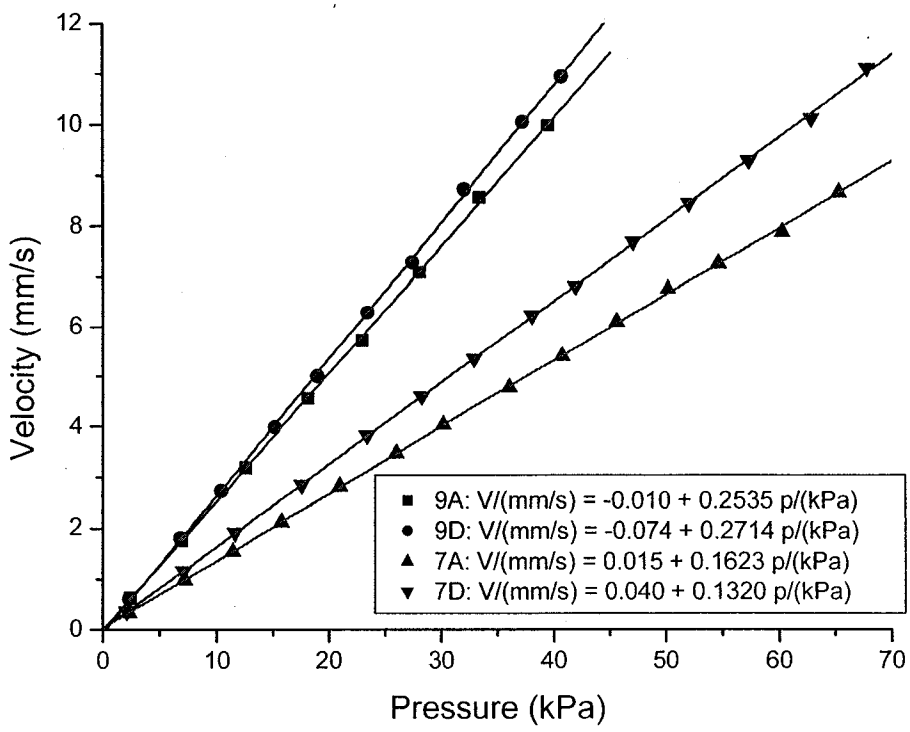

Figure 2.6. Plot of flow velocity versus applied pressure for four different two-port, single channel devices, with different weir depth. Device 9A, 9D: weir depth ~ 3 μm; device 7A, 7D: weir depth ~ 1 μm.

flow rate vs pressure using Equation 2.9, developed in section 2.2. Because of the low fluorescein concentration the viscosity used was that of pure water. The measured device dimensions were used in the calculation, assuming a rectangular shape. The calculated slopes are also reported in Table 2.2, along with the % deviation of the calculated value relative to the experimental value.

Table 2.2. Comparison of experimental slopes with those from the Navier-Stokes equations for two-port devices

No.	t	η^a	Resist%[b]	Slope(cal)	Slope(exp)	Dev%
	(C)	(mPas)		(mm/kPas)	(mm/kPas)	
9A	23.0	0.9416	3.4	0.2561	0.2535	1.0
9D	23.8	0.9205	2.3	0.2657	0.2714	-2.1
7A	23.0	0.9430	46.7	0.1355	0.1320	2.7
7D	23.0	0.9430	33.8	0.1676	0.1623	3.3

a) the viscosity was calculated by $\eta = 1.793\times10^{-3} - 4.732\times10^{-5}t + 4.48\times10^{-7}t^2$, an empirical equation based on the data in (26);
b) Resist% represents the contribution of the weir on the flow resistance;
c) Slope(cal) was calculated by Equation 2.9.

The deviation between theory and experiment indicated in Table 2.2 is 3 % or less. Experimental error for any given slope is < 0.5 %, but the variation of slope over time of ± 2.6 % is a more reliable estimate of the absolute precision of each measurement. Thus, the observed deviations are within our estimated experimental error. While some local heating due to photobleaching is expected, the magnitude of temperature change should be in the range of 0.1 to 0.3 degrees (27), so that systematic bias in the results should be significant. The observed deviation between theory and experiment for 1 μm-deep weirs was slightly larger than for 3 μm-deep weirs, but the precision of our data leads us to conclude that there is no measurable deviation from the

predictions of the Navier-Stokes and Hagen-Poisseuille equations for flow in glass channels with a dimension ≥ 1 μm.

By comparing Equations 2.2 and 2.4, experimental flow velocities can be transferred into the volumetric velocities, which is a basic parameter for the design of microchip. Table 2.3 lists the transfer factor for two-port devices.

Table 2.3. Transfer factors for transferring the experimental velocity into the volumetric flowrate

No.	*F*	*G(0)*	*k*
			(m^2)
9A	0.01138	0.000594	2.013E-09
9D	0.01134	0.000592	1.992E-09
7A	0.01129	0.000587	1.943E-09
7D	0.01118	0.000577	1.923E-09

a) *F* was calculated by Equation 2.5;
b) *G(0)* was calculated by Equations 2.2;
c) *k* was calculated by comparing Equations 2.4 and 2.5 to Equation 2.2.

2.4.3 Fluidic Impedance of a Flow Channel Network

We have combined two further tests of the Hagen-Poisseuille equation in the evaluation of a three-port device we utilized previously for the creation of chromatography and solid phase extraction beds. While our two-port devices contained slot shaped channels, many fluidic devices employ a D-shaped channels that results from isotropic etching of a mask feature that to a depth similar to the feature width. Our optical probe approach is not effective with such a channel, as the y-dimension velocity variation

is significant relative to the laser probe spot size we used. However, measurement in a slot channel connected to a D-shaped channel should be effective, just as it is for measurement of flow across the very shallow weir. The tests described below show this is the case. Additionally, fluidic networks are a key component of most microfluidic chips, and passive control of flow distribution within a network is a key element of chip design. We have further tested the Hagen-Poisseuille equation by comparing the predicted flow distribution obtained for a three-port design, incorporating two weirs, a D-shaped channel, and a branched network with experimental measurements of the linear velocity distribution.

Figure 2.7 illustrates the three port devices tested, while Table 2.4 provides the specific dimensions of each region of the device. The side channel was designed to have a high enough resistance to flow compared to the weirs and the main channel to minimize flow into the side when pumping fluid along the main channel. We measured flow rates upstream and downstream of the two weirs, and compared them to determine the loss to the side channel. To compare the results with theory as accurately as possible we also needed to calculate the form factor, F, for the isotropically etched side channel, and this was done using a computational fluid modeling package from Coventor.

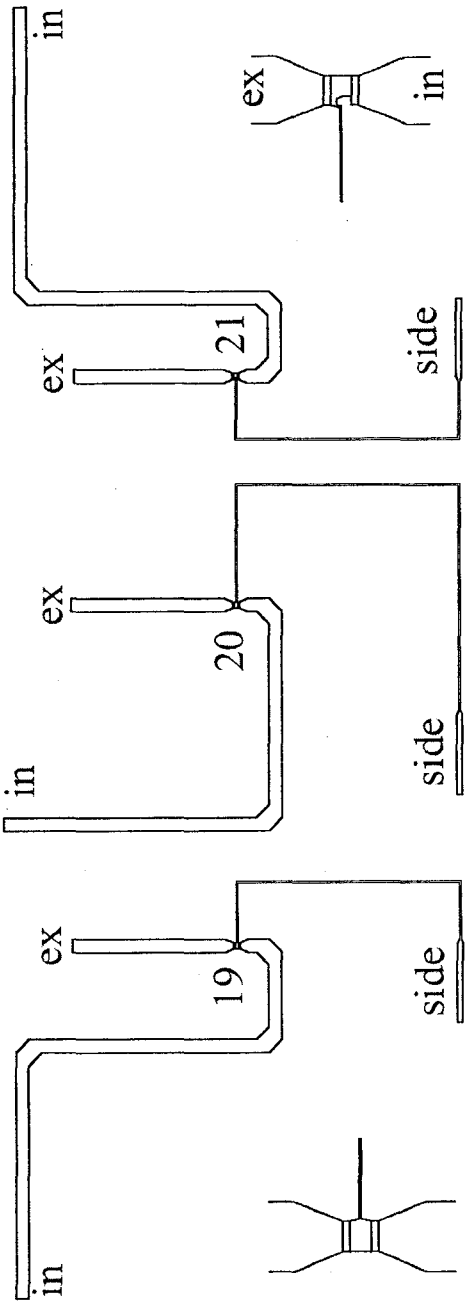

Figure 2.7. Layout of 3-port devices tested in this study. Devices were numbered for identification, as shown. The pressure drops and dimension labels used in the analysis are shown. Most work was done using the symmetric side channel connection to the double weir zone (left inset), while some studies were performed using the asymmetric entrance to the double weir zone (right inset).

Table 2.4. Channel dimensions (in micron) for three-port devices

Device No.	**Width**	**Depth**	**Length**
819			
Exit channel	592	9.625	5997
Weir	273	3.155	21.6
Side channel 1	42.2	10.79	15108
Side channel 2	225	10.79	2165
619			
Exit channel	590	9.605	5976
Weir	277	1.035	17.7
Side channel 1	43.8	10.74	15321
Side channel 2	235	10.74	2077
820			
Exit channel	592	9.705	5294
Weir	276	3.165	31.0
Side channel 1	41.2	10.81	25282
Side channel 2	223	10.81	2059
720			
Exit channel	588	9.640	5343
Weir	274	1.000	32.2
Side channel 1	40.2	10.78	25273
Side channel 2	222	10.78	1695
620			
Exit channel	593	9.650	5346
Weir	279	1.060	27.6
Side channel 1	43.8	10.84	25312
Side channel 2	235	10.84	2194
921			
Exit channel	592	9.730	5351
Weir	275	3.025	29.8
Side channel 1	41.8	10.84	15277
Side channel 2	223	10.84	2481
621			
Exit channel	593	9.680	5337
Weir	278	1.035	26.4
Side channel 1	44.0	10.76	15287
Side channel 2	236	10.76	2055

The Hagen-Poisseuille equation may be expressed as $Q = \Delta p/r$, where r is the fluidic resistance of a flow channel segment, and $r = 4\eta L/(Wd)^2F$. We consider the point at the centre of the main channel midway between the two weirs. The pressure drop between this point and either of the two exit ports Δp. Expressed for the main exit channel:

$$\Delta p = \Delta p_{ex} + \Delta p_{wr} \quad \text{or} \quad \Delta p = Q_{ex}r_{ex} + Q_{ex}r_{wr} \tag{2.12}$$

where subscript ex refers to the 10 μm deep exit channel (including the segment from the centre of the channel to the weir), and wr to the weir region. The volume flow rate towards the exit port is the same in the 10 μm deep portion as it is across the weir. We can rearrange this expression to obtain

$$Q_{ex} = \Delta p/(r_{ex} + r_{wr}) \tag{2.13}$$

The side channel is comprised of a long narrow segment (subscript 1) to restrict flow and a short, wide segment (subscript 2) allowing us to write

$$Q_s = \Delta p/(r_{s1} + r_{s2}) \tag{2.14}$$

The flow into the main channel exit, relative to the total flow from the main channel inlet, is given by

$$Q_{ex}/(Q_{ex} + Q_s) = Q_{ex}/Q_{in} = (r_{s1} + r_{s2})/(r_{ex} + r_{wr} + r_{s1} + r_{s2}) \tag{2.15}$$

where Q_{in} is the inlet channel flow. The value Q_{ex}/Q_{in} was evaluated experimentally by measuring the linear flow rate both upstream and downstream of the two weirs. Because the cross section of the main channel is the same at both measurement locations, the ratio of linear flow rates is equal to the ratio of volume flow rates, Q_{ex}/Q_{in}(exp). Figure 2.8 shows the linear flow velocities measured for weir depths of 1 and 3 μm. Figure 2.9 shows a set of experimental velocities for device 621 with an asymmetric chamber (see right inset, Figure 2.7). Table 2.5 presents the ratio of flow velocities for a series of devices, whose measured geometries are presented in Table 2.4. The data show that decreasing the depth, or increasing the length of the weir resulted in increased flow into the side arm, while increasing the length of the side arm had the opposite effect (e.g. device 620 vs 621).

Table 2.5. Comparison of the experimental, calculated, and nominal flow ratios

Device No	Q_{ex}/Q_{in}%(exp)	Q_{ex}/Q_{in}% (cal)	Q_{ex}/Q_{in}% (nom)	Q_{ex}/Q_{in}%(cal-exp)
819	96.0	96.8	98.3	+0.8
619	86.3	85.6	87.9	-0.7
820	98.5	98.2	99.0	-0.3
720	86.3	86.1	90.1	-0.2
620	86.9	87.6	90.3	+0.7
921	96.5	96.9	98.3	+0.4
621	81.6	80.9	84.9	-0.7

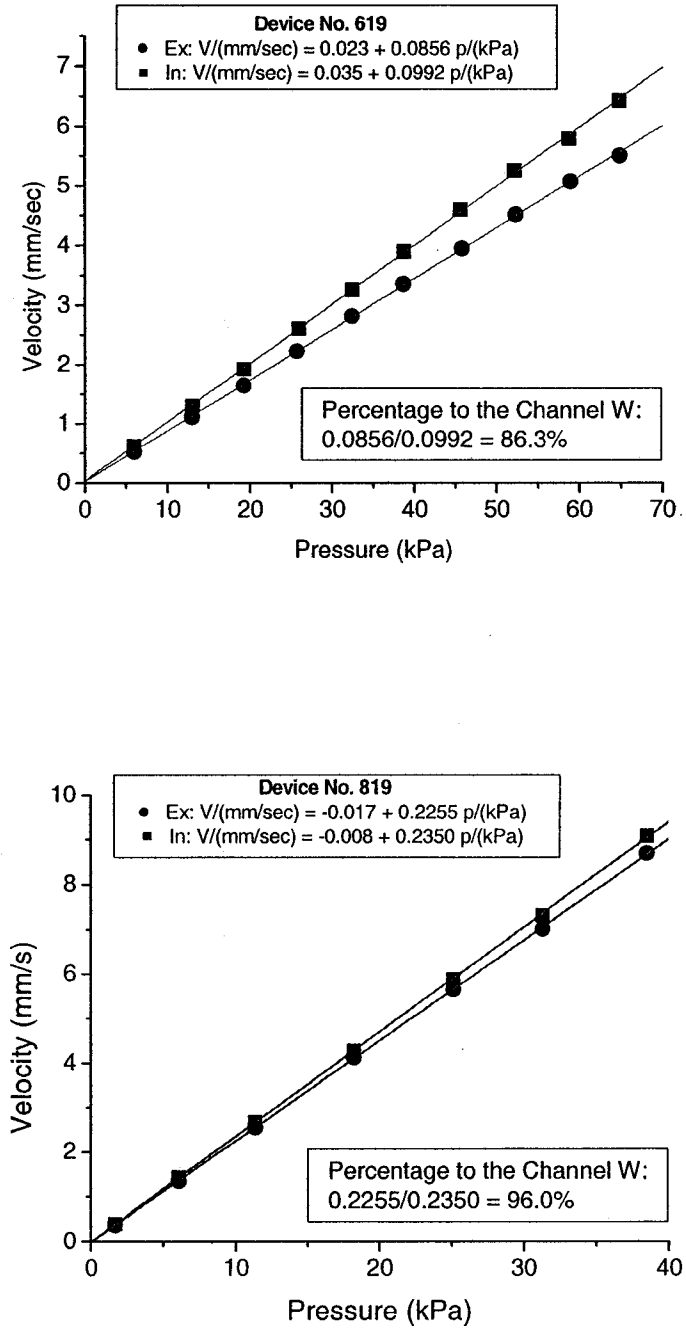

Figure 2.8. Plot of flow velocity versus applied pressure for x19 three-port devices, one with weirs etched 1.04 μm deep and 17.7 μm long (619), the other with weirs etched 3.16 μm deep and 21.6 μm long (819). Upper traces of each pair of curves show the flow velocity upstream of the double weirs in the main channel, while lower traces show the velocity downstream of both weirs in the main channel. Bleaching laser 10-15 mW, detection laser 2.5 mW, PMT bias 500 V.

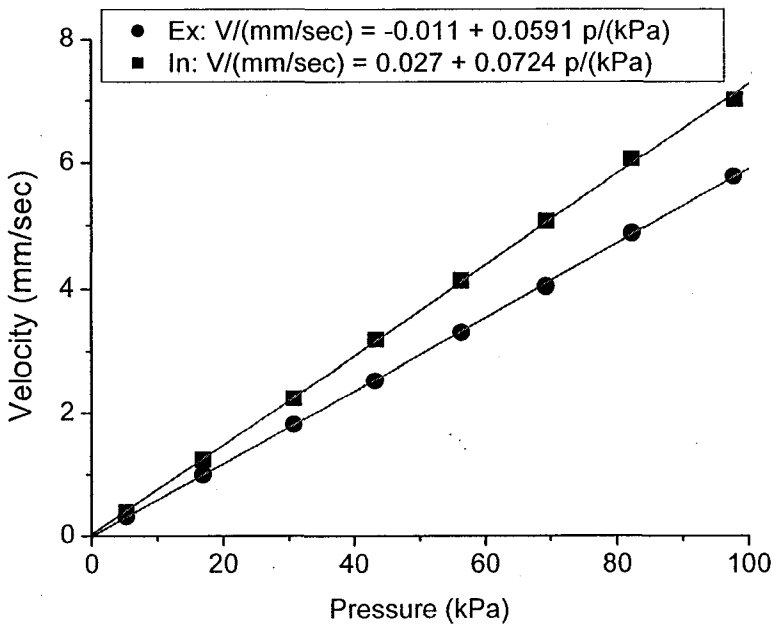

Figure 2.9. Experimental velocities measured in device 621 with an asymmetric chamber.

2.4.4 Form Factor for D-Shaped Channels

In order to calculate r_{s1} and r_{s2} accurately the form factor, F_D, for an isotropically etched, D-shaped channel must be used, rather than the form factor for a rectangular channel given by Equation 2.5. Because the D-shape is ubiquitous experimentally, we concluded that it would be useful to make available a working curve for its Hagen-Poisseuille equation form factor. Details regarding the stability and accuracy of the FEM simulation with Coventor's FlumeCAD are given in section 2.3.5. Figure 2.10 shows a parabolic velocity profile obtained for a D-shape channel. Figure 2.11 shows

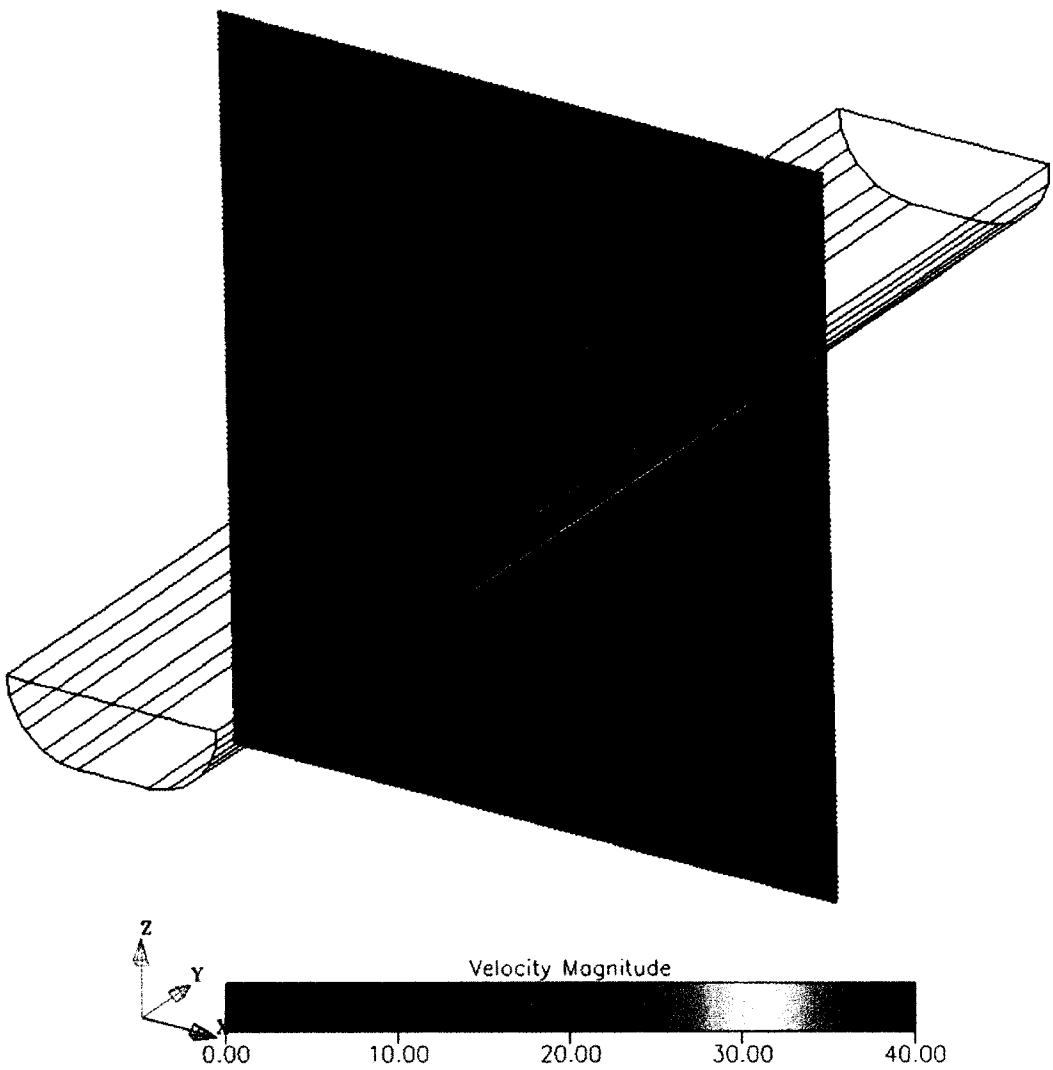

Figure 2.10. Simulated velocity profile in a D-shaped channel by using FlumeCAD software. The segment of the channel shown in this figure is smaller than the real length of the channel for simulation. The scale shows relative units.

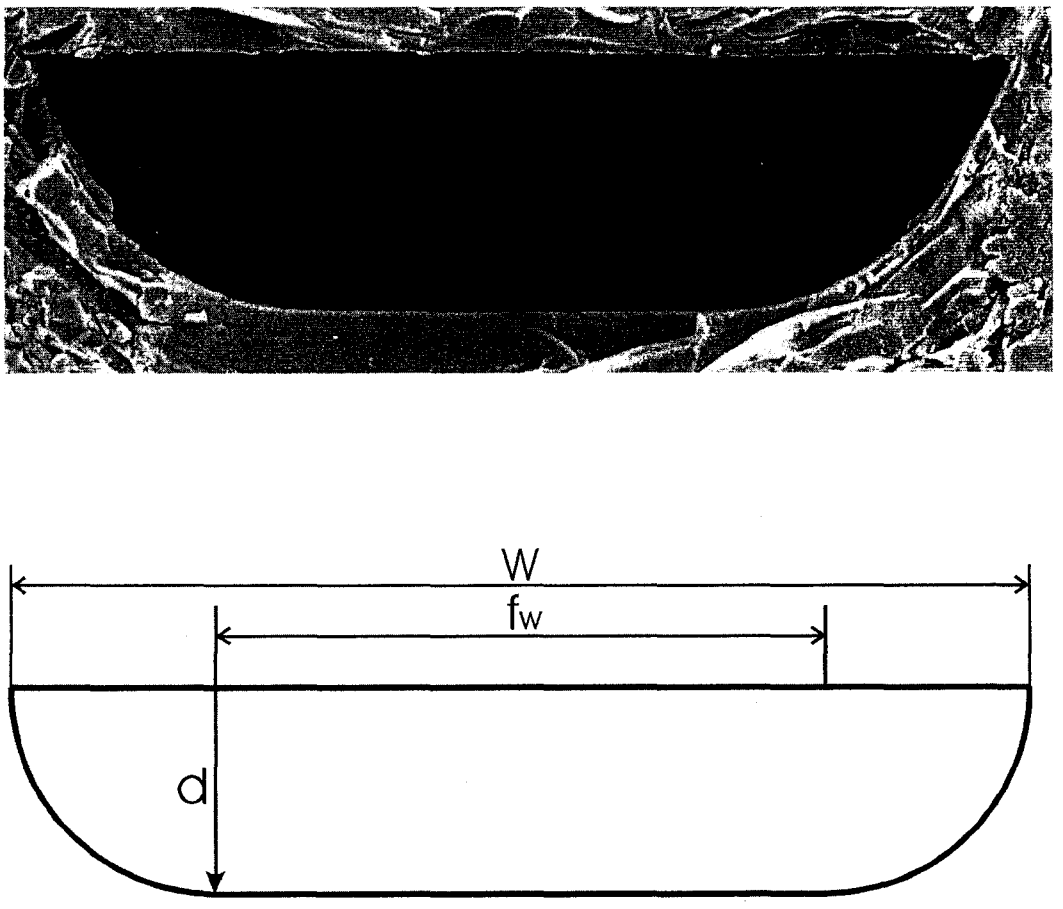

Figure 2.11 Electron micrograph of a typical D-shaped isotropically etched channel. Dimension labels used for cross sectional analysis are indicated.

an electron micrograph of a D-shaped channel, along with the notation used for the dimensions. The D-shape was taken to have width W-2d = fw at the bottom of the channel, W at the top, and a circular arc with radius d sweeping out the side walls, in good agreement with the photomicrograph. The aspect ratio, or d/W, is the critical variable in the form factor calculation, and we have compared channels having the same aspect ratio, as shown in Figure 2.12. The form factor F_D was calculated from $F_D = 4\eta LQ_{sim}/(Wd)^2\Delta p$, where Q_{sim} is the FEM simulated flow velocity. It is evident there are significant differences for d/W ratios greater than ~0.05. However, the differences are exaggerated by the different cross sectional areas of D- versus rectangular shapes, and so we also show the form factor calculated according to $F_D = 4\eta LQ_{sim}/A^2\Delta p$, where A is the area of a D-shaped channel with aspect ratio d/W. In order to facilitate the use of the working curve for a D-shaped channel, the results in Figure 2.12 for the lower trace were fit to the empirical equation below

$$F_D = 0.3468\left(\frac{d}{W}\right) - 0.6230\left(\frac{d}{W}\right)^2 + 1.2466\left(\frac{d}{W}\right)^3 - 2.7916\left(\frac{d}{W}\right)^4 + 2.3696\left(\frac{d}{W}\right)^5 \quad (2.16)$$

The equation showed that the rsd is smaller than ±0.5% ($r^2 = 0.9998$) for aspect ratios between 0.05 to 0.5.

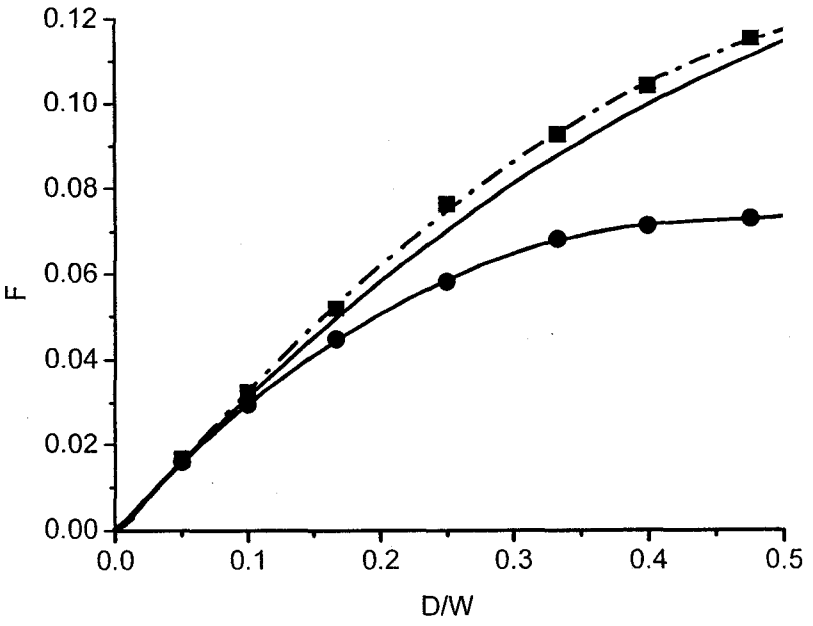

Figure 2.12 Plot of geometrical form factor, F, as a function of aspect ratio, depth/width (d/W), for a rectangular cross section and for a D-shaped channel. F was calculated using Equation 2.5 for the rectangular shape. F for the D shaped channel was calculated using $F_D = Q_{sim}4\eta L/(Wd)^2\Delta p$ for the lowest trace, and $F_D = Q_{sim}4\eta L/A^2\Delta p$ (A is area) for the uppermost trace. The lowest curve was fit with Equation 2.16 to provide a working curve for F_D.

2.4.5 Applicability of the Hagen-Poisseuille Equation in Modeling a Fluidic Network

The fluid flow within the 3-port device could be evaluated using the Hagen-Poisseuille equation, along with the form factors given by Equation 2.16 for a D-shaped channel and Equation 2.5 for the slot-shaped channels. Again, taking the pressure drop from the centre of the main channel midway between the two weirs to

atmosphere as Δp, we use Equation 2.13-2.15 to calculate the ratio predicted for Q_{ex}/Q_{in}(cal). The resulting values are given in Table 2.5, along with the deviation relative to the experimentally observed ratio, Q_{ex}/Q_{in}(exp). The deviation in Table 2.5 is smaller than that seen in Table 2.2, presumably because the error of a relative flow rate is less susceptible to measurement bias than is the absolute flow rate. The comparison shows that the Hagen-Poisseuille equation accurately predicts the ratio of flows at the branching point in the channel, even with a 1-μm sized flow channel as one of the design components.

The value for Q_{ex}/Q_{in}(cal) was determined using measured values of the device dimensions, rather than the nominal values targeted by the fabrication process. Since variations in etch depths and channel lengths do occur from batch to batch, and even within a single wafer, it is instructive to evaluate how great an effect this can have on the deviation between experiment and theory. The value for Q_{ex}/Q_{in}(nominal) was calculated assuming etch depths of 10 μm for the deep channel, 1 or 3 μm for the weirs, and a 1:1 aspect ratio for isotropic etching, using the feature widths of the mask design. The side channel form factor was evaluated for a D-shape, and the other channels were taken to be rectangular. A comparison in Table 2.5 of Q_{ex}/Q_{in}(nominal) with Q_{ex}/Q_{in}(cal) predicted for actual dimensions shows a deviation of 1-4 %, as does a comparison to the measured flow rates, Q_{ex}/Q_{in}(exp). This result provides a useful estimation of the tolerance that can

be expected in performance from fabricated flow restrictors, relative to the design parameters.

2.6 Conclusions

Photobleaching time of flight provides measurement of the linear velocity of flow rates in microchannels and offers a useful alternative to PIV techniques, which are not well suited to micron and submicron sized channels. Maximum linear velocity was successfully converted to volumetric flow rates so that the measured values could be compared quantitatively to the predictions of the Hagen-Poisseuille equation. The Navier-Stokes equation and the Hagen-Poisseuille solution to that equation successfully describe the pressure - flow rate relationship in devices with at least one dimension on the scale of 1 μm. This contrasts with claims of a variety of previous studies (4-8), but is consistent with most researchers expectations. The model was tested across a linear flow rate range in the narrowest dimension of 0.3-16 mm/sec and a volumetric flow rate range of 0.6-32 nL/sec. The maximum Reynolds number tested was 0.3. The Hagen-Poisseuille solution can be used to design multiport devices with intersecting channels, achieving the intended flow rate ratios in channels with differing flow resistance with an accuracy of 1-2%. Despite the differences between achieved etch depths and widths and the nominal values a deviation of only 1-4 % in the flow ratios was observed. This observation

provides a useful guideline for predicting tolerance sensitivity in device manufacture. The empirical equation of the geometric form factor for a D-shaped channel can be used for the future design.

2.7 References

1. Harrison, D. J.; Fluri, K.; Seiler, K.; Fan, Z.; Effenhauser, C. S.; Manz, A. *Science* **1993**, 261, 895-898.
2. Longwell, P. A. *Mechanics of fluid flow*, McGraw-Hill: New York, **1966**.
3. Johnson, R.W. *The Handbook of Fluid Dynamics*, CRC Press: Boca Raton, **1998**.
4. Pfahler, J.; Harley, J.; Bau, H.; Zemel, J. *Sens. Actuators* **1990**, A21-23, 431-434.
5. Peng, X. F.; Peterson, G. P.; Wang, B. X. *Exp. Heat Transf.* **1994**, 7, 249-264.
6. Mala, G. M.; Li, D. *Int. J. Heat Fluid Flow* **1999**, 20, 142-148.
7. Papautsky, I.; Brazzle, J.; Ameel, T.; Frazier, A. B. *Sens. Actuators A* **1999**, 73, 101-108.
8. Sharp, K. V.; Adrian, R. J.; Beebe, D. J. In *2000 ASME International Mechanical Engineering Congress & Exposition*, Orlando, FL, MEMS-Vol. 2, **2000**, pp. 461-466.
9. Chen, Z.; Milner, T. E.; Dave, D.; Nelson, J. S. *Opt. Lett.* **1997**, 22, 64-66.

10. Santiago, J. G.; Wereley, S.; Meinhart, C. D.; Beebe, D. J.; Adrain, R. J. *Exp. Fluids* **1998**, 25, 316-319.

11. Drain, L. E. *The Laser Doppler Technique*, John Wiley & Sons: Chichester, **1980**.

12. Wang, W.; Lui, Y.; Sonek, G. J.; Berns, M. W.; Keller, R. A. *Appl. Phys. Lett.* **1995**, 67, 1057-1059.

13. Monnig, C. A.; Jorgenson, J. W. *Anal. Chem.* **1991**, 63, 802-807.

14. Monnig, C. A.; Dohmeier, D. M.; Jorgenson, J. W. *Anal. Chem.* **1991**, 63, 807-810.

15. Moore, A. W., Jr.; Jorgenson, J. W. *Anal. Chem.* **1993**, 65, 3550- 3560.

16. Oleschuk, R. D.; Shultz-Lockyear, L. L.; Ning, Y.; Harrison, D. J. *Anal. Chem.* **2000**, 72, 585-590.

17. Oleschuk, R. D.; Jemere, A. B.; Shultz-Lockyear, L. L.; Fajuyigbe, F.; Harrison, D. J. In *Proceedings of Micro Total Analysis Systems 2000*, Kluwer Academic Publishers: Dodrecht, The Netherlands, 2000; pp 11-14.

18. Fan, Z. H.; Harrison, D. J. *Anal. Chem.* **1994**, 66, 177-184.

19. Baker, A. J. *Finite Element Computational Fluid Mechanics*, Hemisphere Publishing Corporation: Washington, **1983**.

20. Neckers, D. C.; Valdes-Aguilera, O. M. *Adv. Photochem.* **1993**, 18, 315-394.

21. Lindquist, L. *Arkiv. Kemi.* **1960**, 16, 79-138.

22. Kasche, V.; Lindquist; L. *J. Phys. Chem.* **1964**, 68, 817-823.

23. Ocvirk, G.; Tang, T.; Harrison, D. J. *Analyst* **1998**, 123, 1429-1434.

24. *FlumeCAD Guide*, Coventor Technologies, Inc.: Raleigh, **2000**.

25. Probstein, R. F. *Physicochemical Hydrodynamics: An Introduction*, 2nd ed., Wiley & Sons: New York, **1994**.

26. Lide, D. R. (Ed.) *Handbook of Chemistry and Physics*, 83rd ed., CRC Press: Boca Raton, **2002-2003**.

27. Wu, S.; Dovichi, N. J. *J. Appl. Phys.* **1990**, 67, 1170-1182.

Chapter 3

Design and Fabrication of Magnetohydrodynamic Liquid Chromatography Chips

3.1 Introduction

The most popular pressure driven analytical instrument is liquid chromatograph (LC), but a fully chip-based LC has not been realized. This is because pressure driven flow requires pumps and valves; manipulating a pressure driven flow on chip is very demanding. The reason that capillary electrophoresis (CE) and capillary electrochromatography (CEC) are successful on-chip is because electroosmotic flow (EOF) can be realized and controlled by the application of voltages, without any active pumps or valving. There is one other technique that can be effectively used to manipulate fluids in a microchannel, namely magnetohydrodynamic (MHD) flow. This technique has not yet been thoroughly explored for LC. Therefore, this thesis investigates the development of an LC chip using MHD flow.

3.1.1 Magnetohydrodynamic (MHD) Flow

As discussed in section 1.3, the interaction between an electric current and a perpendicular magnetic field generates a Lorentz force. If we apply a current across a

conductive electrolyte solution, as shown in Figure 3.1, then the current carrying ions experience the Lorentz force and move, dragging the nearby solution forward, and hence

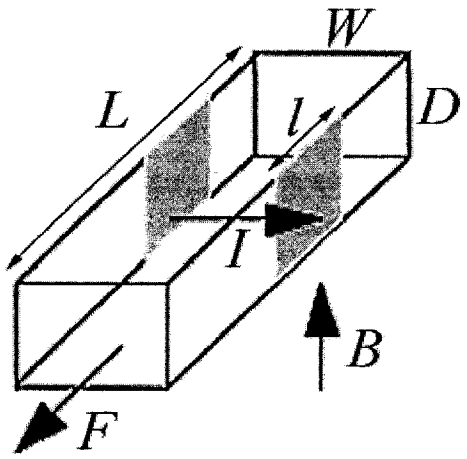

Figure 3.1. Lorentz force generated by the interaction between a current across a channel filled with an electrolyte solution and a perpendicular magnetic field.

creating a bulk flow. This flow is known as magnetohydrodynamic (MHD) flow. The pumping pressure p generated by MHD flow can be calculated from

$$p = IB / D \tag{3.1}$$

where I is the electric current across a channel, B the flux density of the magnetic field, and D the height of the electrodes. Clearly, without the magnetic field, no pumping will occur. Under a given magnetic field, p is proportional to I. Reversing the current direction will reverse the flow direction. Similarly, reversing the direction of B will also reverse the flow direction.

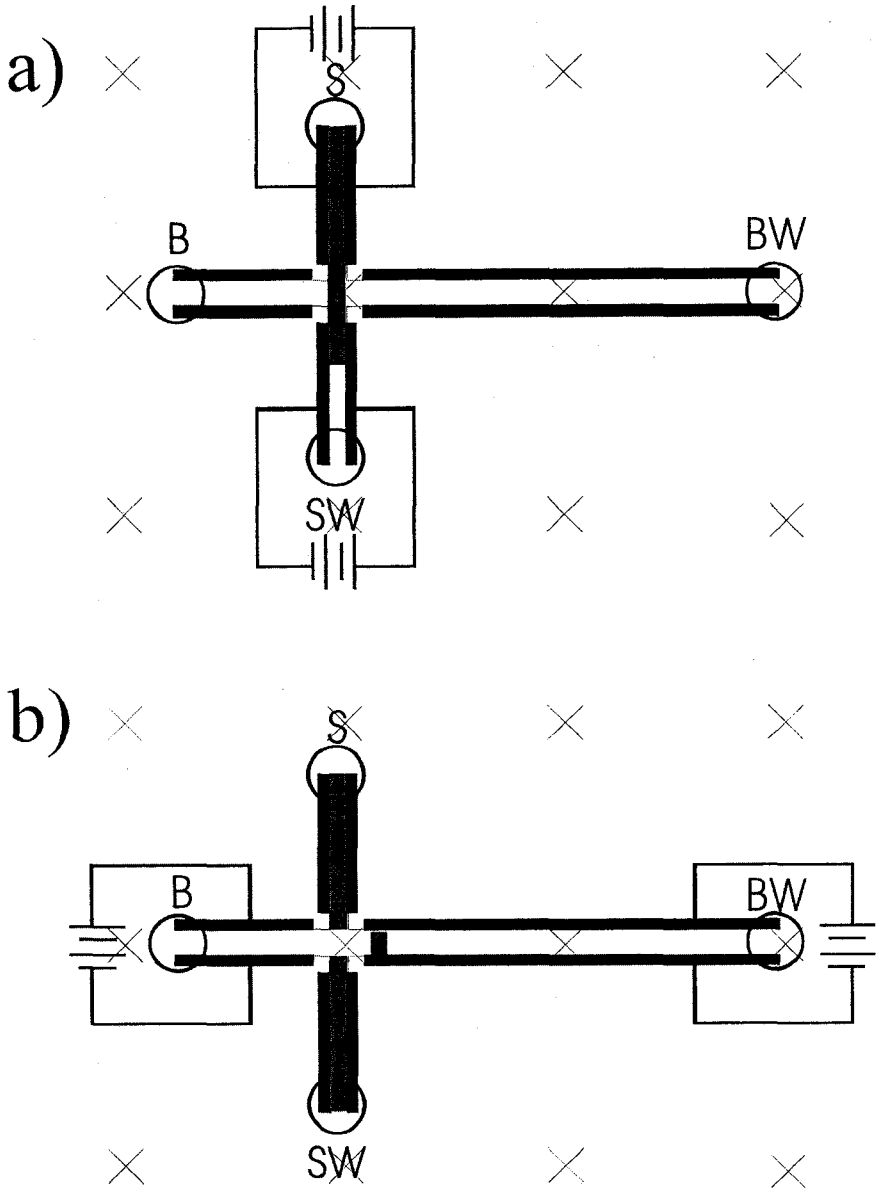

Figure 3.2. a) Injection: Apply voltage to the sampling channels and pump the sample from the reservoir S to SW. b) Separation: Pump the sample plug towards BW. Open tubular separation occurs with stationary phase immobilized on walls.

MHD could potentially be used to pump an LC on chip. Under a magnetic field, if we apply a voltage across channels which are filled with electrolyte solution, MHD can pump a sample, say from reservoir S to SW (Figure 3.2a). If we then switch the voltage, as shown in Figure 3.2b, a sample plug will be created, and pumped towards reservoir BW. Valveless switching of fluid flow between channels is achieved by switching the voltages applied to each channel, just as when using CE chips (1). Any leakage arising from convective flow or diffusion at intersecting channels can easily be eliminated by adding some pumping in the side channels in the required directions (Figure 3.3), as is done with *pinching* or *pushback* techniques used in CE chips (1-3). Immobilizing a stationary phase on the column walls then allows open tubular liquid chromatography (OTLC). We will refer to such a liquid chromatograph on a chip, with magnetohydrodynamic pumping, as an *MHD liquid chromatograph (MHD LC)*, or as *electromagnetic liquid chromatograph (EMLC)*.

3.1.2 MHD Pumping for LC Applications

When we apply a potential to create a current flow through a liquid for MHD LC, the current through the channel is limited by the bubble current density threshold $j_b = I/lD$, at which electrolysis occurs, so we can also write that the maximum pressure attainable, p_m, is

$$p_m = j_b lB \tag{3.2}$$

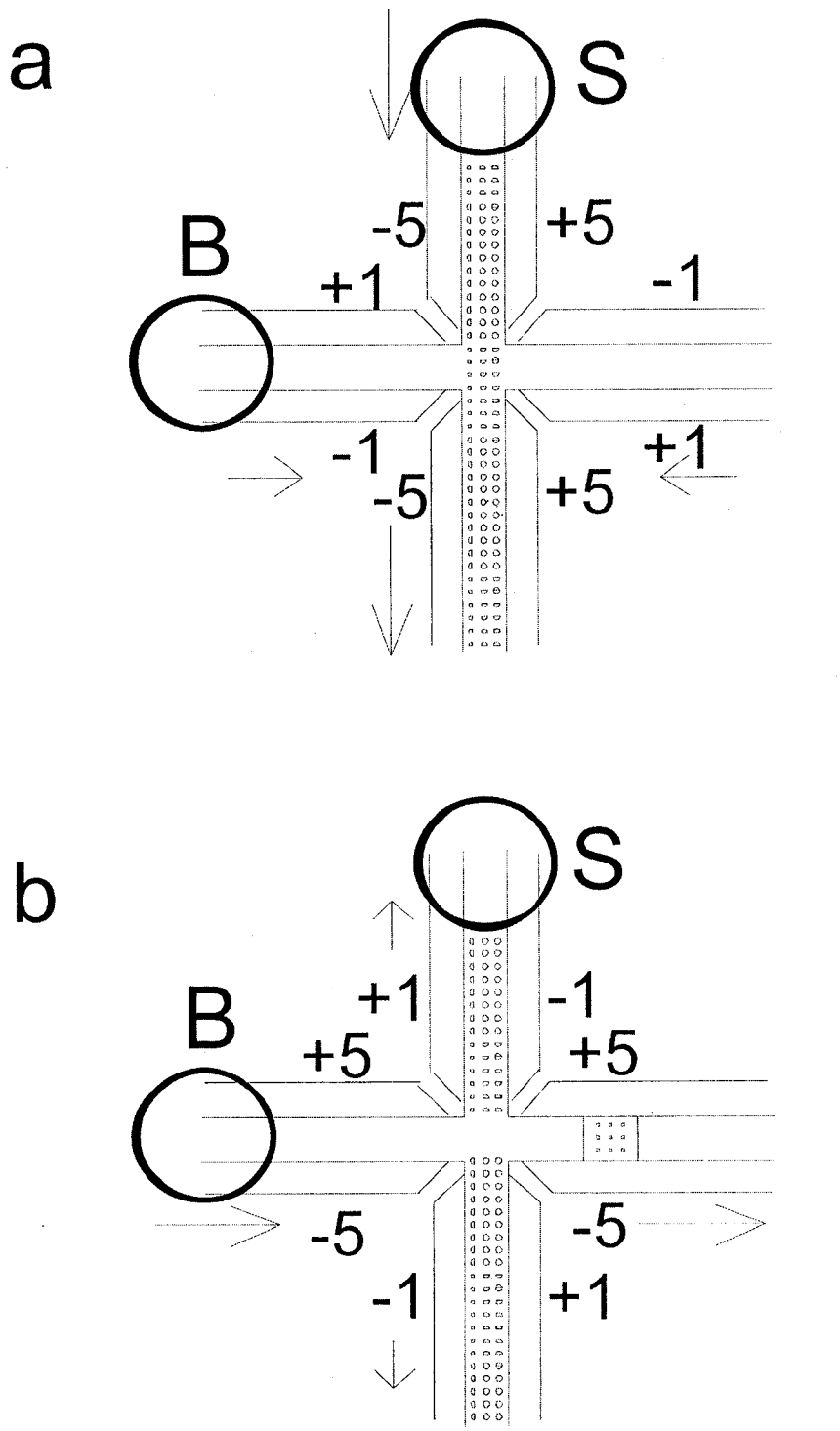

Figure 3.3. a) Pinching; b) Pushback. The numbers represent the relative voltage applied to the microchannels. The arrows represent the flow directions.

where l is the length of the electrodes. For a rectangular channel as in Figure 3.1, maximum pressure can be converted into a maximum linear velocity, v_m:

$$v_m = \frac{WDlFj_b B}{4\eta L} \tag{3.3}$$

where F is the geometric factor as defined in section 2.2, η the viscosity of the fluid, and L the length of the channel. The value of v_m depends on magnetic field strength, electrode length and maximum bubble current density. The value of j_b increases as the AC frequency increases, but as discussed in Chapter 1, the AC field strength of an electromagnet decreases with frequency. Frequency is thus not the easiest parameter to modify to improve performance. We can also see that for a given current density, the pumping speed is directly proportional to the cross-sectional area of the channel. In other words, the smaller the channel size, the lower the pumping speed. This means that the MHD pump scales in the wrong direction for microfluidics – a big misfortune. Lemoff and Lee obtained a speed of 1.5 mm/sec, but used a big trapezoidal channel (380 μm deep, top 800 μm wide, with a 54° trapezoidal angle down to the bottom) (4, 5). Eijkel *et al.* decreased the cross-section to 30 μm deep × 200 μm wide channels, but the velocity dropped to 40 μm/sec (6, 7). Unfortunately, for OTLC, the Golay equation tells us a minimum velocity of 100 μm/sec in a 10 μm channel is required, as discussed in Chapter 1. Therefore, unless we are able to increase the pumping pressure or velocity, the MHD pump is too weak for OTLC. The Golay equation (equation 1.1) suggests several

compromises and design changes that can be made to adopt MHD for LC application. These are discussed below.

3.1.2 Ideas to Enhance MHD Pumping on Chip

In order to enhance MHD pumping on-chip, three ideas have been proposed and explained in this thesis: a) improve and optimize the earlier microchannel designs (this chapter); b) build a strong AC magnetic field source at a higher frequency (Chapter 4); c) find a highly conductive liquid to allow use of low DC voltage without electrolysis (Chapter 5). In this chapter, I will focus on how to improve the earlier microchannel design, design LC chips accordingly and then fabricate them. Fabrication of the optimal design proved to be a significant challenge, as will be discussed.

3.2 Electromagnetic Channel (EMC)

The combination of the following design elements has not been used previously within an MHD chip, but could result in higher pumping speeds.

3.2.1 Full Length Electrodes

First, a straightforward but useful idea to enhance the pumping power is to extend the electrodes the full length of the channel, in which case $l = L$ or

$$v_m = \frac{WDFj_bB}{4\eta} \tag{3.4}$$

Therefore, the dependence of the pumping velocity on the channel length, observed for a traditional pressure pump, is not an issue. This could be useful for LC because a longer column is often required for LC, and with this design concept no price is paid in terms of an increased pressure head.

3.2.2 Rectangular Cross-Section

A trapezoidal channel cross-section (Figure 1.3) is easy to make using wet anisotropic Si etching (4, 5), but depositing metal on the walls gives non-parallel electrodes. The non-uniform current density, j, this causes in the channels negatively impacts the flow velocity that can be attained. Considering the higher flow resistance for a trapezoidal cross-section, obtained using an empirical equation (8), we can calculate the mean flow velocity relative to that of a square channel with the same area and depth as

$$\frac{v_{trap}}{v_{squ}} = \frac{2(1-\cot\theta)}{\cot\theta}\left(\frac{\sin\theta}{1+\sin\theta}\right)^2 \ln\frac{1+\cot\theta}{1-\cot\theta}, \qquad \theta < \frac{\pi}{2} \tag{3.5}$$

where θ is the trapezoidal angle. Table 3.1 shows the results, with all velocities being expressed relative to the square geometry. Thus for MHD flow, the best design is square, with metal sidewalls. We refer to a pumping channel mode with a square (or rectangular with close width and depth) cross section and with electrodes that run the full length of the channels as an *electromagnetic channel (EMC)*.

Table 3.1. Comparison on the flow velocity of the trapezoidal and square cross-sections with the same cross-sectional area and depth, square channel as reference.

Cross-section	θ	Relative mean velocity
trapezoidal	54.7	29.4
trapezoidal	60	41.5
square	90	100

Table 3.2. The dimensional parameters for the wire.

Current I (A)	1
Voltage drop U (V)	0.1
Resistance allowed R (Ω)	0.1
Wire length l (m)	0.1
Resistivity ρ (Ωm)	10^{-8}
Area required A (m^2)	10^{-8}
Wire depth D (μm)	20
Wire width W (μm)	500

3.2.3 Cross-Section of the Wires and Electrodes

The current required for MHD pumping is high. Depending upon the length of the channel, it is in the range of 100 mA to 1 A. Simultaneously, the voltage drop along the electrodes due to Ohmic losses needs to be low, say 0.1 V, in order to obtain uniform

pumping force along the channel. This requires thick electrodes or wires to minimize their impedance. Before designing any EMC devices, simple calculations were done, as shown in Table 3.2. For a typical length of wire made of a typical metal, the minimum cross-section required is 10^4 μm^2. In order to reduce the difficulties faced in electroplating thick deposits, we chose a depth of 20 μm. Consequently, the width of the wires needs to be as high as 500 μm.

3.2.4 Bonding Nails

The anisotropic etching process required to fabricate vertical sidewalls makes Si the most obvious material choice, since such processes are readily available for Si (9). The need for an optical detection scheme meant that glass was the best choice for a cover plate. Unfortunately, while Si and Pyrex glass bond well, Pyrex and metal do not. Thus, wide electrodes cause difficulty in bonding at the channel edges. To ensure bonding near the flow channel, an arrangement of Si *bonding nails* embedded within the metal deposit was designed. This is shown in Figure 3.4. Bonding nails are 20 μm away from the flow channel and 40 μm apart, with a size of 160 μm × 100 μm. This design keeps the resistance from the bulk of the electrode to the electrode near the surface of the channel to less than 0.01 Ω.

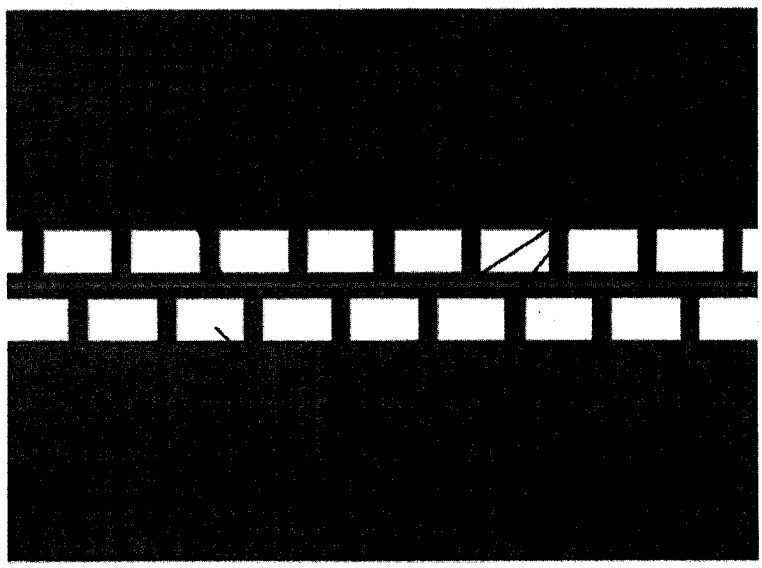

Figure 3.4. EMC with a bonding nail design, realizing better bonding close to the channel. Channel: 10 μm, bonding nail: 160 μm × 100 μm, electrode: 20 μm, wire: 500 μm.

3.2.5 Channel Junctions

Flexible control of flow within each channel can be obtained using independent contact electrode pairs within each channel segment. Therefore, the electrodes at the channel junctions, such as a T junction (Figure 3.5a) and cross junction (Figure 3.5b), must be separated by nonconductive materials. To ensure this, electrodes were separated by at least 5 times the width of the channels. A separation between electrodes in different channel segments of 75 μm was used for the 10 μm wide channels, so as to prevent electrical leakage and cross-talk.

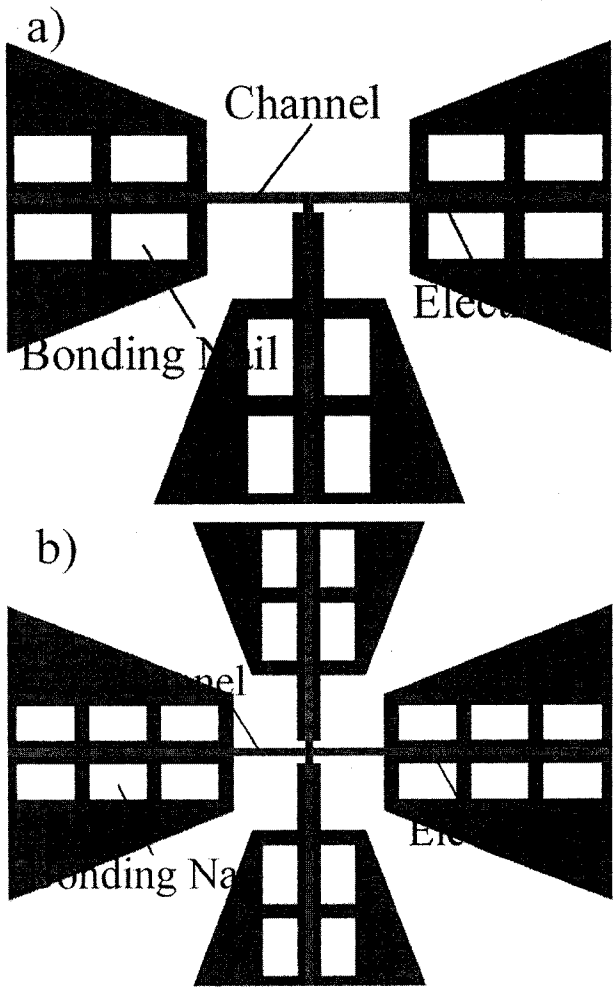

Figure 3.5. a) T junction and b) cross junction design, in which the electrodes (grey) in different channel segments are separated from electrodes in other segments by about 5 times the channel width.

3.2.6 Reservoir Structure

If the electrodes are extended to reservoirs, as in Figure 3.6a, then the current going through a reservoir will be significantly high. This is because the reservoirs are much deeper than the channels (Figure 3.6b) or in other words the resistances are much

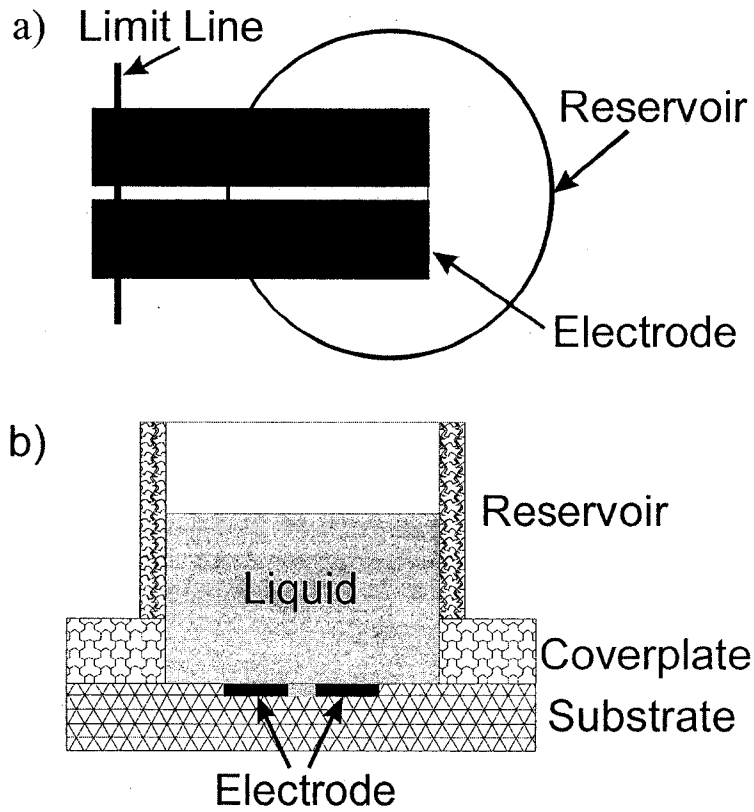

Figure 3.6. Short circuit effect (actually a low impedance shunt) occurs if the electrodes are extended into the reservoir as in a), this is because the reservoir is much deeper than the channel, as in b). The limit line in a) indicates electrode length limit for safe operation.

lower. While not exactly accurate, we refer to the shunt this would create as a *short circuit effect*. In order to avoid any short circuit effect in the reservoirs, the electrodes were designed to end more than 10 times the channel width away from the reservoirs.

3.3 EMLC

This optimized EMC design potentially generates the highest MHD pumping velocity of any device design to-date, per unit cross-section. The next question was how to use an EMC to design LC devices on chip. Several different design concepts were developed, each of which may have certain advantages. Figure 3.7 illustrates the realized designs.

3.3.1 Device E: Easiest LC Design

Figure 3.8 shows a design which is comprised of a sampling channel (from the reservoir S to SW), cross injector, and separation channel (from the reservoir B to BW). This is the easiest (more accurately the simplest) design for LC. The separation channel actually is a straight channel because the detection point is at D. The segment from D to BW was designated the *tail channel*, because it was designed to move BW away from the detection point D. Such a design was required to achieve *prism-coupled LIF detection*, which will be discussed in section 4.3.2. Due to the nature of the EMC, the tail channel will not affect the pumping velocity or the band broadening of the analytes. It will increase the total current flow, however. A shallow, straight separation channel can minimize band-broadening effects due to channel geometry, generate a high surface-to-cross sectional area for immobilizing stationary phase, and hence produce a reasonable separation effect for LC analysis.

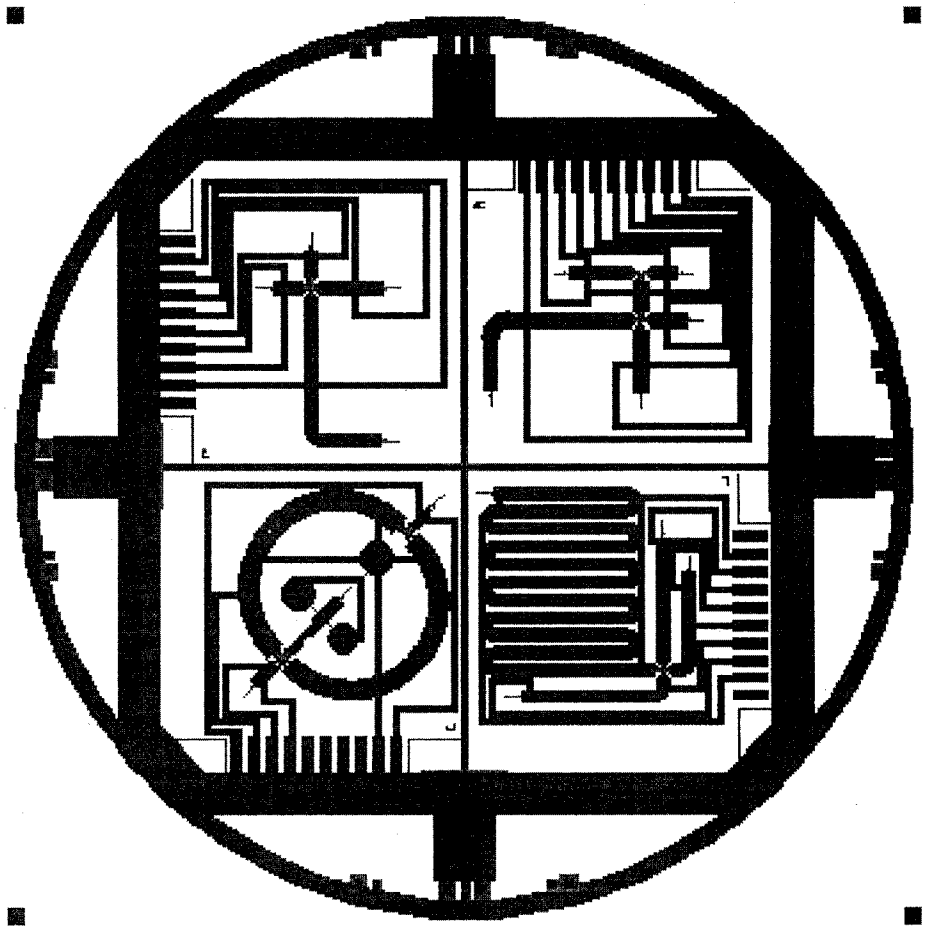

Figure 3.7. EMLC chip design, in which there are 4 different LC devices and a thick wire loop. Top left: device E, top right: device M, bottom right: device L; bottom left: device C.

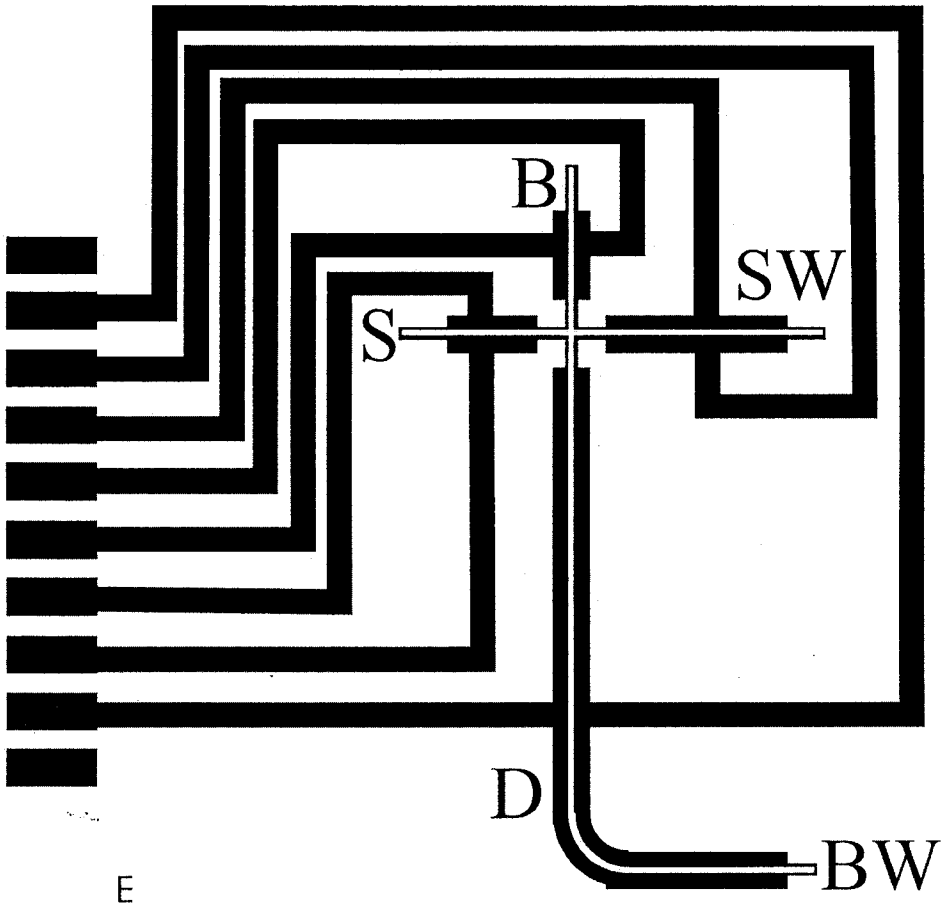

Figure 3.8. The Device E, which includes a straight separation channel. The segment from D to BW is referred to as the *tail channel*. S is sample, SW sample waste, B buffer, BW buffer waste, D detection location. The bonding nails are not shown.

In conventional LC, the plate height from the resistance to mass transfer in the mobile phase, H_M, is the largest term, while both the plate height from the longitudinal diffusion, H_{LD}, and the plate height from the resistance to mass transfer in the stationary phase, H_S, can be omitted in a well designed system. However, in MHD LC, the H_{LD} term may be larger than the H_M term, because the flow velocity in MHD LC is slow. For device E, the channel size is 10 μm. Suppose that the analyte diffusion coefficient is 3.3×10^{-9} m^2 s^{-1} (fluorescein in water, ref. 10), the capacity factor is 1, and the pumping velocity is 100 μm/sec, then H_{LD} = 6.6 μm, and H_M = 1.5 μm. In other words, for a 2 cm long straight separation channel in device E, about 2400 plates can be obtained. As we know, Equation 1.1 was derived for circular channels, not for square channels. For square channels, the H_M term should be larger (say one time larger). However, while H_M does have a dependence on the cross section shape, the term is relatively small compared to H_{LD}, so the above estimation is very close. Compared to conventional OTLC, the unit plate number of MHD LC is a bit less. For example, Gohlin *et al.* (11) obtained 1.9 million plates on a 6 m × ϕ 6.3 μm column (*i.e.* 6600 plates on a 2 cm column).

3.3.2 Device M: Merging Solvents for Solvent Programming

Solvent programming is quite useful for a traditional LC system. By increasing the strength of the eluant, analysis time can be reduced and much better chromatographic peaks can be obtained. Figure 3.9 depicts a design that could generate solvent programs.

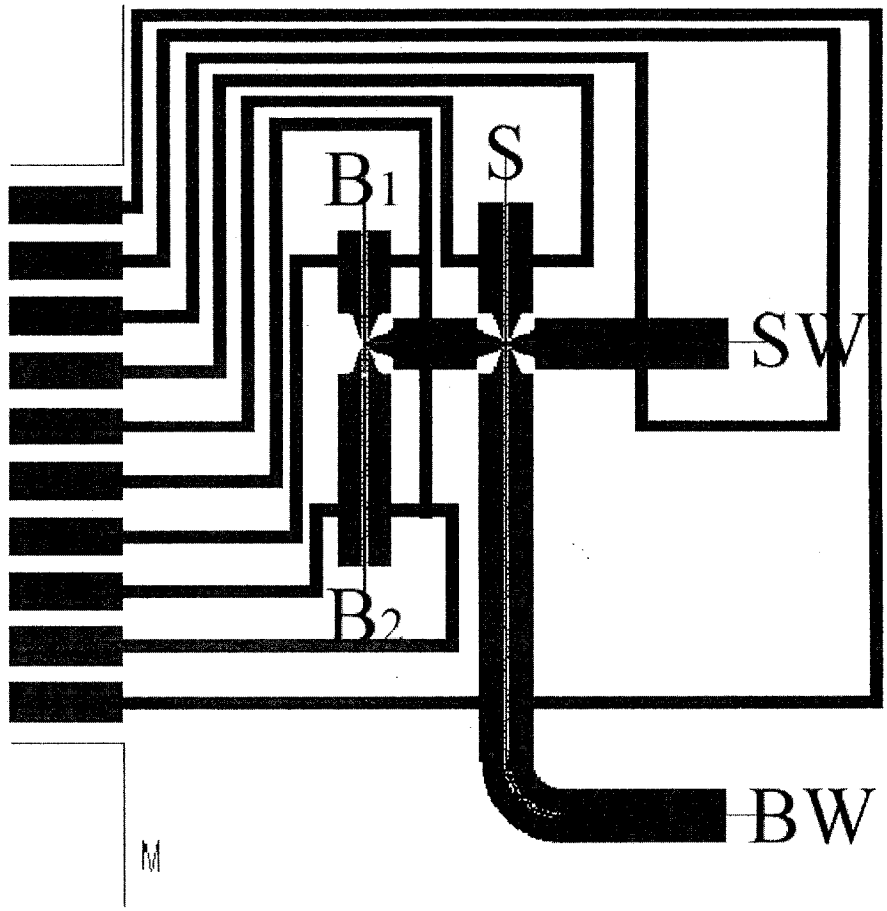

Figure 3.9. The Device M, in which a solvent program can be realized by sweeping the voltages applied to the channels to B_1 and B_2. S is sample, SW sample waste, B_1 and B_2 buffers, BW buffer waste.

By using the EMC, solvent programming should be easily realized by ramping up the voltage applied to the one set of channels while ramping down the voltage on the other set. A solvent program could be generated with such a ramp program by merging flow from B_1 (weak solvent) with flow from B_2 (strong solvent).

3.3.3 Device L: Long Separation Channel in a Small Wafer

Unlike CE, LC often needs a longer channel due to its larger plate heights. In order to obtain a long channel within a given size of wafer (actually a given size (area) of the magnetic field), two different devices were designed. Device L (Figure 3.10) would be a very useful LC design. In a 34 mm × 34 mm wafer, a 20 cm long separation channel was formed, which could potentially realize large numbers of plates (say 20,000). Another advantage is that the detector can be set at any point along the channel, if we want to shorten the separation time.

In terms of band broadening, spiral channels were proven to be better than the serpentine shape for CE. However, for the EMC design, since the electrodes/wires are very thick, it is difficult to use a spiral shape in a small region of a wafer.

3.3.4 Device C: Circular Separation Channel

It is possible to make an infinitely long channel for LC by MHD. Figure 3.11 shows a device with a circular separation channel, a concept which was first reported by

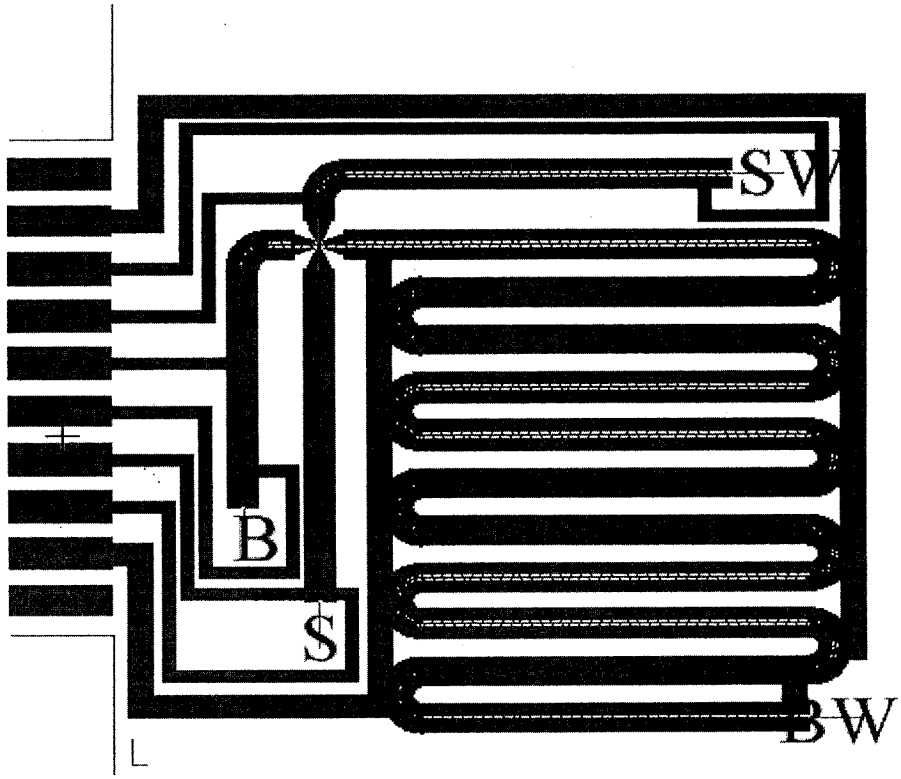

Figure 3.10. The device L, in which a 20 cm long separation channel is included. S is sample, SW sample waste, B buffer, BW buffer waste.

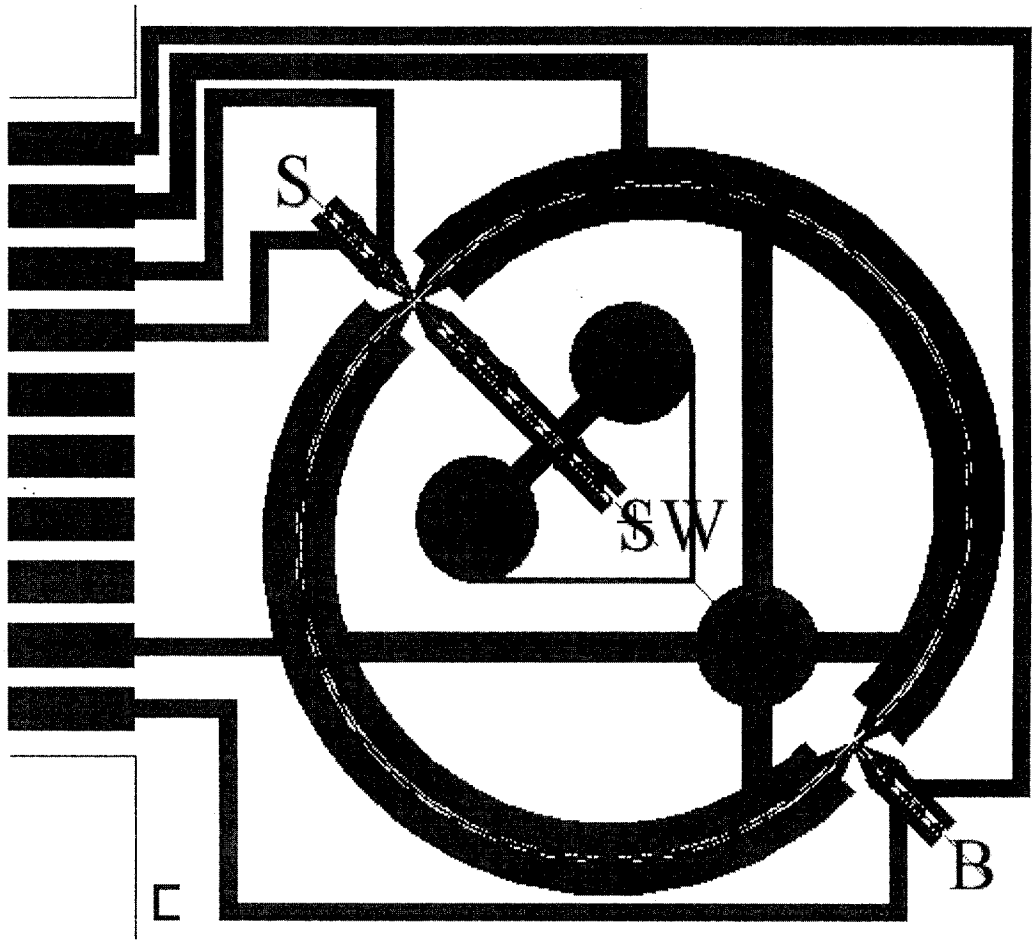

Figure 3.11. The Device C, which has a circular separation channel. The detection can be done anywhere in the loop. S is sample, SW sample waste, B buffer.

Eijkel *et al.* (6, 7). MHD flow can make the fluid flow in a circle, creating an infinitely long separation loop. A detector can be set at any point of the loop and the detection can be performed each time the analytes circle the loop. Of course, the sample may ultimately disperse too much, or exceed the peak capacity of the loop (12). Thus, the separation efficiency possible is not infinite.

3.4 Microelectromechanical Systems

The EMC design presents a significant challenge for current microfabrication methods, although the issues are not obvious at first glance. The EMC design requires that a top plate be bonded, creating capillaries by capping the channels formed in the bottom plate, as shown in Figure 3.12. Bonding processes available place severe constraints on the planarity of the bottom plate. Thick metal deposits have usually been made by electrochemical deposition. While this method is common in micromachining, there is no significant experience with placing a hermetically sealed top plate over such large electroplated structures. In fact, the roughness of most electroplated surfaces means this cannot be accomplished without additional processing (13). We have developed a polishing procedure to address this issue.

The required feature size of 10 μm made SU-8 unacceptable as a deep resist, as 15 μm is a typical lower feature size (14), meaning bulk machining with ICP-RIE was preferred to obtain vertical sidewalls. A two-mask (masks were prepared by DWL 66

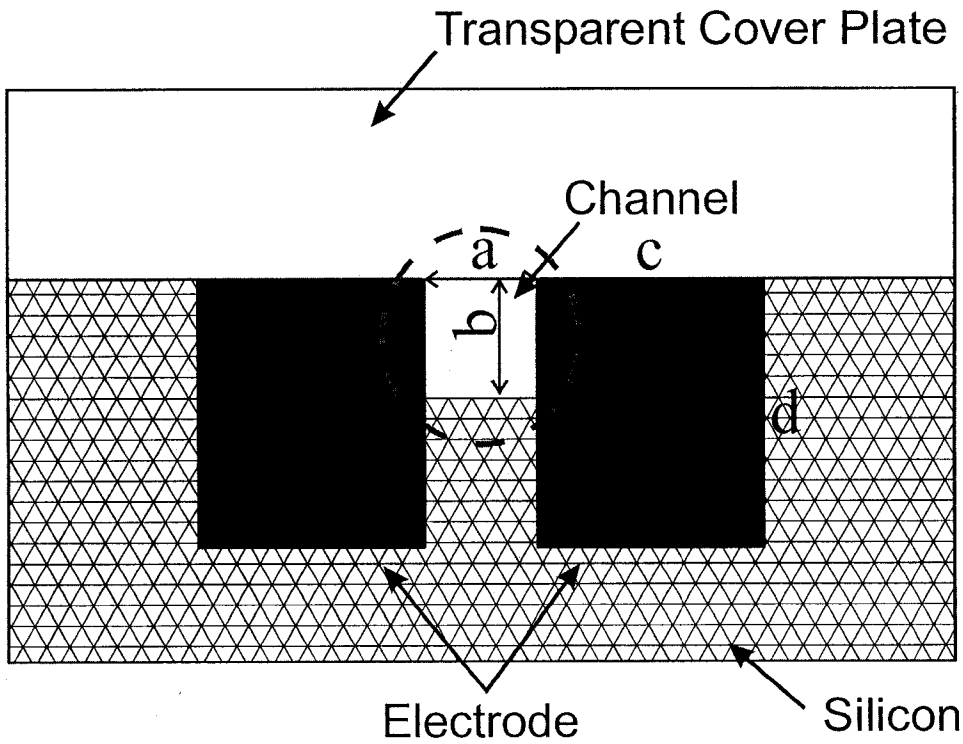

Figure 3.12. The cross-section of an EMC, in which a square channel is opened between the electrodes. A transparent cover plate is bonded to the silicon bonding nails besides the electrodes. a = b = 10 μm, c = 20 μm, d = 20 μm.

Pattern Generator, Heidelberg Instruments, Germany) process was employed, as indicated in Figure 3.13. First, grooves were opened for electroplating on a Si substrate (ϕ 4", Virgin Test, 100, P/Boron, 1-30 Ωcm, 500-550 μm, Silicon Valley Microelectronics, Inc., San Jose, CA, USA). In order to lift off the photoresist (HPR 504 in this case), it is important that it not be damaged by the plasma while doing ICP-RIE (Plasmalab System 100, Oxford Instruments, UK). Therefore, a revised Bosch process

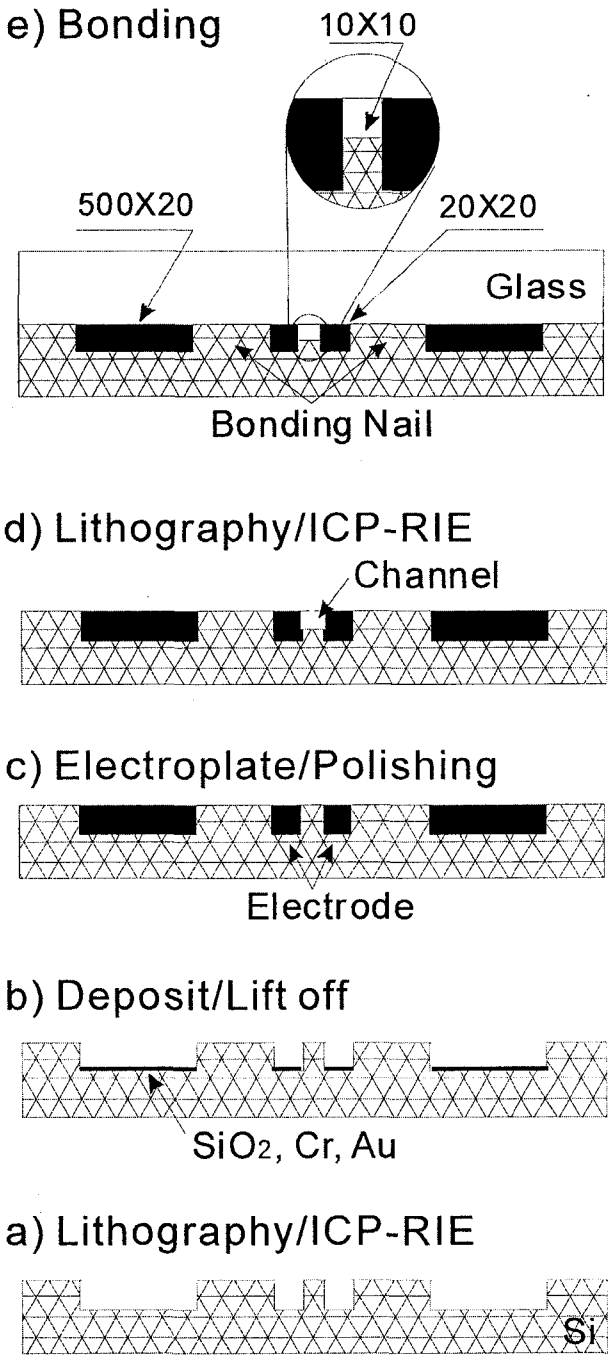

Figure 3.13. Process steps for the fabrication of EMC for MHD flow. Dimensions are in μm.

was developed in this thesis work. Compared to typical parameters offered by Oxford Instruments and the University of Alberta NanoFab, the etching step length was reduced by decreasing the flow rate of SF_6 (from 75 sccm to 65 or 70 sccm) and the etch time (from 15 to 8 sec). Damage to the photoresist was significantly reduced (the sidewall surface roughness should be improved as well). The slow etch rate (0.2 ~ 0.3 μm/step) was not a problem, because the depth required was only 20 μm. Note that this idea worked well, but the specific parameters were very sensitive to many other parameters, such as ICP chamber design, DC bias selected, wafer temperature, and even wafer coverage. Therefore, an optimization is always required.

Silicon dioxide (280 nm, 99.9999%, Kurt J. Lesker Co., Clairton, PA, USA) was deposited by an e-beam evaporator built on site (Gomez, NanoFab, University of Alberta, Edmonton, Alberta), to prevent electrical contact to the Si substrate. The evaporation rate of silicon dioxide was monitored by a quartz crystal monitor (Kurt J. Lesker Co., Clairton, PA, USA) and carefully controlled to be less than 2 Å/sec, to keep the surface temperature low and avoid damaging the HPR 504. A routine Cr/Au (20 nm Cr, 99.95%, 150 nm Au, 99.99%, Kurt J. Lesker Co., Clairton, PA, USA) sputter deposition process was employed by using a dual-target magnetron sputtering system (Kurt J. Lesker Co., Clairton, PA, USA), because HPR 504 survived the argon plasma. This gave a patterned seed layer used to initiate electroplating of Ag.

It is a big challenge to get a uniformly electroplated surface on a patterned wafer, because of unavoidable, non-uniform lines of current (Figure 1.10, ref. 14) and the resulting metal ion concentration gradients in the electroplating solution. This is true even with patented commercial deposition solutions (Silvor 90 Bright Silver Plating Solution, Technic Canada, Inc., in which there exist potassium silver cyanide and patented replenisher brightener). Slow plating (1 μm/hr) gives improved results. In this work, with current densities less than 1 mA/cm^2 for silver, the thinnest wires (20 μm wide) grew almost twice as fast as the widest wires (500 μm wide). Figure 3.14 shows typical surface roughness of a straight section of an EMC and in the vicinity of a cross junction, measured by an optical profilometer (Zygo Corporation, Middlefield, CT, USA).

Another factor causing a non-uniform electroplating surface is the different resistance of the wires in different regions. For the chip design shown in Figure 3.7, devices are surrounded by a 5 mm thick wire. This thick wire is used to reduce the resistance and hence make the surface voltage more uniform for electroplating.

Bonding requires extremely flat surfaces. Given the need to planarize these devices for bonding, and the difficulty of planarizing effectively, we set a target of less than 0.2 μm surface height variation. This was achieved by polishing with 50 nm Al_2O_3 particles (Buehler, Lake Bluff, IL, USA) prepared as a paste in distilled water. A polishing cloth (Buehler, Lake Bluff, IL, USA) was affixed to a planar pad and loaded into a drill. Polishing was done at a speed less than 100 RPM so as not to break the wafer,

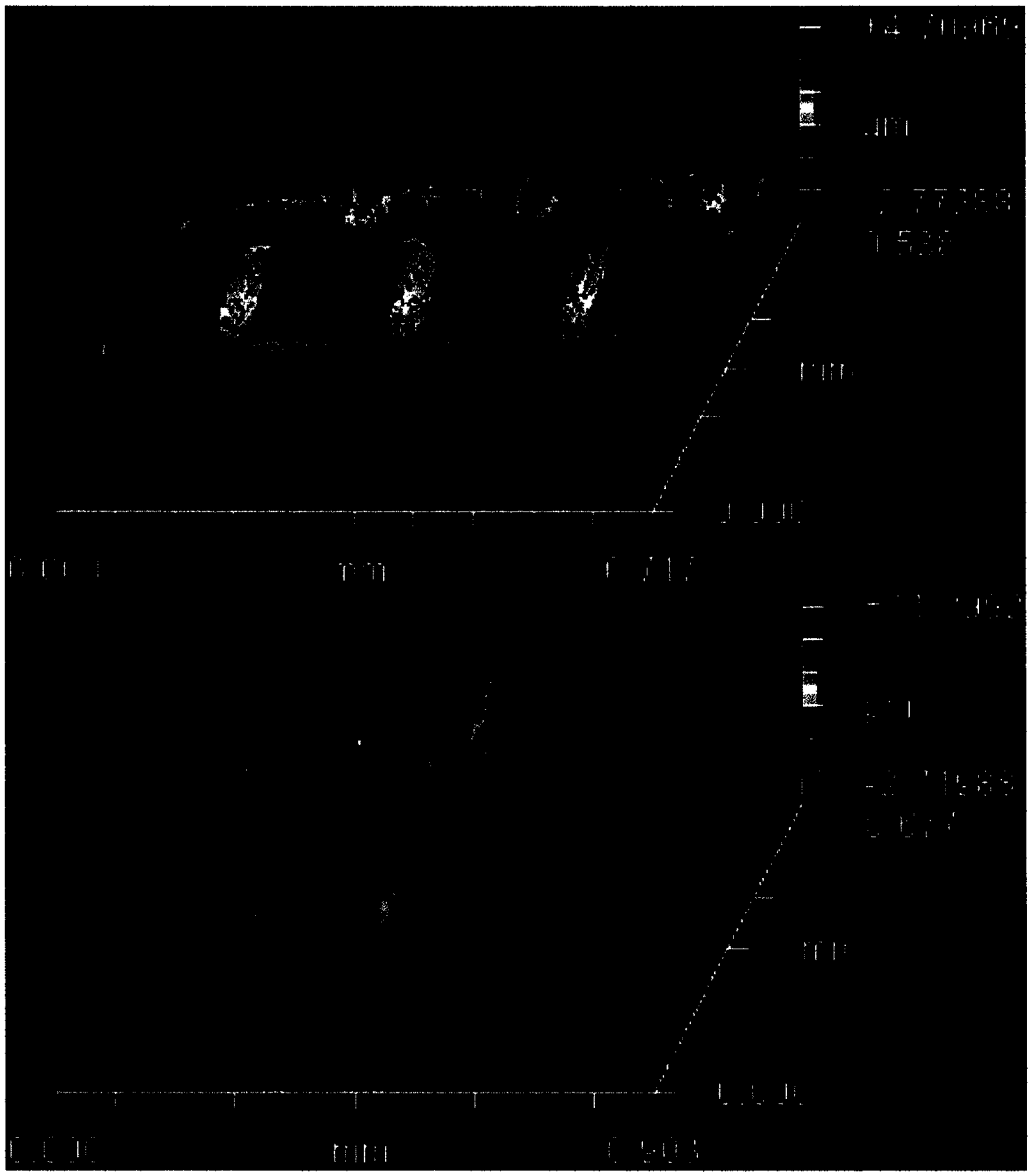

Figure 3.14. Typical surface roughness after electroplating. a) Straight channel. The thin electrodes (middle) grew faster than did the wide wires (front and back). The flat green planes are the bonding nails. b) The vicinity of a cross junction. The current density at the vicinity of a cross junction is the highest because of larger covered area, as shown in the chip design. Therefore, the electrodes grew much faster than any other regions, such as straight channels. The flat blue planes are silicon.

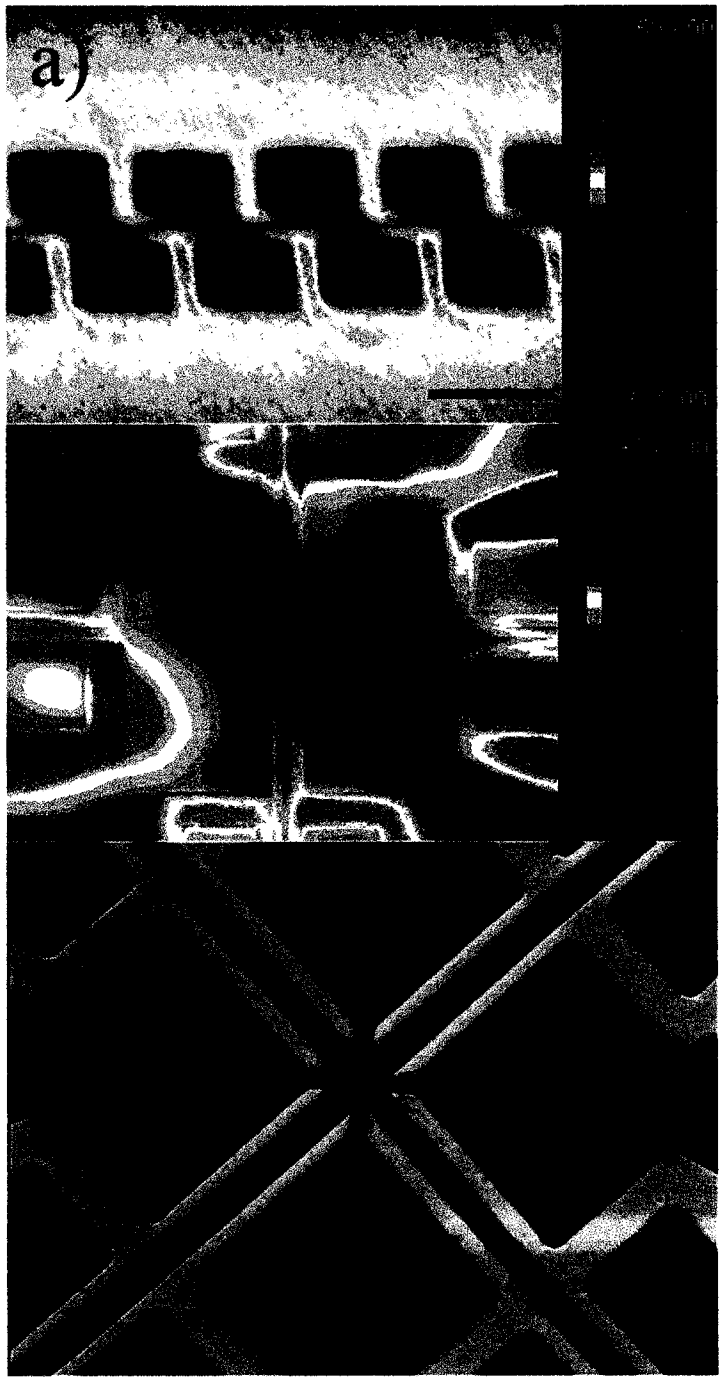

Figure 3.15. Typical surface roughness after polishing. a) Straight channel, with an RMS roughness of 91 nm. Space bar, 200 μm. b) Cross junction, with an RMS roughness of 71 nm. Space bar, 100 μm. The metal electrodes and wires (yellow) are still relatively higher than the bonding nails (blue or green). c) Photomicrograph of a cross junction. The space between electrodes is 10 μm.

requiring several hours. Figure 3.15 shows corresponding typical surfaces after polishing. The RMS roughness for both surfaces is less than 100 nm.

A second mask step was then used with ICP-RIE to etch a flow channel between the electrodes. It was suspected that gold or silver might contaminate the ICP-RIE (15). Using the Bosch process, we found it helpful to halve both etching and deposition times (etching: from 25 to 15 sec; deposition: from 8 to 5 sec). Doing so apparently lowered the possibility of damaging the electrodes with fluorine or sulphur radicals. This adjustment works especially well given that in this step only shallow channels (10 μm) were fabricated.

Finally, a 0211 glass cover plate (Corning, NY, USA) was bonded to the silicon wafer by anodic bonding. The temperature for anodic bonding should be kept low (lower than 300°C). This is because metal and silicon often have a large difference in the expansion coefficient (16). Furthermore, compared to a bulk metal, thin sheets can be oxidized at a much lower temperature. The bonding took 1-3 hours with a voltage from 1 to 3 kV. The hot plate was set between 280 and 300°C.

Besides anodic bonding, HF bonding (17) was also used. The procedure followed was essentially identical to that of ref. 17. Because of delamination, once the devices were filled with solvent for a period of time, this method was not used.

Ni was also tested as an electrode material. The current density used for Ni electroplating was 3.5 mA/cm^2. A rough surface was also observed after plating, as

shown in Figure 3.16a. Ni electrodes were also polished by using 50 nm Al_2O_3 particles. Compared to Ag, Ni was relatively easier to polish, and hence polishing was done manually. This may be because Ni is harder than Ag, and a hard metal is believed to be easier to polish (18). Figure 3.16b shows the surface after polishing.

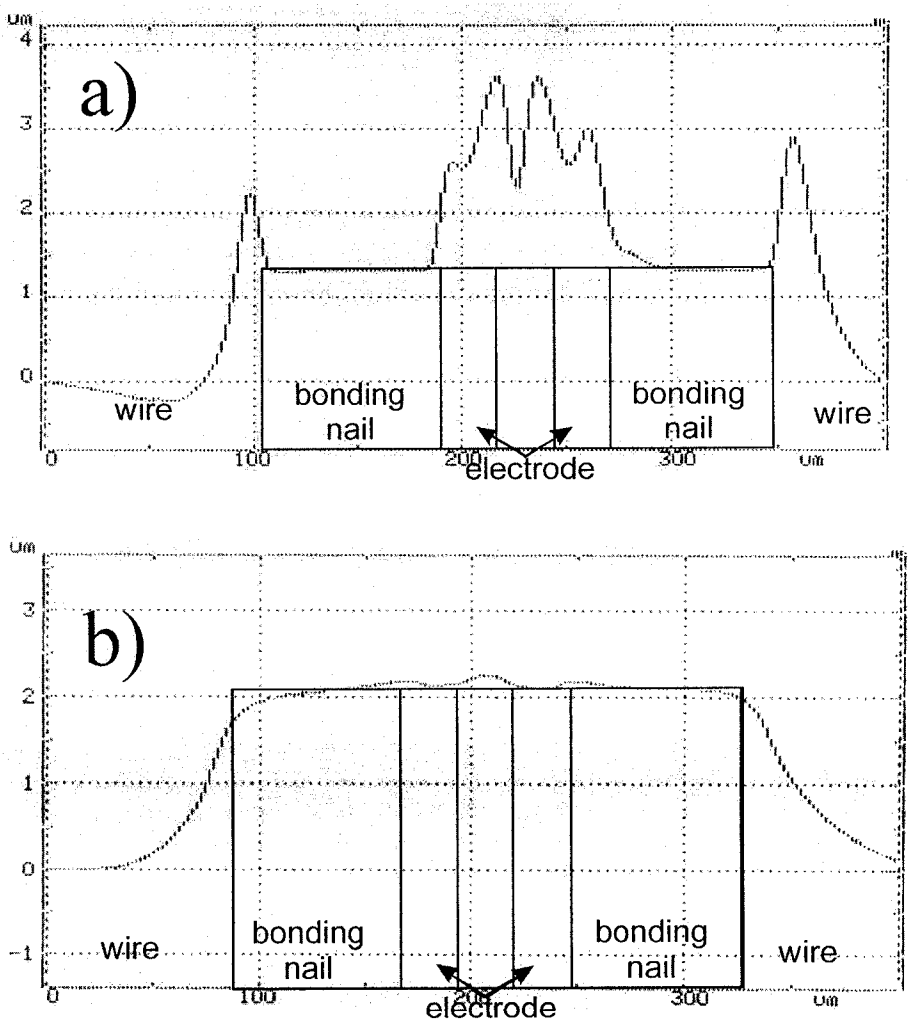

Figure 3.16. Surface roughness of nickel electrode. a) after electroplating; b) after several hours manual polishing.

3.5 Characterization and Discussion

Figure 3.17 shows photos of three typical, realized device elements: a straight channel, T-junction, and cross junction. A finished device M is shown in Figure 3.18, in which there are 5 reservoirs, 10 pin wires connected to outside power suppliers, and a prism for detection. Electrodes in each channel segment can be individually addressed. For example, if we apply a voltage to pins 2 and 3, we should be able to generate pumping for the arm to SW. Similarly, if we apply a voltage to pins 1 and 0, then we can pump liquid in the arm to BW.

Tests on bubble current density threshold (Figure 3.19) were done with Ag electrodes formed in the chip, showing more than 20% higher current density than those of Lemoff and Lee (4, 5) can be applied in the EMC. Lemoff and Lee used Pt as the electrodes. The use of Ag electrodes may be the reason for the improved current density, because roughed electrode surfaces were observed under the microscope after several hours of operation. Increased surface roughness is likely indicative of Ag oxidation and re-deposition. Higher current density will allow higher pumping rates, or the use of lower frequencies and weaker magnetic fields.

3.6 Conclusions

We have designed and fabricated an EMC which can potentially generate more powerful MHD pumping in a channel with a 10 μm square cross section. Four different

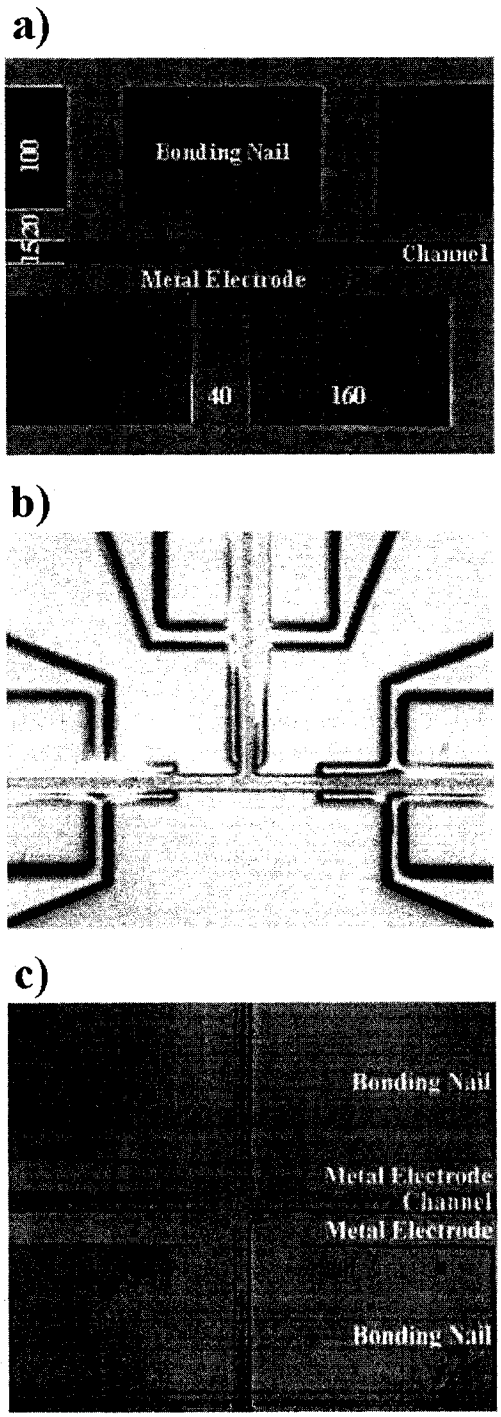

Figure 3.17. Photomicrographs for MHD channels in different shapes. a) Straight channel; b) T-junction, with three pairs of isolated electrodes; c) Cross junction, with four pairs of electrodes.

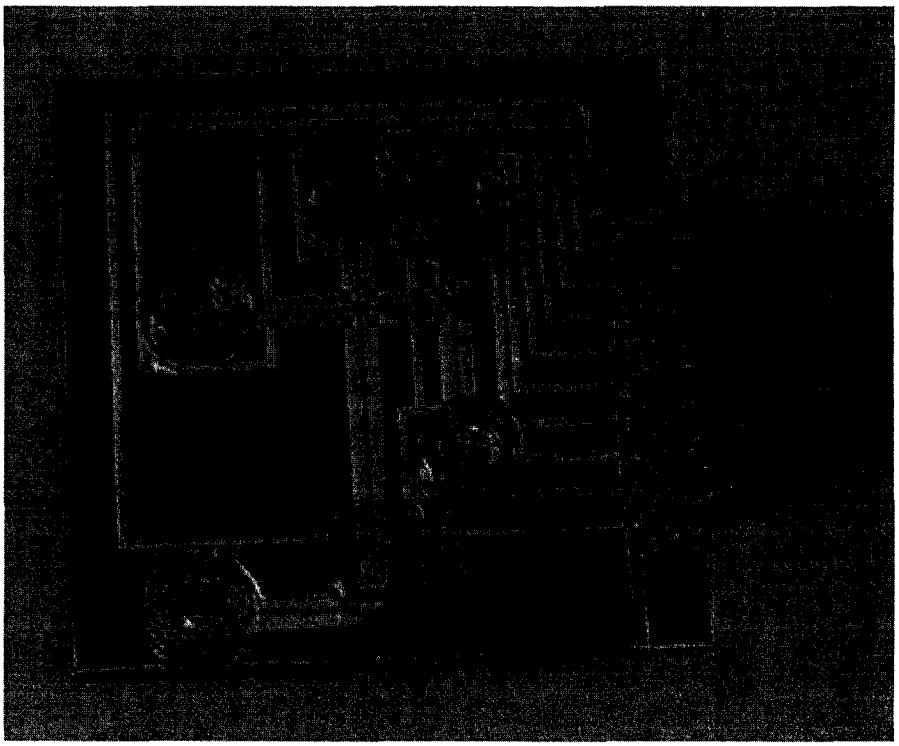

Figure 3.18. Final device M (34 mm × 34 mm), in which each arm can be individually addressed.

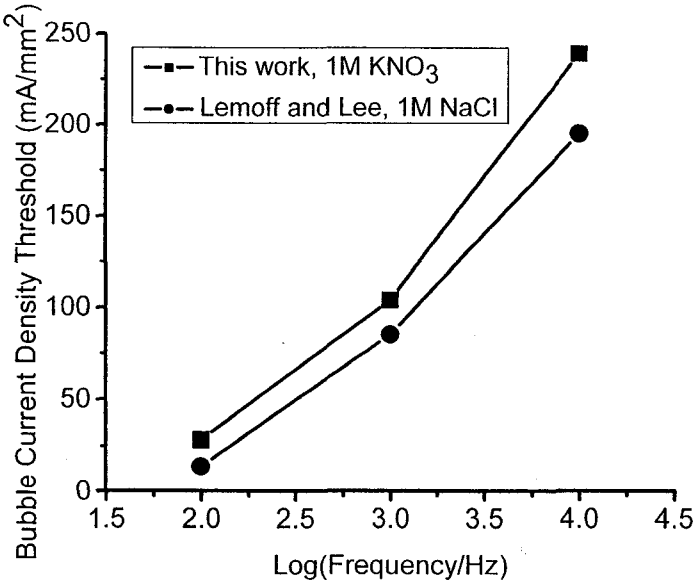

Figure 3.19. Experimental bubble current density thresholds of EMC.

OTLC design concepts were developed, each of which may have certain advantages. A solvent program could be realized by a voltage program merging weak solvent with strong solvent. A 20 cm long separation channel was realized by serpentine shape in a 34 mm × 34 mm wafer, which might generate about 10,000 plates. The channel size is small enough for this OTLC chromatographic method to be effected. The challenges associated with fabrication have been overcome by optimizing electroplating conditions, developing polishing techniques for planarization of rough electrochemical surfaces, and reducing the ICP-RIE etching rates. A higher experimental bubble current density threshold was obtained which would enhance MHD pumping velocity.

The problems in metallizing and planarizing MHD devices are actually very similar to current metallization challenges in ULSI microchip fabrication. Chemical mechanical polishing (CMP) with a slurry has been widely used in the damascene process to metallize Al or Cu vias formed in ULSI microchips (19). Silver may in fact be the material used for the next ULSI generation, but CMP of patterned silver is in its infancy (18). We have shown a high planarity can be achieved by oxide particle polishing, without any chemical agents. Therefore, this Ag patterning technique could be very useful for the IC industry.

3.7 References

1. Harrison, D. J.; Manz, A.; Fan, Z.; Lfidi, H.; Widmer, H. M. *Anal. Chem.* **1992**, 64, 1926-1932.
2. Harrison, D. J.; Fluri, K.; Seiler, K.; Fan, Z.; Effenhauser, C. S.; Manz, A. *Science* **1993**, 261, 895-897.
3. Fan, Z. H.; Harrison, D. J. *Anal. Chem.* **1994**, 66, 177-184.
4. Lemoff, A. V.; Lee, A. P.; Miles, R. R.; McConaghy, C. F. *Transducers '99*, 1126-1129.
5. Lemoff, A. V.; Lee, A. P. *Sens. Actuators B* **2000**, 63, 178-185.
6. Eijkel, J. C. T.; Dalton, C.; Hayden, C. J.; Drysdale, J. A.; Kwok, J. C.; Manz, A. In *Proceedings of Micro Total Analysis Systems 2001*; Kluwer Academic Publications: Dordrecht, The Netherlands, **2001**, 541–542.
7. Eijkel, J. C. T.; Dalton, C.; Hayden, C. J.; Burt, J. P. H.; Manz, A. *Sens. Actuators B* **2003**, 92, 215-221.
8. Fried, E.; Idelchik, I. E. *Flow resistance: a design guide for engineers*; Hemisphere: New York, **1989**, pp. 22.
9. Senturia, S. D.; Schmidt, M. A.; Harrison, D. J. *Microsystems: Mechanical, Chemical, Optical*, Lecture Notes, Massachusetts Institute of Technology, **1998**.
10. Fan, Z. H.; Harrison, D. J. *Anal. Chem.* **1993**, 66, 177-184.
11. Gohlin, K.; Larsson, M. Chromatographia **1994**, 39, 729.

12. Burggraf, N.; Manz, A.; Verpoorte, E.; Effenhauser, C. S.; Widmer, H. M. *Sens. Actuators B* **1994**, 20, 103-110.

13. Chang, S.-C.; Shieh, J.-M.; Dai, B.-T.; Feng, M.-S.; Li, Y.-H.; Shih, C. H.; Tsai, M. H.; Shue, S. L.; Liang, R. S.; Wang, Y.-L. *Electrochem. Solid-State Let.* **2003**, 6, G72-G74.

14. Judy, J. W. http://www.ee.ucla.edu/research/judylab/procedures/.

15. Schmidt, M. A. Private communication.

16. Lide, D. R. (Ed.) *Handbook of Chemistry and Physics*; 83rd ed.; CRC Press: Boca Raton, **2002-2003.**

17. Nakanishia, H.; Nishimotoa, T.; Nakamurab, R.; Yotsumotob, A.; Yoshidaa, T.; Shojib, S. *Sens. Actuators A* **2000**, 79, 237-244.

18. Hauder, M.; Gstottner, J.; Gao, L.; Schmitt-Landsiedel, D. *Microelectron. Eng.* **2002**, 64, 73-79.

19. Wrschka, P.; Hernandez, J.; Oehrlein, G. S.; Negrych, J. A.; Haag, G.; Rau, P.; Curriec; J. E. *J. Electrochem. Soc.* **2001**, 148, G321-G325.

Chapter 4

Rotating Permanent Magnets for AC Magnetohydrodynamic Pumping

4.1 Introduction

The EMC design introduced in Chapter 3 for magnetohydrodynamic pumping allows higher currents to pass through electrolyte solutions, but electrolysis will still happen, generating gas bubbles in the microchip channels once the bubble threshold is reached. According to Lemoff and Lee (1, 2), bubbles can be suppressed by an AC electric current coupled with an AC magnetic field. For an AC electric field, the bubble current density threshold is a function of the field frequency. Increasing the frequency allows higher current density to be achieved without bubble formation (Figure 1.4). However, for AC magnetic fields generated by an electromagnet, increasing the frequency significantly lowers the magnetic field strength (Figure 1.5). In fact, for electromagnets – the most common source of AC magnetic field, the field strength is designed at 50-60 Hz (1, 2). Due to the hysteresis and eddy currents generated in the core materials (usually ferrite) by an electrically induced magnetic field (3), electromagnets are not recommended for use beyond 400 Hz (4). For a commercial electromagnet with a field strength of 1 T or so, GMW Associates describe the magnets as "dangerous if used

beyond 400 Hz." (4) Electromagnets can get very hot even at 60 Hz and need a water cooling system. Both Lemoff *et al.* (1, 2) and Eijkel *et al.* (5, 6) used electromagnets at 1 kHz or higher, but Lemoff's magnet was very small. (B = 7.4-18.7 mT). Eijkel's (B = 105 mT) somewhat larger magnet became quite hot, as he mentioned in the paper (6).

In this chapter, I will present an idea for generating a strong AC magnetic field for frequencies of several hundred Hz, with a potential for up to 1 kHz. The field strength should not vary with frequency. In order to use this AC magnet for MHD, corresponding chip mount, detector, and electronic control systems have also been designed.

4.2 Design

4.2.1 Calculated Pumping Velocities for AC Electromagnets

It is important to know what pumping velocity could be realized using commercial AC magnets before undertaking a new magnet design. Table 4.1 lists those predicted by using Equation 3.4 for the EMC design. As discussed in section 1.2.1, in order to get a small plate height for open tubular liquid chromatography (OTLC), the channel size should not exceed 10 μm. Suppose both Lemoff and Eijkel's electromagnets are used at 1 kHz, then according to Figure 3.19, the maximum current density will be 100 mA/mm^2. Obviously, the calculated pumping velocities are too slow. GMW Associates manufactured an AC electromagnet, which can produce a flux density of ~ 1.6

T (7). It was designed for 60 Hz, so the current density due to the bubble threshold limit is as small as 20 mA/mm^2, and hence a theoretical pumping velocity of 0.12 mm/sec could be achieved. By using it, we will be unable to do research at any other frequency. It is also very expensive (> US$25,000). Therefore, commercial products, in this case, were not our choice. In order to achieve a pumping velocity of 0.1 mm/sec, we predicted that a minimum flux density of 0.256 T was required if the frequency could reach 1 kHz, as shown in Table 4.1. We then decided to design an AC magnet to meet these requirements.

The details of the analysis leading to the last two experimental entries in Table 4.1 are given later in this Chapter.

Table 4.1. Calculated pumping velocities for AC electromagnets

D	W	f	j_b	B	v	Source
μm	μm	Hz	mA/mm^2	T	mm/sec	
10	10	1000	100	0.0187	0.007	Lemoff
10	10	1000	100	0.105	0.041	Eijkel
10	10	60	20	1.6	0.12	GMW
10	10	1000	100	0.256	0.1	Predicted
10	10	200	46	0.552	0.1	This work
10	10	480	78	0.552	0.16	This work

4.2.2 Permanent Magnet and Its Field Strength

No doubt the simplest and cheapest magnet is a permanent magnet. For a rectangular permanent magnet as shown in Figure 4.1a, the flux density B outside the magnet can be empirically predicted (8) by

$$B=\frac{B_r}{\pi}\left(\tan^{-1}\frac{ab}{2x\sqrt{4x^2+a^2+b^2}}-\tan^{-1}\frac{ab}{2(l+x)\sqrt{4(l+x)^2+a^2+b^2}}\right) \tag{4.1}$$

where B_r is the residual flux density of the material, a and b are the dimensions of the magnet perpendicular to the magnetic field, l is the length of the magnet along the magnetic field, x is the distance from the measured point to the magnet surface.

In terms of the material, permanent magnets can be divided into different categories: rare earths, ceramics, alnico, and flexibles, etc. (8) Among them, the rare earth neodymium-iron-boron magnet has the largest residual flux density, and hence the strongest field strength. The flux density can be doubled by facing two identical magnets towards each other in attracting positions (Figure 4.1b). It can be further strengthened by yoking them as shown in Figure 4.1c. For a perfect yoke, the flux density can be calculated by

$$B=\frac{2B_r}{\pi}\left(\tan^{-1}\frac{ab}{2x\sqrt{4x^2+a^2+b^2}}-\tan^{-1}\frac{ab}{2(2l+x)\sqrt{4(2l+x)^2+a^2+b^2}}\right) \tag{4.2}$$

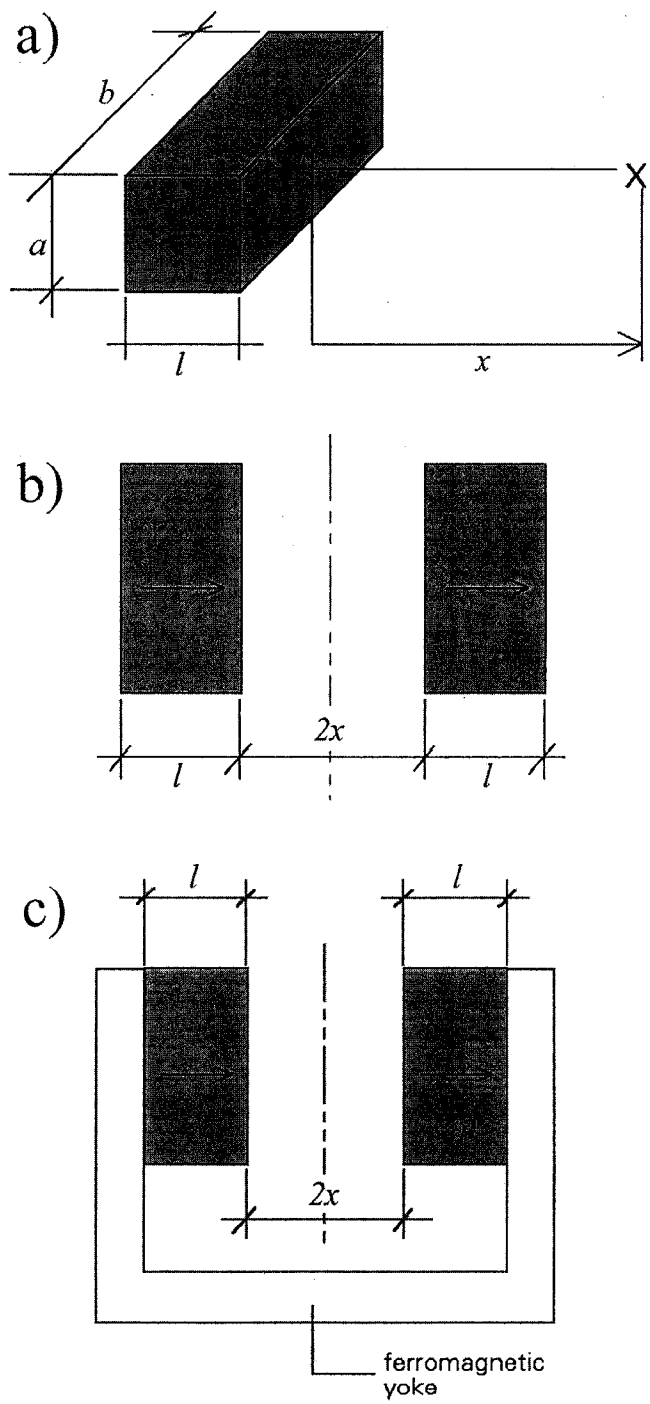

Figure 4.1. Field strength of permanent magnets. a) single; b) two magnets facing each other in attracting positions; c) attracting magnets with an additional ferromagnetic yoke.

4.2.3 Rotating Permanent Magnets

By using these strong permanent magnets mounted in a rotor, we are able to create an AC magnet. Figure 4.2 depicts the idea: If permanent magnets are mounted alternately onto a magnet holder as in Figure 4.2 and if the holder is rotated, then any point above the holder will face north and south periodically – generating an AC magnetic field. The frequency of this alternating field depends on the number of magnetic pairs in the holder and on the rotation speed, while its field strength depends upon the magnets used, not on the frequency. By taking the ideas in Figure 4.1b, if two holders are made to face each other with magnets in attracting positions (i.e. the north side of the magnet on one holder faces the south side on the other), the magnetic field will be doubled. Another advantage is that the field in the gap space will be more uniform, which is important because the gap is where the microchips will be inserted. A yoke such as in Figure 4.1c is not the best option in this case, because of obvious manufacturing difficulties. A simpler and more powerful design is to put a yoke plane, as shown in Figure 4.2b, on each of the two facing magnet holders. It can strengthen the field better because each magnet is yoked by two adjacent magnets as indicated by the arrows in Figure 4.2a. Moreover, yoke planes can also shield the magnetic field well, creating less field leakage and external interference.

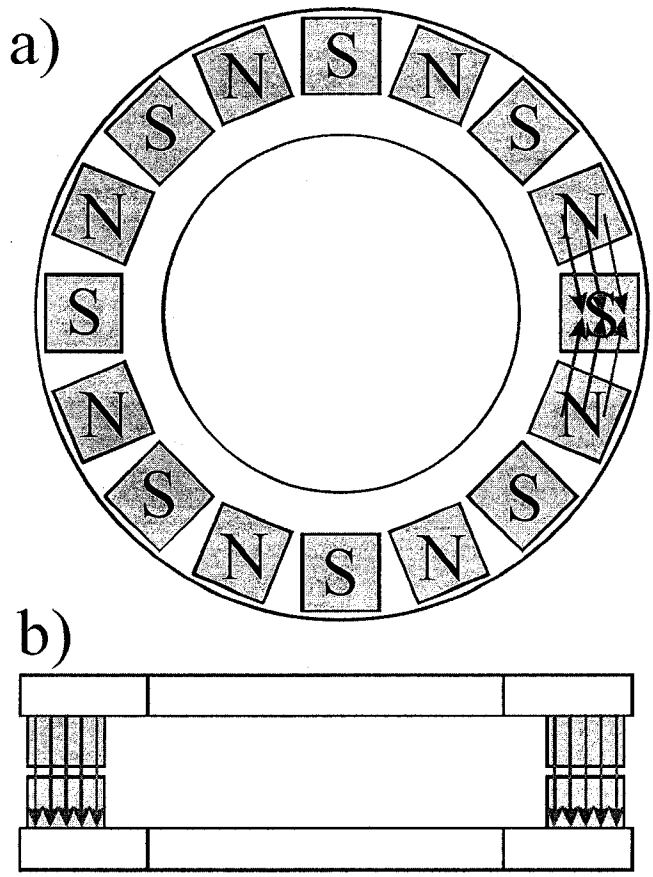

Figure 4.2. Rotating permanent magnets. a) mount magnets alternately, arrows indicate each magnet is yoked by two adjacent magnets; b) magnets with yoke rings.

4.3 Experimental

4.3.1 AC Magnet

Thirty-two sintered neodymium-iron-boron magnets (N5064, B_r = 1.44 T) were manufactured by Magnetic Component Engineering, Inc, Torrance, CA. The length of

each magnet along the magnetic field axis is 0.5", while the size perpendicular to the field is 1" × 1". The field strength and direction were detected with a gaussmeter (Field Monitor, Model 810H, 10X probe, F. W. Bell Inc., Columbus, OH, USA).

Two magnet holders (ϕ8" × 0.504") were made of 6061 aluminum, in each of which 16 magnets were mounted alternately as shown in Figure 4.3. A 1 mm thick lip was designed at the lower surface of the holder to stop super strong attractions between magnets when they are placed in attracting positions. Special epoxy glue (Speed Bonder Product H4500, Loctite, Rocky Hill, CT) was used to immobilize the magnets. On each magnetic holder, an iron steel plane (ϕ8" × 3/8") was accurately placed and co-centered with the magnetic holder, creating one half of the rotor. Finally, the half rotors were mounted together to form the complete rotor (Figure 4.4). Because the attractive forces affected alignment, the assembly steps were done slowly and carefully, using Teflon strips as buffers to allow small adjustments. The gap between the magnet holders is 8 mm, meaning that the distance between the magnets is 10 mm.

The rotor was screwed onto a ϕ1" 304 stainless steel shaft and balanced at an Edmonton International Airport turbine firm using facilities obtained from NASA. By using two super precision bearings (6205TBR12P4, RHP, UK), the rotor was eventually mounted onto an aluminum station as shown in Figure 4.5. By doing so, no ferromagnetic

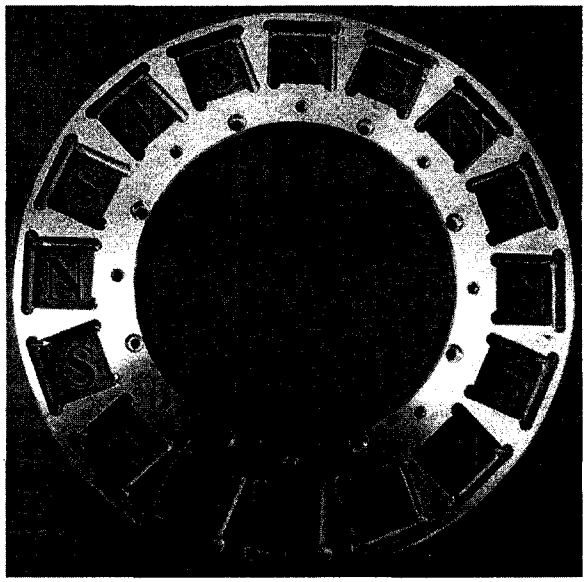

Figure 4.3. Magnet holder (top view, ϕ8")

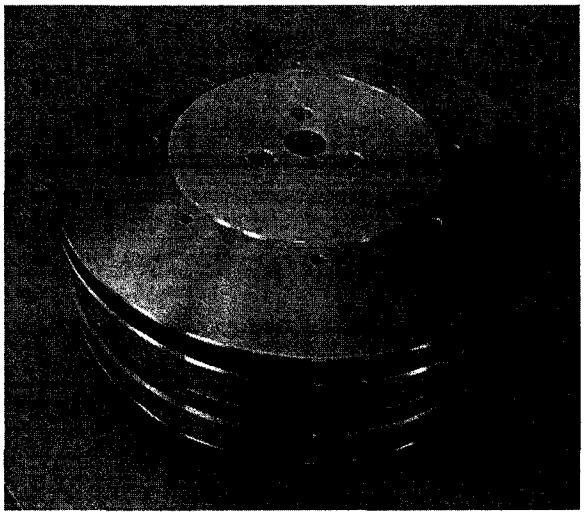

Figure 4.4. Magnet rotor (ϕ8" × 2") composed of (from top to bottom) yoke plane, magnet holder, gap (8 mm), magnet holder and yoke plane.

materials were used in the vicinity of the rotor. Finally, the assembly was then fixed onto a steel station with a weight of 0.5 tons so as to minimize any vibration (Figure 4.5).

The rotor was powered by a DC motor (CDP3445, 1 horsepower, maximum speed: 1750 RPM, Baldor Motors and Drives, Fort Smith, AR, USA) with a DC motor speed control (MSC 700, MagneTek, El Paso, TX, USA). By using gears and belt, the speed of the rotor is accelerated to 4.5 (72 teeth versus 16 teeth) times of that of the motor, giving a maximum 7875 RPM for the rotor.

4.3.2 Prism Coupled LIF Detection

Laser induced fluorescence (LIF) was used for detection. A right-angle mini-prism (3.3 mm, Melles Griot, Carlsbad, CA, USA) was used to reflect excitation and emission light, as shown in Figures 4.6 and 4.7. In order to immobilize the prism, epoxy glue was applied to a side (not the bottom) of the prism. We refer to this as *prism coupled LIF*. A home made confocal microscope (9) was mounted horizontally on a long range translational stage (UniSlide A6018B-S6-TL, Velmex, Bloomfield, NY, USA) as shown in Figure 4.8. A mirror used to reflect the laser into the microscope was also mounted on the same translational stage. A red diode laser (635 nm, ACM08/2004, Power Technology Inc., Little Rock, AR, USA) was used for the excitation source (10). The beam was directed by two mirrors onto the *stage mounted* mirror. A dichroic mirror

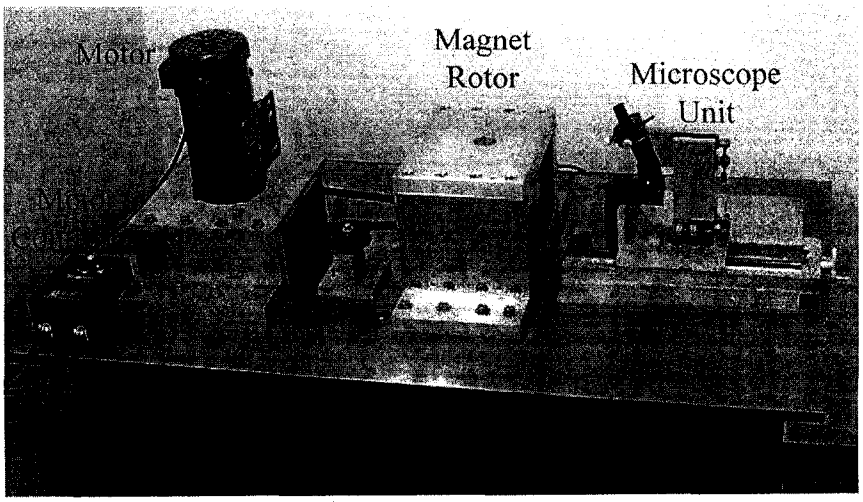

Figure 4.5. AC magnet station

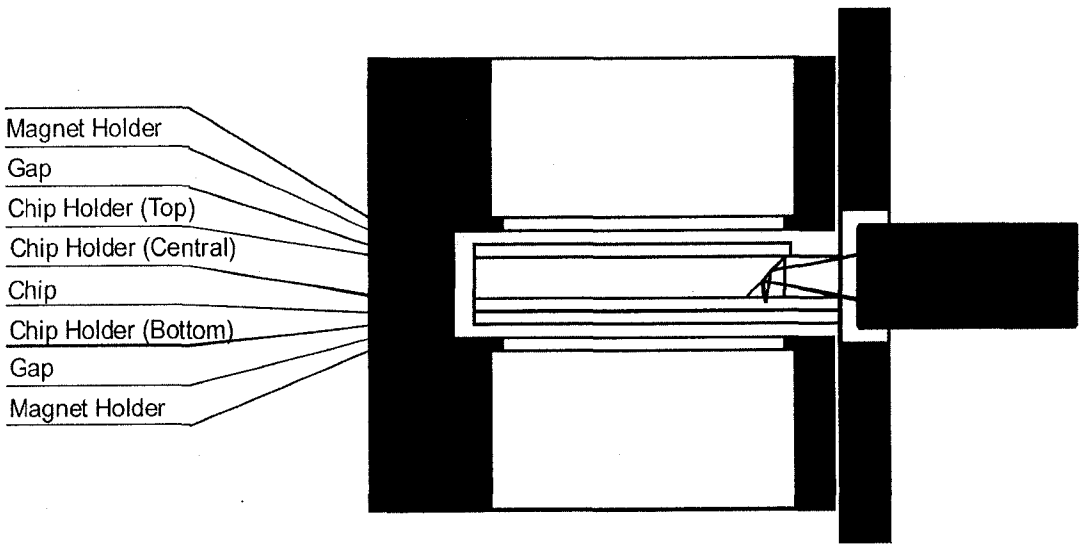

Figure 4.6. Schematic diagram of the prism coupled LIF.

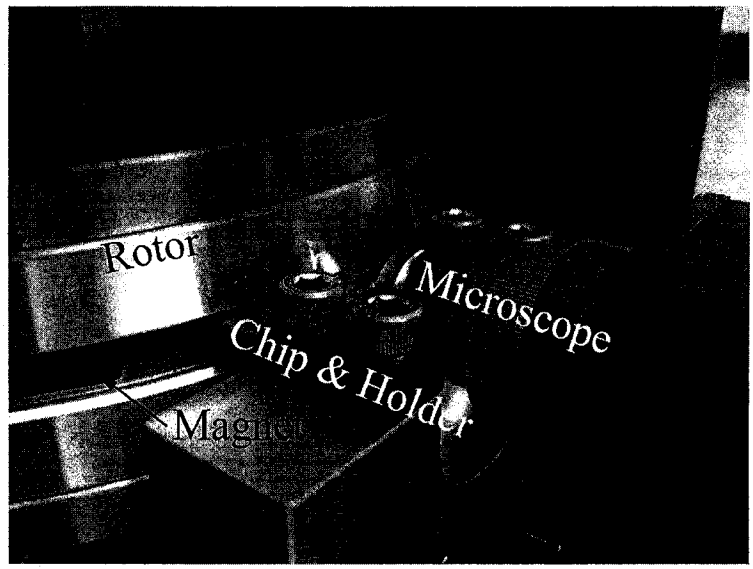

Figure 4.7. Image of prism coupled LIF

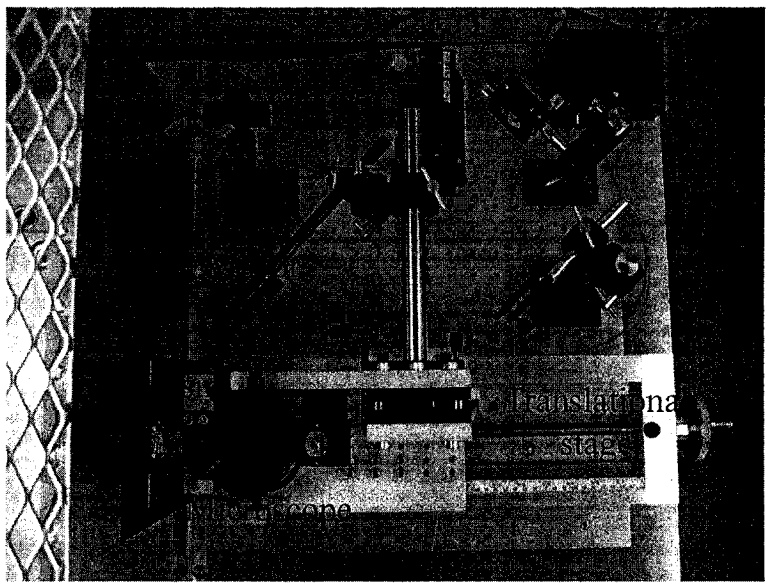

Figure 4.8. Optical microscope setup. By two mirrors (unmarked), a red laser is reflected parallel to the translational stage; a stage mounted mirror is used to reflect the light into the microscope, so that any movement of the microscope along the translational stage will not affect the laser focusing.

(645DRLP02, Omega, Battleboro, VT, USA) in the microscope directed the beam to the objective lens. The objective lens (5709, New Focus, Santa Clara, CA, USA) had 10X power, and a 13.3 mm working distance so that it could be positioned outside the magnetic field. No further alignment was required after the initial adjustments. The working distance of the objective lens was taken by the chip (0.5 mm, half of the chip width), prism (3.3 mm), chip edge (6 mm), gap between the chip and the lens (3 mm), and lens holder (0.5 mm), as shown in Figure 4.9. Samples were added into the reservoirs of the chip before it was inserted into the magnetic field region.

4.3.3 Generation of a Coupled Electric Field

A signal pickup coil was prepared. Figure 4.10 shows the groove for the coil, milled in a 5 mm thick Delrin holder. Ten loops of transformer wire were placed into the groove. When the rotor was rotating, an AC electromotive force (emf) was generated, which had the same frequency as the magnetic field. The coil was designed to be an arc with an angle of 22.5°, corresponding to the angle of two adjacent magnet (360°/16 = 22.5°). The Delrin holder was mounted co-centering with the rotor within the magnet gap. With this design, the emf did not cancel out because the two straight arms never faced the same magnet. The pick up signal was amplified (gain was more or less than 1) by a homemade amplifier and then fed to the electrodes on the chip as the electric voltage

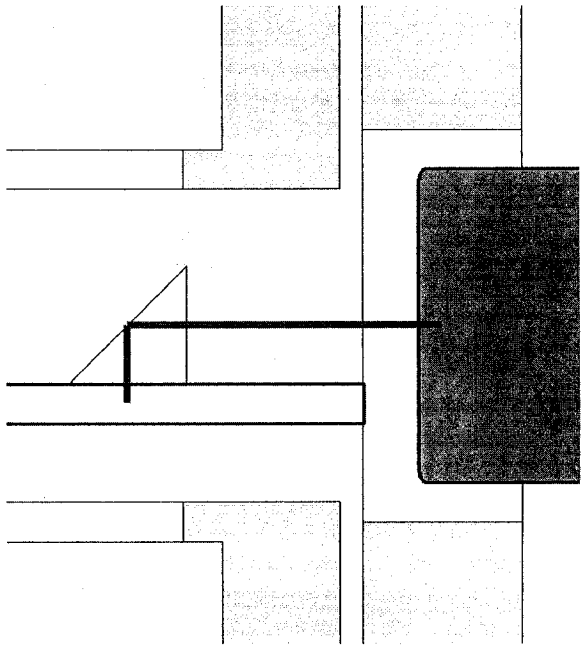

Figure 4.9. Objective working distance (13.3 mm): chip (0.5 mm, half of the chip width), prism (3.3 mm), chip edge (6 mm), gap between the chip and the lens (3 mm), and lens holder (0.5 mm).

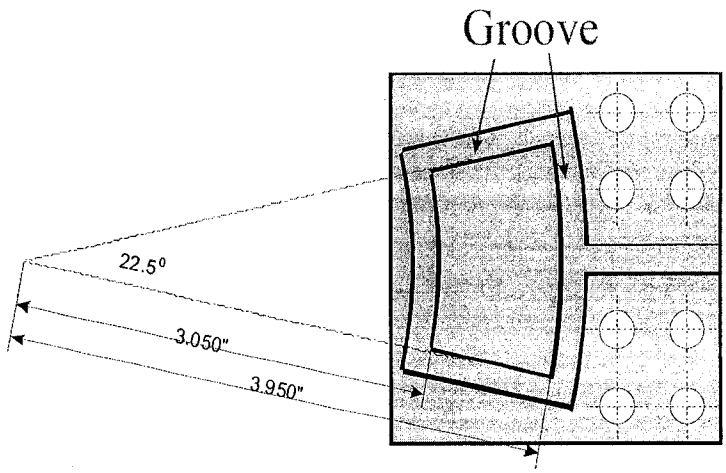

Figure 4.10. Groove design for pickup coil

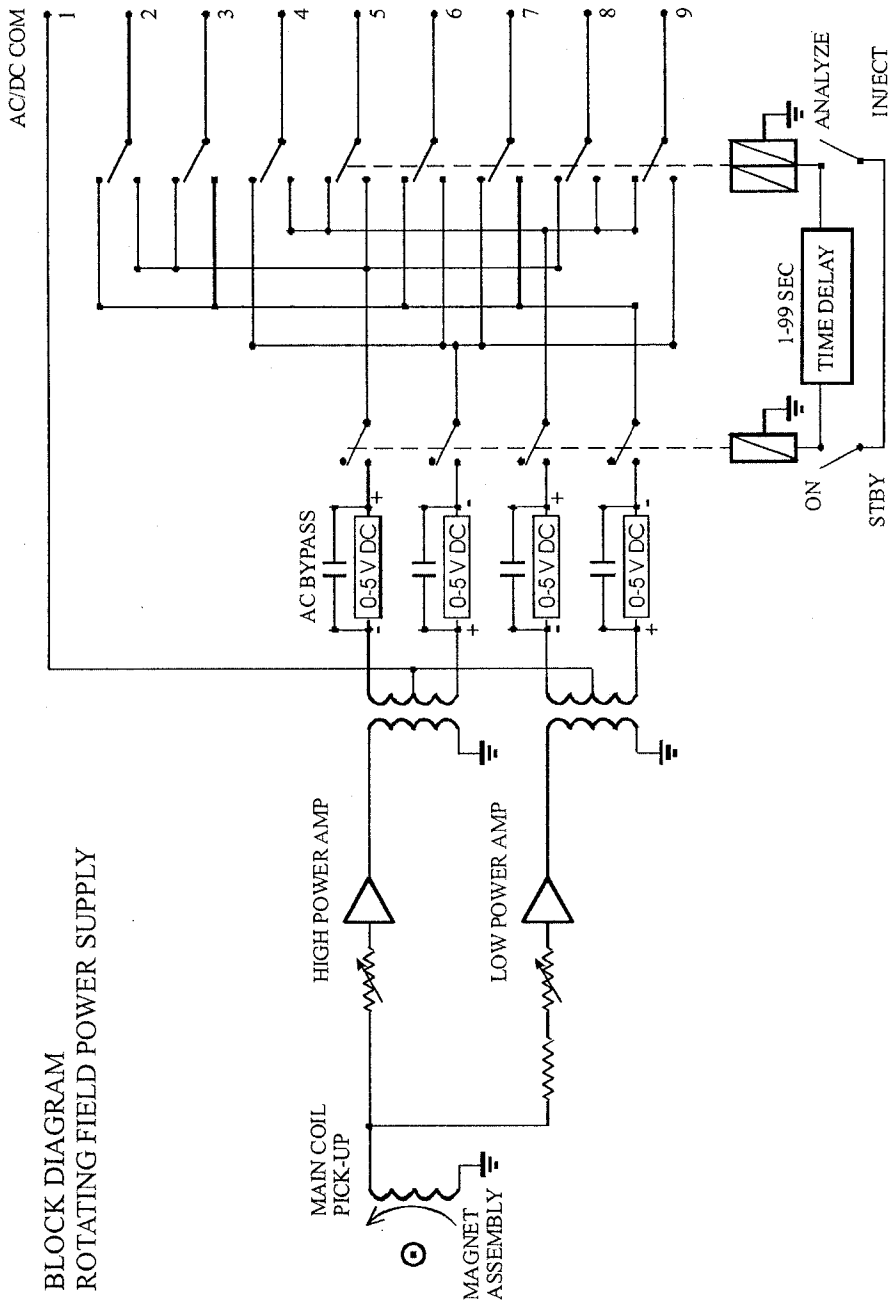

Figure 4.11. Block diagram of the power supply, including an AC amplifier and a DC power source. Pure AC, pure DC (which will be used in Chapter 5), or AC voltages with offset can be generated for operating MHD LC microchips.

source. Figure 4.11 shows part of the circuit diagram of the amplifier, in which two gains with higher or lower amplitudes were realized. The phase adjustment unit is not shown in the diagram.

4.4 Characterization and Discussions

4.4.1 Wobbling of the Rotor

Figure 4.12 shows the *play* of the rotor in the static state, i.e. without rotating, measured by a dial indicator, a form of caliper. The dynamic wobbling could not be measured in our lab but was minimized when the rotor was balanced. The small wobble that remained did not affect the rotation up to 3600 RPM, even though the gap between the rotor and the chip holder was as small as 1.1 mm. We did not test at a higher speed because the vibration increased. Since any damage to this system is irreversible, we did not want to take any risks before enough information was collected at low frequencies or RPMs.

4.4.2 Detection System

An MHD pump involves two electric fields: a) primary electric field for MHD pumping; b) secondary electric field induced by the flow, which is a function of the flow velocity. Therefore, electrochemical detection would not be an easy option to implement

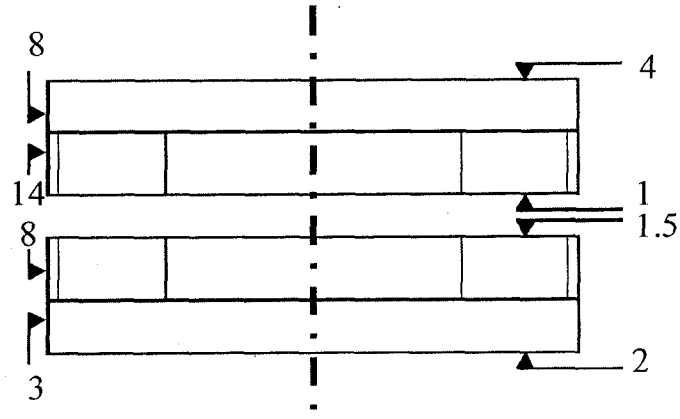

Figure 4.12. Wobbling of the rotor in units of thousandth of an inch.

for MHD, because a) the background currents from the applied voltage and eddy currents will be significant; b) any instability of the flow will cause noise due to the secondary electric field changes; c) the greatest problem is that the sample may be consumed in the EMC. Laser induced fluorescence (LIF) detection which isolates the detection signal from the electric fields is a good choice for detection. Its high sensitivity is vital for LC chips because open-tubular liquid chromatography (OTLC) has a relatively low sample capacity. However, the typical inverted or conventional microscope detector design used with CE chips is unsuitable, because the space above and below the chip is occupied by the magnets (the gap is 8 mm). The prism coupled LIF solved this problem. As shown in Figures 4.6 and 4.9, a prism was used to couple the excitation and emission light to and from the chip, while it was inside the magnetic rotor gap. An epiluminescent microscope

was mounted horizontally to interface with the chip through the prism. Figures 4.7 and 4.8 show the microscope mount and optical stage used for the detection system.

4.4.3 Mounting Microchips between Magnets

It is an obvious challenge to mount a chip between the magnets. Since the rotor is rotating at a high speed, the chip will experience vigorous air flow which might cause wobbling. A strong chip holder is required, but not one made of metal, because of eddy current heating induced under an AC magnetic field. Delrin, a strong plastic, was therefore used (Figure 4.13). The chip holder has the same thickness as the prism (and the height of the reservoirs as well), so that no extra space is taken. A chip (1 mm thick) was fixed in place using a bottom piece (1 mm thick) which was also made of Delrin. A cover (polyethylene, 0.5 mm thick) above the reservoirs was also required, so as to eliminate any possible siphon effect on the reservoirs, caused by air flow, and to reduce vaporization of the solutions. This cover should be transparent. This assembly was then inserted in the field gap with careful height adjustment, so that each side had a 1.1 mm gap between the rotor and the chip holder, as schematically illustrated in Figure 4.6. Finally, the distance between the channel and objective lens must be shorter than the working distance of the objective lens (13.3 mm), because the channel on the chip must be optically accessible by the microscope.

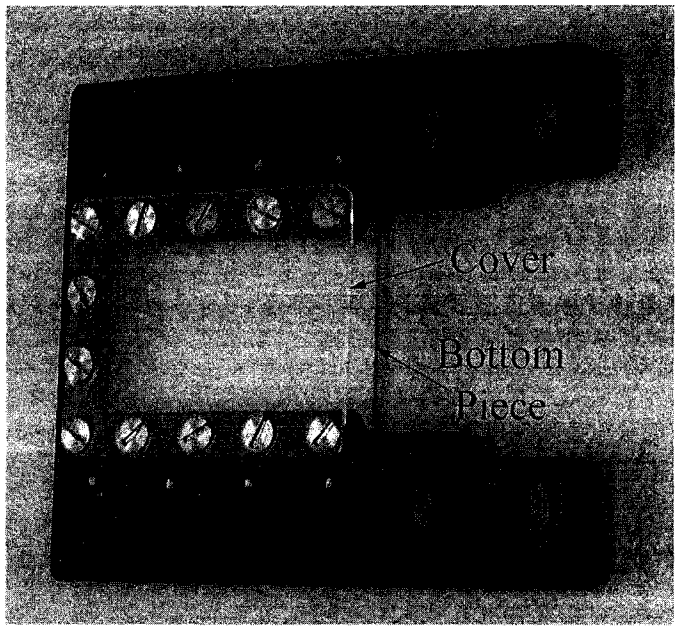

Figure 4.13. Chip holder (2.4" × 2.1") with cover and bottom piece.

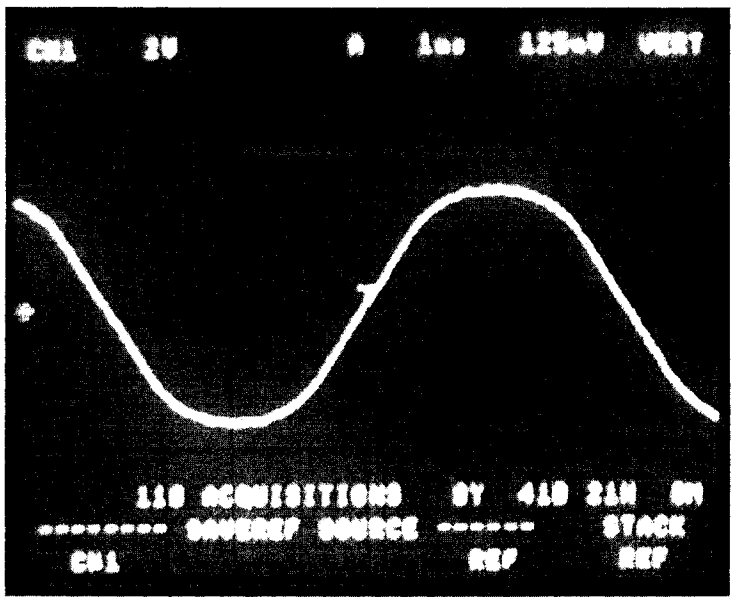

Figure 4.14. Waveform picked up from AC magnetic field.

4.4.4. Synchronizing the Electric and Magnetic Field

As discussed by Lemoff and Lee (1), the Lorentz force generated by AC MHD is a time-averaged force. In order to realize AC MHD pumping, the Lorentz force generated at each period should point in the same direction. The peak and direction of the electric field should match that of the magnetic field, so as to induce the highest pumping force. Therefore, frequency matching and phase matching between the electric current in the channel and the magnetic field is required. Any frequency or phase mismatching will reduce the strength of the Lorentz force. This is easy when using electromagnets, but for a rotating magnetic field, the frequency and phase are determined by the rotor and are fairly easily influenced by environmental variables. The pickup coil picked the magnetic field and converted into an electric signal. Figure 4.14 shows a 100 Hz waveform obtained at a rotor speed of 750 RPM. By using this signal, phase matching will no longer be a problem.

4.4.5 Field Strength

Minimal field strength differences between each magnet pair are essential to obtain a uniform field amplitude. Table 4.2 lists the measured flux densities at the gap centers for individual pairs of magnets. According to Equation 4.1, the flux densities should be 0.642 T without a yoke, while it should be as high as 0.886 T with a yoke from

two adjacent magnets. Considering that a nonideal iron selection was used for the yoke planes, the average measured flux density of 0.727 ± 0.004 T seems reasonable.

For the waveform picked up from the magnetic field by the pickup coil (Figure 4.14), the time in the peak region is longer than that of a sinusoidal wave. This is reasonable because the magnets cover a larger area than does the aluminum plate in the magnetic holder, as shown in Figure 4.3.

The effective flux density of the AC magnet can empirically be estimated by comparing the area covered by the 16 magnets to the whole area of the ring:

$$B_{eff} \approx \frac{16A_s}{A_r} \cdot B_{ave} \tag{4.3}$$

where B_{ave} is 0.727 T. The factor $16A_s / A_r$ is the ratio of the area covered by the 16 magnets to the whole area of the ring. For our design shown in Figure 4.3,

$$A_s = 1\,\text{inch}^2$$

and

$$A_r = \pi(r_2^2 - r_1^2) = \pi(3.855^2 - 2.855^2) = 21.08\,\text{inch}^2$$

so $16A_s / A_r = 0.759$, slightly large than the rms value ($\sqrt{2}/2$) for a sinusoidal wave. This is consistent with the waveform in Figure 4.14.

Therefore, according to Equation 4.3, the effective flux density of the AC magnet is 0.552 T.

Table 4.2. Measured magnetic flux densities for each magnet pair

No	*B*/T
1	0.731
2	-0.718
3	0.728
4	-0.724
5	0.726
6	-0.727
7	0.733
8	-0.725
9	0.725
10	-0.726
11	0.728
12	-0.726
13	0.732
14	-0.729
15	0.722
16	-0.725

The field frequency depends upon the rotation speed, and can be easily calculated by

$$f = \frac{16}{2} \cdot \frac{S}{60} \tag{4.4}$$

where 16 is the number of the magnets on each magnet holder, and S is the rotor speed in RPM. If it rotates at a speed of 7500 RPM, then a frequency as high as 1 kHz can be realized. At the maximum 3600 RPM the system was tested at, a maximum frequency of 480 Hz was obtained.

4.4.6 Minimum AC Frequency for OTLC

Based on our estimate of effective magnetic flux density, the minimum AC frequency or the rotation speed of the rotor can be estimated for a given desired flow velocity. As we know from Chapter 1, for a 10 μm square channel, a minimum velocity of 100 μm/sec is required for OTLC. From Equation 3.4, the current density required can be calculated as

$$j = \frac{4\eta v}{WDFB} = \frac{4 \times 0.89\text{mPa} \cdot \text{sec} \times 100\mu\text{m/sec}}{10\mu\text{m} \times 10\mu\text{m} \times 0.14 \times 0.552\text{T}} = 46\text{mA/mm}^2 \tag{4.5}$$

According to the bubble current density threshold of the EMC in Figure 3.19, this current should be realized at a frequency of at least 200 Hz, which corresponds to a rotor speed of at least 1500 RPM. At the upper limit of rotation speed tested of 3600 RPM, a

frequency of 480 Hz corresponds to a bubble current density threshold of 78 mA/mm^2 in Figure 3.19, and a flow velocity of 160 μm/sec.

4.4.7 Eddy Current and Induced Electromotive Force

The above prediction is probably too optimistic, because of the heating effect of the currents induced in the electrodes by the magnetic field, known as the eddy current. Quantitative measurements on eddy heat were not done in this work. However, a temperature increase on an unbonded chip after several minutes running at ~2000 RPM was observed by hand touch. In fact, Eijkel *et al.* discussed eddy currents in MHD under AC magnetic field. At 2.44 kHz, their device temperature increased to 15 K above environmental with natural cooling (B = 0.1 T amplitude) and to 7 K above environmental with forced air-cooling (6). For a given electrode design, eddy heat is roughly proportional to the square of the frequency and the square of the magnetic field strength. At a frequency of about 200 Hz we are about one order magnitude lower than that used by Eijkel *et al.*, but the field strength is about one order magnitude higher. Considering our chip design uses much smaller electrodes, we expect that either comparable or less eddy heat will be generated in our chip. Nevertheless, the heat generated could be expected to create thermal gradients that affect the separation, and might even boil the liquid.

Another problem is related to the induced electromotive force (emf). Under an AC magnetic field, emfs will be induced from the wires. They will interfere with the electrical voltage applied to the electrodes. This can be solved by two methods with additional efforts. One is to compensate the input voltage with the emfs. The other is to create a design with the shortest electrode contact leads possible. Then the external wires connecting electrode pairs should be twisted when they are in the AC magnetic field. The emfs generated in the parallel electrodes will not affect the pumping because they have the same voltage and phase, and hence are cancelled.

4.4.8 Suspension of AC MHD Project

The goal of μTAS or lab-on-a-chip is to shrink the size into a chip, without bringing in many additional accessories. Obviously, a big AC magnet is a poor option, because of its cost and difficulty of use. The reason we originally decided to design this AC magnet is to find the best operating conditions for AC MHD, because AC MHD was believed to be the only chance of using MHD flow on chip. The operating conditions we were planning to explore include the applicability of EMC design, control and introduction of electric field, magnetic field strength and frequency, prism coupled LIF detection system, composition of electrolyte solution, and possible samples for separation. Most of these goals have not yet been achieved, because the research on AC

MHD was temporarily suspended. We have found a better way to realize MHD pumping on chip, which will be discussed in Chapter 5. However, we believe that this AC magnet may still give us useful information in the future.

4.5 Conclusions for AC MHD

A powerful AC magnet has been designed and manufactured which is able to generate a flux density of 0.552 T at a frequency up to 1 kHz. Such a field would allow EMC to pump as high as 100 μm/sec in a 10 μm channel. The research on AC MHD was temporarily suspended when a better idea for running an MHD pump was developed, as described in Chapter 5.

4.6 References

1. Lemoff, A. V., Lee, A. P., Miles, R. R., McConaghy, C. F., Transducers '99 **1999**, 1126-1129.
2. Lemoff, A. V.; Lee, A. P. *Sens. Actuators B* **2000**, 63, 178–185.
3. McPherson, G.; Laramore, R. D. An Introduction to Electrical Machines and Transformers, 2nd ed.; John Wiley & Sons: New York, **1981**.
4. GMW Associate, private communication.

5. Eijkel, J. C.T., Dalton, C., Hayden, C. J., Drysdale, J. A., Kwok, Y. C., Manz, A., In *Proceedings of Micro Total Analysis Systems 2001*; Kluwer Academic Publishers: Dordrecht, The Netherlands, 2001; pp 541-542.

6. Eijkel, J. C. T.; Dalton, C.; Hayden, C. J.; Burt, J. P. H.; Manz, A. *Sens. Actuators B*, **2003**, 92, 215-221.

7. GMW Associate, *Model 5403AC Users Manual*, GMW, San Carlos, CA, USA.

8. Magnet Sales & Manufacturing Inc., High performance permanent magnets, **1995**

9. Ocvirk, G.; Tang, T.; Harrison, D. J. *Analyst* **1998**, 123, 1429-1434.

10. Jiang, G.; Attiya, S.; Ocvirk, G.; Lee, W. E.; Harrison, D. J. *Biosens. Bioelectron.* **2000**, 14, 861-869.

Chapter 5

Magnetohydrodynamic Nano Pump for Liquid Chromatography on Chip

5.1 Introduction

MHD pumping can be performed in either DC or AC mode, because both can generate a Lorentz force. The reason for using the AC mode in MHD pumping is to suppress gas bubbles generated by electrolysis. However, AC MHD requires an alternating magnetic field, which is difficult to produce and operate at high field strengths and high frequencies. The AC magnetic field also causes eddy currents, which heat up the liquid in the channel and even result in bubbles. This makes us recall the advantages of DC MHD – inexpensive DC magnets at high field strength (such as Nd-Fe-B permanent magnets) and freedom from eddy currents as well. This thesis chapter discusses how to perform MHD in the DC mode without the generation of bubbles.

In an electrolyte solution, a DC current must be transferred from the electrode to a charge carrier in solution. This carrier must be a redox couple, coming from electrolyte solute, electrode, or the solvent. Electrolysis of water requires at least 1.2 V, and typically 2-3 V is used to get high currents. This has been the mode of choice in AC MHD to date.

Other redox couples besides H_2O might be used, but the > 0.1 M concentrations they would require to carry high current densities would be problematic for LC.

Gold nanoparticle suspensions or colloids can be prepared and suspended in water (1) and have been widely used as a marker for biological macromolecules (2, 3). Murray and co-workers have shown that alkanethiolate monolayer protected Au clusters (Au MPC) can transfer charge to and from an electrode (4-8). Thus, it is possible that they could be used as a substitute for redox couples. However, the currents Murray and co-workers obtained for suspended particles at electrodes were relatively low (*e.g.* 0.05 μA for hexanethiolate Au MPCs at a 9.5×10^{-3} cm^2 Pt electrode or 0.5 $\mu A/mm^2$ at 0.22 V, ref. 5). Murray and co-workers (9, 10) also worked with solid-state films, which have the highest concentration of Au MPC. The films showed the electron self-exchange rate was low, due to the insulating effect of the alkanethiolate chains (resistivity $\rho = 77\ \Omega cm$ for bulk toluenethiolate Au MPC, ref. 9). In solution, it is impossible to get such a high concentration of Au MPC (even if possible, it will be too viscous). Consequently, the current density that the MPC may carry seems to be far too low for MHD pumping.

From an alternative perspective, the assembly of nanoparticles to form filaments is known to occur in electrorheological (ER) fluids (11-14). Typically, non-conductive particles are used in ER. While it was not clear that Au nanoparticles could be used to

create dynamic nanowires in solution and thus pass a DC current in solution, we realized that if they did, such a solution could be used in DC MHD.

To be a current carrier for MHD, its particles must meet three conditions: a) be able to transfer and carry charges at least as well as redox couples do; b) be small enough to be well dispersed in the liquid; c) form a stable suspension. In this chapter, I will present a highly conductive liquid which is composed of gold nanoparticle suspensions and describe its applications to DC MHD. Large Au particles that did not require a monolayer coating for stabilization were used, at a relatively high concentration.

5.2 Experimental

5.2.1 Materials and Reagents

Gold nanoparticle suspensions (20 nm) were supplied by Sigma (St. Louis, MO, USA) with a concentration of 0.01 wt. %, containing 0.02% sodium azide preservative. They were concentrated to above 1 wt. % by a 10-kDa Microsep filter (Filtron Technology Corporation, Northborough, MA, USA) using a centrifuge (J2-21, Beckman Coulter, Inc., Fullerton, CA, USA) at 7000 RPM at 8 ± 4 °C. The concentration of gold nanoparticle suspensions was estimated from the volume ratio of the original (0.01 wt. %) and final solutions. Fluorescent beads (FluoSpheres, 2 μm, suspension of 2% solids, yellow green, Molecular Probes Inc., Eugene, OR, USA) were mixed with the

concentrated gold nanoparticle suspensions (1-5 vol. %), immediately vortexed, and then stored at 4-8 °C before use. A concentrated (> 0.1 mM) fluorescein solution was prepared by dissolving fluorescein disodium salt (Sigma, St. Louis, MO, USA) into DI water produced by a Milli-Q UV Plus Ultra-Pure system (Millipore, Mississauga, ON, Canada).

5.2.2 Operating Procedure

A permanent magnet (1" × 1", Nd-Fe-B, N5064, B_r = 1.44 T, Magnetic Component Engineering, Inc., Torrance, CA, USA) was mounted on a magnet holder. An EMC device (Device E or M, see Chapter 3) was placed onto the magnet. The mixture of nanoparticle suspensions and fluorescent beads was filled into one of the reservoirs. The channels were filled by capillary forces, and then the nanoparticle mixture was delivered into the other reservoirs. Sometimes a positive pressure was applied to help filling. The voltages applied to the channels were supplied by a homemade power supply (Figure 4.11, current: 2 A, voltage: 5 V). A homemade confocal microscope (15) coupled with a 488 nm argon ion laser (Cyonics, San Jose, CA, USA) was used for detection. The design was the same as that shown in Figures 4.5, 4.7 and 4.8, except the unit was mounted vertically, underneath the chip. The movement of the fluorescent beads indicated the flow in the channels, and was recorded by CCD camera (TK-1280U, JVC, Japan or ASTROVID StellaCam, Adirondack Video Astronomy, Glens Falls, NY, USA) and a

super VHS video recorder. The velocity was estimated from these movies as it was by Lemoff and Lee (16). The movie was played frame by frame so as to scale the time (30 frame/sec). The distance the fluorescent beads travelled was scaled in the monitor and then converted into real distance based on the magnification. The conductivity tests were done in the microchannels in Devices E and M. Voltages generated by the power supply were applied to the electrodes; currents were measured with a multimeter (3478A, Hewlett-Packard, Palo Alto, CA, USA). For nanoparticle images, one drop of gold suspension was pipetted onto nickel grids (300 mesh, Marivac Inc., Halifax, NS, coated using 0.3% pioloform (Ted Pella Inc., Redding, CA, USA) in chloform), air dried, and then observed with a transmission electron microscope (H-7000, Hitachi Co., Tokyo, Japan).

5.3 Results and Discussion

5.3.1 Concentrated Gold Nanoparticle Suspensions

Commercial gold nanoparticle suspensions are minimally conductive at the concentration they were provided (commonly 0.01 wt. %), as evidenced by a very simple, somewhat crude experimental study. Into a 200 μL sample of Au nanoparticle suspension, two Pt electrodes were inserted about 0.5 cm apart. A DC ohmmeter (which delivers 0.7 V) was connected to the electrodes and a resistance of about 70 kΩ was

measured. The same experiment was performed on the suspension solvent, after first removing the nanoparticles using a Microsep filter and a centrifuge. About the same resistance was measured. A 1 wt. % nanoparticle suspension was then measured in the same fashion, except the volume was about 10-20 μL, so the electrodes were closer together. The resistance observed was well below 1 kΩ. This study served to show that the concentrated nanoparticle suspension was considerably more conductive, indicating that more carefully designed experiments were worth pursuing.

Figure 5.1 shows an Ohmic relationship between the applied voltage and the resulting current density across a channel (10 μm deep × 10 μm wide × 4 mm long) for a 2 wt. % solution. No magnetic field was applied. Currents were passed for a few seconds at each voltage. This results indicate a very low resistance ($R = 16 \pm 0.4\,\Omega$) or resistivity ($\rho = 6.4 \pm 0.3\,\Omega\text{cm}$). The current density obtained is much higher than the bubble current density threshold seen in Figure 3.19, even though the voltage used was less than 0.5 V, much lower than the 1.2 V required for electrolysis to occur.

The Au nanoparticle concentration tested was from 1 to 2%. This concentration is lower than that of commonly used AC MHD electrolyte solutions, such as 1 M NaCl (6 wt. %) and 1 M KNO_3 (9 wt. %).

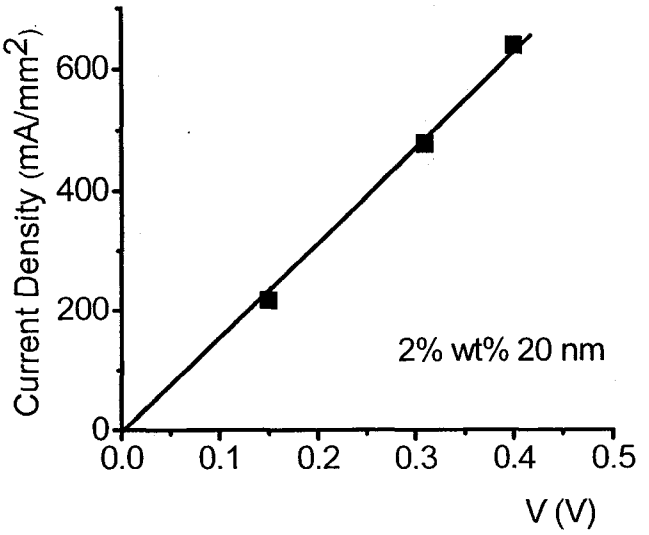

Figure 5.1. Ohm's relation for 2 wt. % gold nanoparticle suspensions.

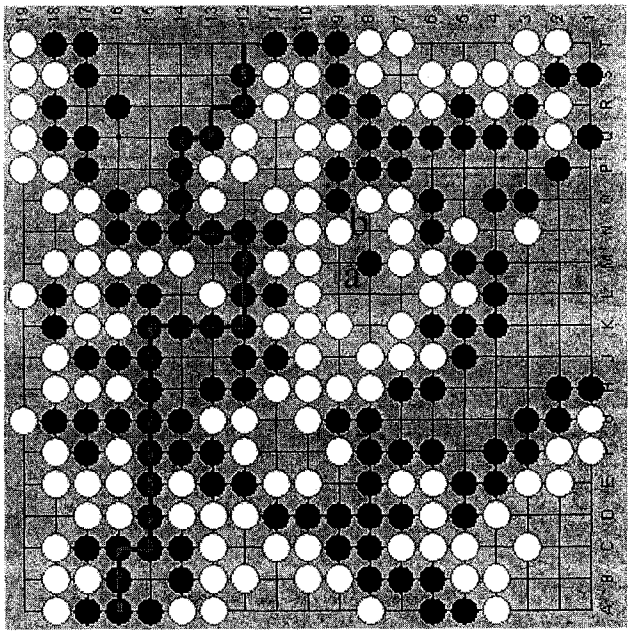

Figure 5.2. *Weichi* model. Black dots represent nanoparticles. The line indicates a wire is formed for electrical conduction.

5.3.2 Possible Mechanisms for Conduction

The reason why concentrated nanoparticle suspensions are conductive is not clear yet. Here we present three possible models. Figure 5.2 shows a Chinese game, *Weichi*. Suppose the black dots represent nanoparticles. If they, like the particles *a* and *b* in Figure 5.2, cannot see each other, then the liquid is not conductive. But after reaching a threshold concentration, a wire of particles could be formed, as shown in Figure 5.2. These nanowires could make the liquid highly conductive.

The Weichi model corresponds to an electron hopping model for charge transfer in solution between particles. The Dahms-Ruff equation (17, 18) can be used to describe charge exchange between a redox couple pair. Murray and co-workers presented how to calculate the *electron self-exchange diffusion coefficient* for Au MPC (8) using the Dahms-Ruff equation:

$$D_E = k_{EX}\delta^2 C/6 \qquad (5.1)$$

where k_{EX} is the biomolecular electron self-exchange rate constant ($M^{-1}s^{-1}$) for electron exchange, occurring at (center-to-center) distance δ(cm) in a solution of concentration C (M). For 1 wt. % 20 nm gold nanoparticle suspensions, $C = 2.1\times10^{-7}$ M (assuming uniform 20 nm diameter particles). We assume that the electron exchange between gold nanoparticles is diffusion controlled, $k_{EX} = 6\times10^{9}$ $M^{-1}s^{-1}$. According to Equation 5.1, a value as small as $8.4\times10^{-10}cm^2s^{-1}$ was obtained for the apparent diffusion coefficient by

electron hopping, which is much lower than the physical diffusion rate. This may indicate that the Weichi model is too crude to explain the conduction phenomena.

Another model is related to electrorheological (ER) fluids. Particles can be lined up under an electric field as shown in Figure 5.3, which is known as the Winslow effect (11). A crude model (12) of the origin of the Winslow effect assumes the following: the dielectric constant of the suspended particles is larger than that of the solvent; the electric field polarizes the particles, leading to the appearance of induced charge on the particle surface; the force between polarizable particles attracts particles to form a chain. Based on this model, the Winslow effect should not happen to conductive particles because the attractive force would be eliminated when the charges flow through them. Gold is a good electrical conductor, so the above ER model does not support gold nanoparticle suspensions exhibiting a Winslow effect. However, for each *naked* gold nanoparticle, a hydration layer surrounds it. The hydration layer increases electrical contact resistance between nanoparticles, and hence leaves the nanoparticles (or at least some of them) partially polarized. If this is the case, a weak attractive force might still exist among the partially polarized nanoparticles, and form loose nanoparticle chains. However, the good performance of Au as an electrode may mean this explanation is not valid. Note that a strong Winslow effect may not be good for MHD pumping because the *coarsening* of chains results in a high viscosity (12) and slows down the MHD pumping. In summary,

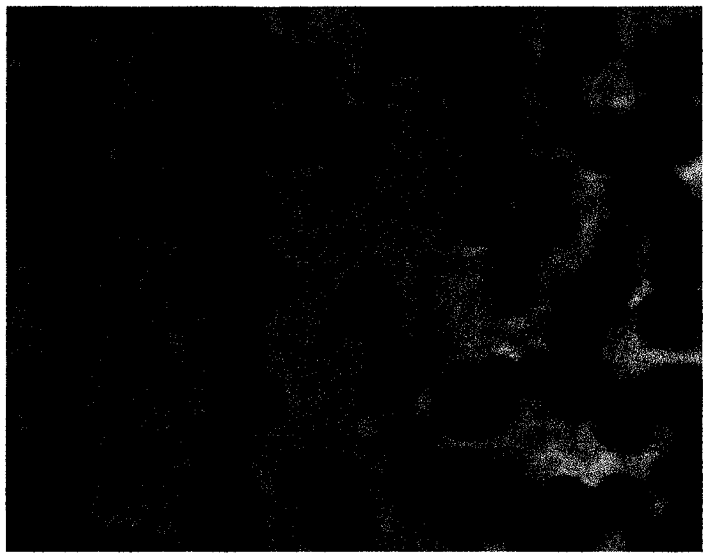

Figure 5.3. Electrorheological fluid image. The ER fluids are made of negative ion exchange resin (average size: 473 μm) and silicone oil. In the image an electrical field is applied from the top to the bottom (14).

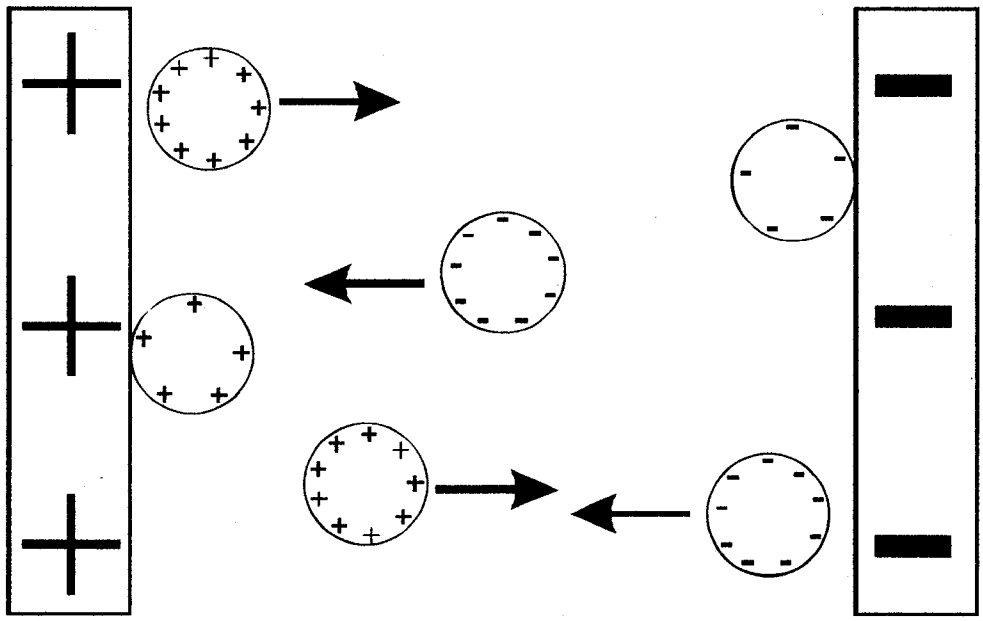

Figure 5.4. Nanocarrier model. The circles represent charged Au nanoparticles migrating in an applied electric field between the electrodes, and undergoing charging and discharging at the electrodes.

based on this model, a Winslow-like effect might happen in gold nanoparticle suspensions. Particles would tend to form chains (or statistical chains) and hence result in a high conductivity.

The third model we refer to as a *nanocarrier* model, as depicted in Figure 5.4. Suppose nanoparticles are carrying negative charges (this is the case after the nanoparticle suspensions are prepared, ref. 1-3), in an electric field between the electrodes, the nanoparticles move from the negative electrode to the positive electrode. Once arriving at the positive electrode, they release the carried charges and become positively charged at the anodic electrode. Once enough positive charges are obtained, the columbic force repels them away from the electrode. Because they are carrying positive charges, these nanoparticles migrate to the negative electrode. When reaching the negative electrode, they release the positive charge and become negatively charged. Such a process will cycle until a positively charged particle collides with a negatively charged particle, but requires the particles carry both charge states. Murray's studies on Au MPCs clearly show that these particles can store discrete charges, and be both oxidized and reduced (4-8). Collision between the nanoparticles would have two different results. One is that they are partially or fully neutralized, and hence slow down or even stop, until they collide with other nanoparticles. The other possibility is that they aggregate and hence the charge-carrying *ability* reduces. In summary, based on this

model, gold nanoparticles are nanocarriers, migrating between the electrodes. When 0.5 V is applied to a 10 μm wide channel, the electric field across the nanoparticle suspensions is 500 V/cm, which is a typical field strength used for EOF flow. Although the nanocarriers are bigger than any electrolyte ions, the electrophoretic flow velocity would not be much smaller because they are carrying much more charge.

5.3.3 Magnetohydrodynamic Nano Pump

If we fill an EMC with concentrated gold nanoparticle suspensions rather than an electrolyte solution, we should then be able to run MHD in the DC mode. Several tests were done and recorded as movies for analysis. Qualitatively similar results were obtained in all the trials. One test was performed in a 20 μm wide × 10 μm deep channel in device M. Gold nanoparticle suspensions (1 wt. %) mixed with 5 vol. % 2 μm fluorescent beads were introduced. Obviously, the former was the current carrier for pumping, while the latter was used for monitoring the flow. As can be seen in Figure 5.5, the fluorescent beads are very bright, even when the laser was focused off to the side of the channel (the faint spot in Figure 5.5). Under a magnetic field ($B \approx 0.4\,\mathrm{T}$) perpendicular to the chip and the plane of the page, when a voltage (from 0 to 0.2 V) was applied from the top electrode to the bottom electrode, a flow was observed from the left to the right. When the voltage was manually reversed (*i.e.* the top electrode negative, the

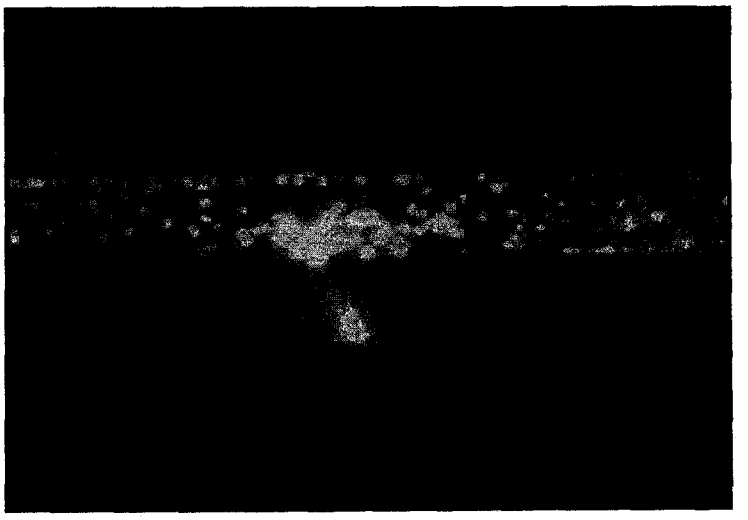

Figure 5.5. MHD Pumping in a straight channel (20 μm wide × 10 μm deep).

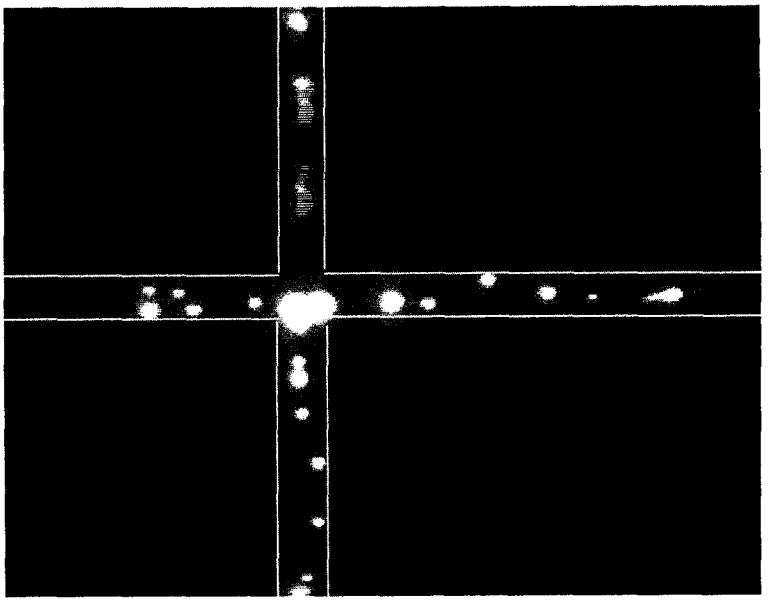

Figure 5.6. MHD pumping in a cross channel (10 μm wide × 9 μm deep).

bottom electrode positive), the flow direction was reversed (*i.e.* from the right to the left). Increasing the voltage to about 0.35 V clearly increased the pumping velocity to a maximum of 0.06 mm/sec, as evidenced by particle motion captured by the movie. In total, current was passed for about 1 min. The experiment was repeated several times. A subsequent run in the same device on a different day at 0.35 V gave a pumping velocity as high as 0.07 mm/sec.

Another movie was taken in a cross channel intersection of device E, with all the channels having a cross-section of 10 μm wide × 9 μm deep. Gold nanoparticle suspensions (2 wt. %) were mixed with 1 vol. % fluorescent beads to give the liquid in the microchannels. The laser was defocused by a lens (f = 15 cm) while the channels were still in focus. Therefore, the images, as shown in Figure 5.6, were not interferred by the laser. Three segments were recorded. First, a hydraulic flow inducing fluorescent particle velocity 0.1-0.15 mm/sec was coming down from the channel segment above the cross intersection. Second, MHD pump flow was generated by a voltage of about 0.5 V (current density: ~800 mA/mm^2) in the segment above the cross section to counter balance the hydraulic flow, although the counterbalance was not very stable. Finally, the MHD counter flow was released, the hydraulic flow continued. This experiment was performed for about 2 min. The above test was done under a magnetic field with a flux density of ~ 0.5 T.

In summary, voltage and current in Device E and M obey Ohm's law. The voltage we typically used was about 0.5 V or less. Consequently, there is no water electrolysis or bubbles formed in the channels. The current for pumping would be as high as 200 mA, depending on the channel length. For both 20 μm and 10 μm wide channels, the maximum pumping speed observed was higher than 0.07 mm/sec, sometimes greater than 0.1 mm/sec.

It is possible that the Ag electrodes are oxidized by the applied potential and contribute to the observed current. However, the studies presented demonstrate that the nanoparticles are playing a significant role in the observed current and MHD pumping. First, the crude conductivity study showed that the 1 wt % nanoparticle solution gave DC conductivity when using Pt electrodes. Second, the 0.01 wt % nanoparticle solution gave a high resistivity in that same experiment, and did not produce any MHD pumping in the microchip device. This indicates that Ag oxidation and dissolution alone, should it be occurring with 0.5 V applied, could not produce the MHD effect. Third, while it is conceivable that the Au particles carried negative charges in one direction, and the Ag ions carried positive charge in the other, this would give a non-steady state current that would not have allowed pumping for periods of a minute or longer. Clearly, experiments will need to be done using Au or Pt electrodes in the chip.

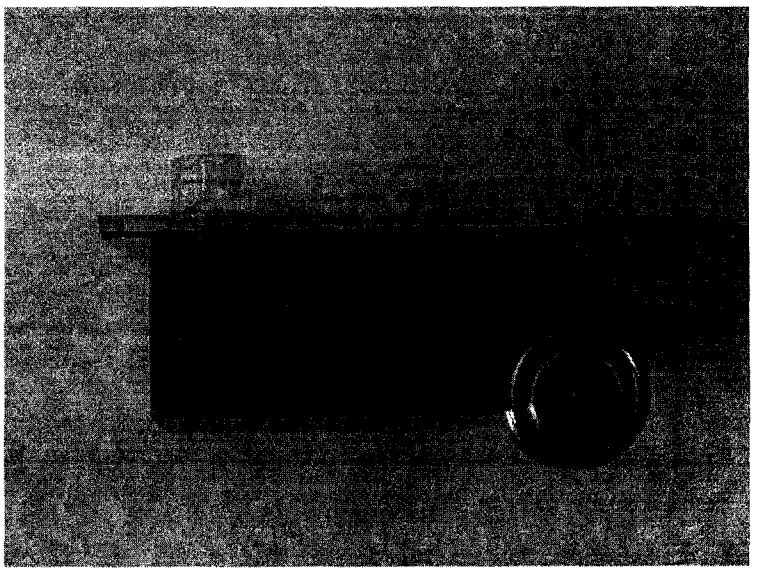

Figure 5.7. MHD nano pump, composed of a microchip (34 mm × 34 mm × 5 mm), permanent magnet (25.4 mm × 25.4 mm × 12.7 mm), and battery.

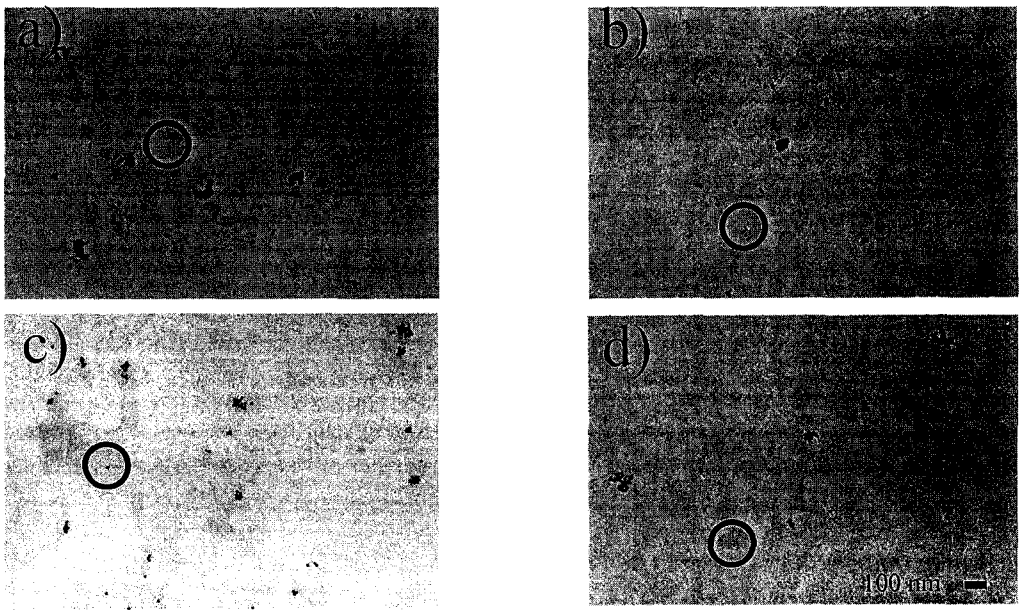

Figure 5.8. TEM images: a) 0.01 wt. % gold nanoparticle suspensions from the supplier; b) 2 wt. % suspensions, kept at 4-8 °C over night, and then diluted; c) 2 wt. % suspensions mixed with fluorescein to a final concentration of 0.1 mM, kept at 4-8 °C over night, and then diluted; d) 2 wt. % suspensions kept at room temperature overnight, and then diluted. A few discrete particles are circled for clarity.

Based on the above results, we can confidently state that we have accomplished an MHD pumping by a very simple technique: a microchip plus a permanent magnet as shown in Figure 5.7. Current required can be supplied by a small battery. We refer to this DC MHD as an *MHD nano pump*.

5.3.4 Stability of Concentrated Gold Nanoparticle Suspensions

For the MHD nano pump, we realize more tests need to be done. Among them, a nanoparticle stability test was the highest priority. Clearly, if nanoparticles aggregate after concentrating, then they will no longer be able to carry current and move, so the stability of concentrated gold nanoparticle suspensions is essential to the application of the MHD nano pump. Several preliminary tests in this thesis work covered both temperature stability and chemical stability. Concentrated nanoparticle suspensions should be stable at room temperature for at least as long as a separation time. They should also be stable to analytes or buffer solutions used in LC. In this thesis work, four samples were examined by TEM:

a) 0.01 wt. % nanoparticle suspensions from the supplier;

b) 0.01 wt. % nanoparticle suspensions concentrated to 2 wt.%, kept at 4-8 °C over night, and then diluted back to 0.01 wt. %;

c) 2 wt. % concentrated nanoparticle suspensions mixed with fluorescein to a final concentration of 0.1 mM, kept at 4-8 °C over night, and then diluted back to 0.01 wt. %;

d) 2 wt. % concentrated nanoparticle suspensions kept at room temperature overnight, and then diluted back to 0.01 wt. %.

No difference in these solutions was observed by the naked eye. Figure 5.8 shows TEM images, indicating that sample *b* had approximately as many single nanoparticles as sample *a*. Sample *c*, in which concentrated nanoparticle suspensions were mixed with a high concentration of fluorescein, appears similar to the original *a* suspensions also. TEM image of sample *d* indicate that the nanoparticle suspensions tended to aggregate if they were kept at room temperature for a long time. Therefore, concentrated nanoparticle suspension should be kept in the refrigerator when not in use.

The TEM image of the gold nanoparticle suspensions after pumping was of great interest. However, we were not able to collect the sample yet.

5.4 Conclusions

Concentrated gold nanoparticle suspensions have been found to be a good current carrier for MHD flow. As a start point, experimental results indicate very optimistic applications in microfluidics, especially LC chips. More detailed tests and mechanism studies are required. However, with the EMC design, a powerful MHD nano pump has

been realized. It is easy to use. We believe that the door to an MHD LC on chip has been opened.

5.5 References

1. Frens, G. *Nature Phys. Sci.* **1973**, 241, 20.
2. Hayat, M. A. (Ed.) *Colloidal Gold: Principles, Methods, and Applications*, Vol. 1, Academic Press, San Diego, **1989**.
3. Hayat, M. A. (Ed.) *Colloidal Gold: Principles, Methods, and Applications*, Vol. 2, Academic Press, San Diego, **1989**.
4. Ingram, R. S.; Hostetler, M. J.; Murray, R. W.; Schaaff, T. G.; Khoury, J. T.; Whetten, R. L.; Bigioni, T. P.; Guthrie, D. K.; First, P. N. *J. Am. Chem. Soc.* **1997**, 119, 9279-9280.
5. Chen, S.; Ingram, R. S.; Hostetler, M. J.; Pietron, J. J.; Murray, R. W.; Schaaff, T. G.; Khoury, J. T.; Alvarez, M. M.; Whetten, R. L. *Science* **1998**, 280, 2098-2101.
6. Chen, S.; Murray, R. W.; Feldberg, S. W. *J. Phys. Chem. B* **1998**, 102, 9898-9907.
7. Chen, S.; Murray, R. W. *Langmuir* **1999**, 15, 682-689.
8. Hicks, J. F.; Templeton, A. C.; Chen, S.; Sheran, K. M.; Jasti, R.; Murray, R. W.; Debord, J.; Schaaff, T. G.; Whetten; R. L. *Anal. Chem.* **1999**, 71, 3703-3711.
9. Wuelfing, W. P.; Murray, R. W. *J. Phys. Chem. B* **2002**, 106, 3139-3145.

10. Wuelfing, W. P.; Green, S. J.; Pietron, J. J.; Cliffel, D. E.; Murray, R. W. *J. Am. Chem. Soc.* **2000**, 122, 11465-11472.

11. Winslow, W. *J. Appl. Phys.* **1949**, 20, 1137.

12. Halsey, T. C. *Science* **1992**, 258, 761-766

13. Trau, M.; Sankaran, S.; Saville, D. A.; Aksay, I. A. *Nature* **1995**, 374, 437-439.

14. Rhee, E.-J.; Park, M.-K.; Yamane, R.; Oshima, S. *Exp. Fluids* **2003**, 34, 316–323.

15. Ocvirk, G.; Tang, T.; Harrison, D. J. *Analyst* **1998**, 123, 1429-1434.

16. Lemoff, A. V.; Lee, A. P. *Sens. & Actuators B* **2000**, 63, 178-185.

17. Dahms, I. *J. Phys. Chem.* **1968**, 72, 362-364.

18. Ruff, I.; Friedrich, V. J. *J. Pyhs. Chem.* **1971**, 75, 3297-3302.

Chapter 6

Conclusions and Future Work

6.1 Conclusions from the Thesis Work

Controlled pressure driven flow within microfluidic devices is not simple to achieve. The flow behavior, generation and control of pressure driven flow for the purpose of performing chromatography was the subject of this thesis. In Chapter 2, the Hagen-Poisseuille equation is shown to hold experimentally in 1 μm deep microchannels, giving us confidence in designing microfluidic devices down to the 1 μm scale using that equation. In order to realize on-chip pressure generation and valveless control of fluid flow, magnetohydrodynamic (MHD) flow was studied. The conditions under which MHD could be used successfully for open tubular liquid chromatography were first examined. Then MHD designs were developed. Among three ideas presented in this thesis work, the experimental combination of an electromagnetic channel (EMC) with a concentrated gold nanoparticle suspension produced a functioning DC MHD nano pump, showing a flow velocity of 0.1 mm/sec in a 10 μm size channel. These results open up the possibility of realizing LC chips. As a major important side product, concentrated gold nanoparticle suspensions were discovered to be a highly conductive liquid, giving an alternative to electrolyte solutions. The applications of such a liquid may be very wide.

6.2 Future Work

While opening some new fields, this thesis work also leaves many interesting areas to be studied. Below is a brief discussion of those topics.

6.2.1 Nanoparticle Suspensions

6.2.1.1 Concentration of Nanoparticle Suspensions

1-2 wt. % was the concentration studied in this thesis work. In order to understand the mechanism of nanoparticle conduction and design the next generation of DC MHD nano pump, determining the relation between conductivity and concentration is the first priority. Such a test may find a transition point where nanoparticle suspensions change from nonconductive (or weakly conductive) to highly conductive. Any MHD nano pump obviously will be operated above this transition point. Whether the transition point exists or not is a piece of key information regarding the mechanism of nanoparticle conduction. Furthermore, the upper limit of concentration and the effect on conductivity is also an important design factor.

6.2.1.2 Nanoparticle Size

Nanoparticle size is another key factor for DC MHD pumping. We do not know how and how much the size will affect the conductivity of the suspensions. The trend of conductivity on the nanoparticle size will help determine the size that is the best for electrical conductivity and for MHD pumping. Smaller particles mean more particles per unit weight added and hence higher concentration, which should be good for electrical conduction. But smaller particles might carry less current or drag less solvent with them. So the size needs to be optimized. For DC MHD nano pump, a smaller nanoparticle size may also mean better solution-like flow behavior, with a lower viscosity.

6.2.1.3 Nanoparticle Materials

Compared to gold, silver shows higher electrical conductivity. However, it is not clear whether silver nanoparticle suspensions will show a much higher DC electrical conductivity. If it is not significantly higher than gold, then gold may be a better choice, because of its relatively inert chemical properties. The search for materials will certainly not be limited to silver, other metals such as platinum and copper could also be an option for different applications. Bucky balls, carbon nanotubes, and other carbon-based materials are believed to have much higher conductivity than metals. Since they are highly compatible with chemical systems, they could be one of the better candidates for

DC conductive solutions. Conductivity tests will direct us to which materials are the best for DC electrical conductivity and for MHD pumping.

6.2.1.4 Nanoparticle Shape

Nanoparticle shape may be another extremely important factor for DC conductivity and for MHD pumping. The idea of the DC MHD nano pump came from a dream of making conductive nanowires connecting the electrodes in the microchannels. Obviously, nanowires connected to the electrodes will show the lowest resistance, but they should simultaneously be movable along the electrodes, like the *electric brushes* used in motors. So far we do not know how to make them. However, an accessible way is to realize conduction by nanowire chains. Nanowires can be suspended in the solution, just like nanoparticles, and may then transfer current as do the nanoparticles. If they can be aligned along the electric field, then they will contribute an extremely high conductivity. This will be very close to our dream.

6.2.2 LC Chips

A major difficulty in making OTLC chips can be solved by the DC MHD nano pump. It can be expected that the first MHD LC will be made soon. A key step left is to coat the EMC channel. Ideal coating should be on the top and bottom walls of the EMC

as shown in Figure 3.12. The electrode could either be left naked, or be coated by a thin conductive film, so that the electric current will not be reduced. Silver is not a good electrode material, because it would be oxidized by a low voltage. Perhaps gold is the best choice. With those developments, a working MHD LC chip will be realized very soon.